The Chiral and Deconfinement Phase Transitions in Strongly Interacting Matter

Vom Fachbereich Physik
der Technischen Universität Darmstadt

zur Erlangung des Grades
eines Doktors der Naturwissenschaften
(Dr. rer. nat.)

genehmigte Dissertation von
Dipl.-Phys. Mathias Wagner
aus Frankfurt am Main

Darmstadt 2008
D17

Referent: Prof. Dr. Jochen Wambach
Korreferent: Prof. Dr. Christian S. Fischer
Tag der Einreichung: 2.12.2008
Tag der Prüfung: 2.2.2009

"The idiot physicists, unable to come up with any wonderful Greek words anymore, call this type of polarization by the unfortunate name of 'color', which has nothing to do with color in the normal sense."

– Richard. P. Feynman

Zusammenfassung

Das Phasendiagramm stark-wechselwirkender Materie ist eines der spannendsten Forschungsgebiete der modernen Teilchenphysik. Theoretisch wird die stark-wechselwirkende Materie durch die *Quantenchromodynamik* (QCD) beschrieben. Bei endlichen Temperaturen und Dichten werden zwei Phasenübergänge erwartet: die Restaurierung der chiralen Symmetrie und die Aufhebung des Farbeinschlusses (‚deconfinement'). Im Standardszenario erwartet man die Existenz eines kritischen Endpunktes im Phasendiagramm.

Neben Gittereichtheorien, die nur bei verschwindendem chemischen Potenzial anwendbar sind, stellen Rechnungen in effektiven Modellen die einzige Möglichkeit dar, in beliebige Bereiche des Phasendiagrammes vorzudringen. Die Konstruktion dieser Modelle orientiert sich an der chiralen Symmetrie der QCD. Eines dieser effektiven Modelle ist das lineare σ-Modell (LσM), ergänzt um fermionische Freiheitsgrade.

Wir haben in einem LσM mit drei leichten Quarks den Einfluss verschiedener Parameter und der $U(1)_A$ Anomalie auf die Restaurierung der chiralen Symmetrie und auf die Existenz und Position des kritischen Endpunktes untersucht. Die chirale kritische Oberfläche bestätigt das Standardszenario des QCD-Phasendiagramms.

Das untersuchte Modell beinhaltet keine gluonischen Freiheitsgrade und ist somit nicht in der Lage, Effekte im Zusammenhang mit dem Farbeinschluss der QCD zu beschreiben. Eine Möglichkeit, diese Effekte dennoch zu berücksichtigen, stellt die Ankopplung des ‚Polyakov Loops' an das LσM mit Quarks dar. Dies führt zum ‚Polyakov–Quark-Meson'(PQM) Modell.

In diesem Modell wurde der Zusammenhang der beiden Phasenübergänge betrachtet. Insbesondere wurde untersucht, ob beide Übergänge entlang einer gemeinsamen Phasengrenze auftreten. Bei verschwindendem chemischen Potenzial wird ein etwa gleichzeitiger Übergang bevorzugt. Bei höheren chemischen Potenzialen laufen die beiden Phasenübergänge allerdings auseinander, und der chirale Übergang erfolgt vor dem ‚deconfinement'-Übergang. Dies führt zu einer Phase mit quarkionischer Materie im PQM-Modell. Der chirale Phasenübergang erfolgt im Allgemeinen bei höheren Temperaturen als im Modell ohne Farbeinschluss. Im Weiteren wurden verschiedene thermodynamische Eigenschaften stark-wechselwirkender Materie untersucht. Im PQM-Modell konnten aktuelle Gitterdaten reproduziert werden. In der Nähe des kritischen Endpunktes wurde zudem die Größe der kritischen Region bestimmt. Ihre Form lässt sich durch unterschiedliche Werte der kritischen Exponenten für verschiedene Pfade zum kritischen Endpunkt erklären, die wir explizit berechnet haben.

Eine Extrapolationsmethode, um Ergebnisse aus Gitterrechnungen auch auf endliches chemisches Potenzial auszudehnen, basiert auf einer Taylorentwicklung des Druckes. Es wurde eine neue Technik entwickelt, um hohe Koeffizienten mit hoher Präzision zu berechnen. Dies erlaubt uns, zusammen mit der Möglichkeit, das thermodynamische Potenzial im PQM-Modell bei endlichem chemischem Potenzial auszuwerten, erstmals die Methode einem fundierten Test in einem realistischen Modell für stark-wechselwirkende Materie zu unterziehen. Es stellt sich heraus, dass selbst mit Koeffizienten 24. Ordnung keine verlässliche Abschätzung der Position des kritischen Endpunktes möglich ist.

Contents

1. Introduction

Strongly interacting matter under extreme conditions is one of the most fascinating subjects in modern particle physics. In the standard model of particle physics the strong interaction is one of the four fundamental forces besides gravity, electromagnetic and weak interaction. While gravity and electromagnetic interactions are experienced in daily life, the strong and weak interaction are not directly present. But the strong interaction, subject of this thesis, is crucial for our existence. It is, e.g., responsible for the existence of nuclei and nucleons. Actually, most of the mass we observe is created dynamically by the strong interaction [1].

Theoretically the strong interaction is described by Quantum Chromodynamics (QCD) [2]. The particles described in this theory the microscopical degrees of freedom, are quarks and gluons. In the standard model there exist six quark flavors (up, down, strange, charm, bottom, top). The 'C' in QCD refers to the 'color' charge carried by the quarks, i.e., the three colors red, green or blue. The gluons are the force carriers in QCD. The fact that they also carry color charge, and can therefore interact with themselves, has enormous consequences for the theory.

QCD has two peculiar features, *confinement* and *asymptotic freedom*. Quarks and gluons interact only weakly at small distances. This is just the opposite of every-day life, e.g., when considering the force between two magnets. In the language of particle physicists asymptotic freedom means, that the coupling constant becomes small at very small distances or correspondingly high energies. For the discovery of asymptotic freedom Politzer [3], Wilczek and Gross [4] were awarded the 2004 Nobel Prize in physics. At large distances the potential between quarks grows linearly with the distance, hence an infinite amount of energy is required to separate two static quarks. This results in confinement, meaning that quarks cannot be separated. Before the two quarks can be separated it becomes energetically favorable to create a new quark-antiquark pair. The non-existence of free quarks, i.e., particles with a fractional charge, has been tested up to high precision and no signature for the existence of free quarks has been found. This feature is closely related to color confinement, meaning that colored particles cannot be observed. Baryons built up of three quarks are colorless objects, since the red, green and blue quarks add up to white. In mesonic states, built out of one quark and one anti-quark, one constituent carries a color while the other carries the corresponding anti-color. The details of the confinement mechanism are not yet fully understood.

In this work we will consider strongly interacting matter at extreme conditions, i.e., at high temperatures and high densities. Similar to boiling water that undergoes a phase transition from liquid to gas, a phase transition is expected for strongly interacting

matter. At low temperatures and low density strongly interacting matter is found in the hadronic phase, i.e., quarks are confined in mesons and hadrons. At higher temperatures the confining interactions become weak and a *quark-gluon plasma* (QGP) is formed.

The question of the phases of strongly interacting matter is not purely academic. The QGP was certainly present in the early universe. After the Big Bang the universe was very hot and the net baryon density was low. Between $10^{-6}\,s$ and $1\,s$ after the Big Bang, the QGP cooled down and hadrons were formed. During this time the early universe passed the phase transition described above. Nowadays a QGP might be found in compact stellar objects, e.g., neutron stars. In these objects the density is very high and so-called color-superconducting phases might exist [5, 6]. These are not a topic of this work.

Experimentally, the phase structure of strongly interacting matter is probed in current (e.g., RHIC at BNL, LHC at CERN) and future experiments (CBM at FAIR). In these experiments heavy-ion collisions are used to create the energy densities required to form a QGP. The interpretation of the experiments is somewhat involved, as the QGP is only generated temporarily. In the detectors different particles emerging from several stages of the collisions are measured. Detailed knowledge of the thermodynamic properties of strongly interacting matter is required to interpret the results.

A further property of QCD is its chiral symmetry, stating that left and right-handed quarks do not mix. This symmetry is exactly realized in the limit of massless quarks and still an approximate symmetry for light quark masses. At high temperatures, chiral symmetry should be restored. The phase transition from the chirally broken to the chirally restored phase is a distinct phenomenon from the deconfinement transition, but both transitions might occur along one common phase boundary. We will investigate the phase boundaries for both transitions.

The work is organized as follows: In Chapter 2 the QCD phase diagram is discussed in general in order to provide a more detailed introduction to the subject. We will discuss several techniques to access the QCD phase diagram, both theoretically and experimentally. The conjectures concerning a critical end point and its dependence on quark masses are summarized.

In Chapter 3 the chiral symmetry restoration is discussed using an effective linear sigma model (LσM) with three quark flavors. The masses of the charm, bottom, and top quarks are much larger than the relevant scales for the phase transitions discussed here, hence the restriction to the three lightest flavors up, down and strange is justified. After an introduction of the model the chiral symmetry restoration is investigated in detail, in particular the existence and location of the critical end point. Most of the results have already been published in [7].

The LσM implements the chiral symmetry of QCD but lacks confinement. In Chapter 4 the model will be augmented by the Polyakov loop, which provides an effective implementation of confinement. The chiral and deconfinement transitions are explored at vanishing and finite density. The influence of the Polyakov loop on the critical end point will be discussed.

In Chapter 5 the thermodynamic properties of strongly interacting matter are investigated in the framework of the models described in the previous two chapters. The influence of the Polyakov loop on several properties is considered and the results are compared to recent lattice data. The influence of the Polyakov loop on the thermodynamic properties near the critical point, in particular the critical exponents, will be discussed.

Since lattice calculations cannot directly access finite density in the QCD phase diagram, several extrapolation methods have been proposed. In Chapter 6 we compare one specific technique, the so called Taylor expansion, with model calculations at finite μ. Applying a novel numerical technique we can perform this expansion up to high orders. This allows us to check the limits and predictive power of this approach.

The results of this work are summarized in Chapter 7.

In appendix A we collect several formulas and parameters concerning the LσM with quarks used in this work.

The numerical method used for the high precision calculation of derivatives in Chapters 5 and 6 is presented in appendix B.

2. Phase diagram of strongly interacting matter

In this chapter we will introduce different approaches to study the QCD phase diagram. The main problem is that neither theoretical nor experimental approaches are straightforward, hence the qualitative and even more the quantitative knowledge is very limited (for reviews see, e.g., [8, 9, 10, 11, 12]). Before discussing the approaches, we briefly introduce the current conjectures about the QCD phase diagram.

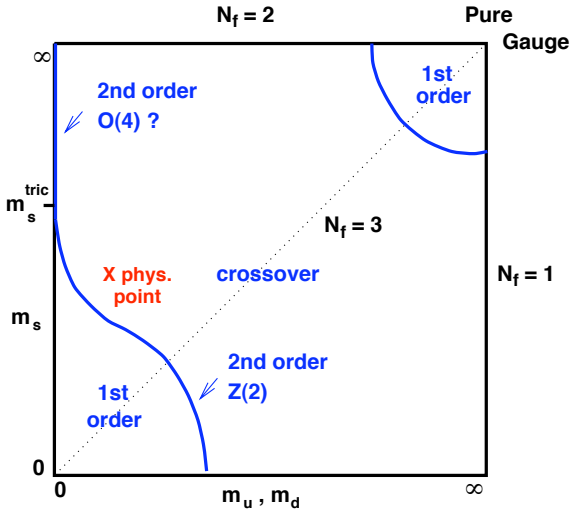

Figure 2.1.: Quark mass dependence of the QCD phase transition at vanishing chemical potential in the plane of the light (m_u, m_d) and strange (m_s) bare quark masses. Figure taken from [13].

2.1. Existence of a critical end point

In the standard scenario the QCD phase diagram obeys a critical end point (CEP). This picture relies heavily on model calculations. Many of these calculations predict a chiral first order transition at finite chemical potential and zero temperature [14, 15, 16]. At zero chemical potential a chiral crossover, predicted also by models, seems now to be confirmed by lattice calculations [17]. At some point on the phase boundary the first-order transition has to end and change into a crossover. At this critical end point the

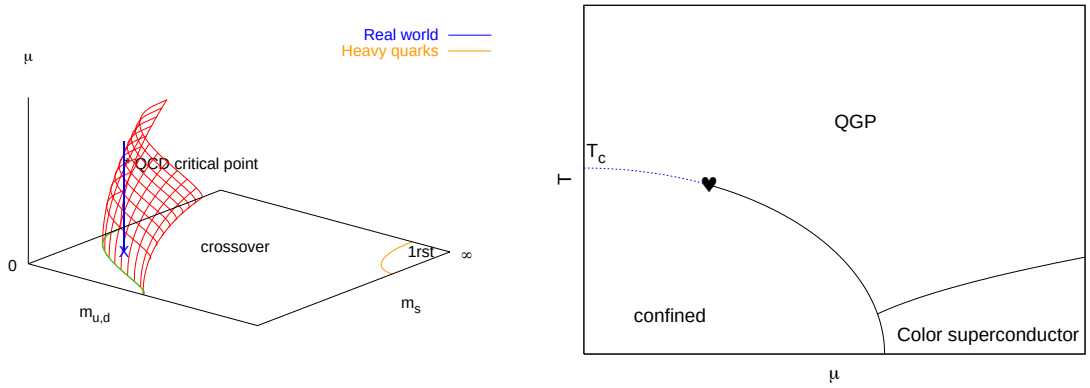

(a) Critical surface (b) Phase diagram

Figure 2.2.: Left: The chiral critical surface defined by the critical chemical potential as function of the light (m_u, m_d) and strange quark (m_s) masses in the standard scenario. Right: The corresponding phase diagram with a critical end point (♡). Figures taken from [13].

transition is of second order. Its existence and location are among the most discussed issues.

Further insight on the phase structure can be gained from considering the quark mass dependence at vanishing chemical potential. In Fig. 2.1 the order of the phase transition is shown as a function of the masses of the two light (m_u, m_d) and the strange quark (m_s). In the lower left corner all quark masses are zero and the chiral symmetry is not explicitly broken. In this chiral limit it is known from universality arguments that the phase transition is of first order [18]. At infinite quark masses no dynamical quarks $(N_f = 0)$ contribute to the system and the dynamics is purely governed by the gluons. This limit is called the pure-gauge limit or Yang-Mills sector of QCD. Between these two limits a region is expected where the transition is a crossover. For vanishing light quark masses $(m_u = m_d = 0)$, a critical strange quark mass (m_s^{tric}) is expected. For $m_s > m_s^{tric}$ and $m_u = m_d = 0$ the transition is second order, in particular also in the limit of $m_s \to \infty$ corresponding to $N_f = 2$. Note that the considerations of the limits $(m \to 0, \infty)$ rely on the presence of the $U(1)_A$ anomaly. While it has not been clear for a long time on whether the physical point, i.e., the point at realistic quark masses, is located in the crossover or the first-order region, recent lattice calculations seem to resolve this issue and confirm a crossover for realistic masses [17]. On the critical line separating the crossover and first-order region, the transition is of second order.

If the chemical potential is turned on, the critical line extends to a surface. It is not known how this surface behaves at finite chemical potential. To ensure the existence of a critical end point it is required that the surface bends towards the physical point. Starting at $\mu = 0$ at the physical point, the surface is then crossed at the critical chemical

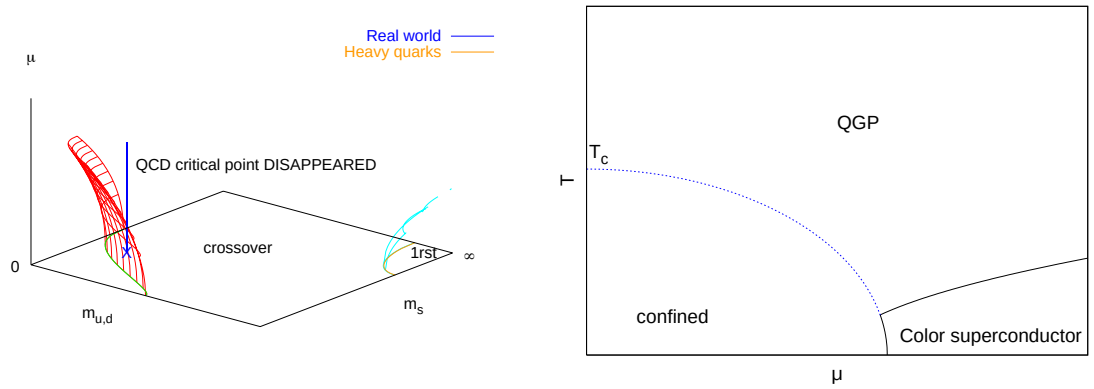

(a) Critical surface (b) Phase diagram

Figure 2.3.: Similar to Fig. 2.2 but for the non-standard scenario of QCD as suggested by de Forcrand and Philipsen [19]. Figures taken from [13].

potential μ_c and the transition changes from a crossover to a first-order transition. This standard scenario is shown in Fig. 2.2(a). The resulting phase diagram, including a critical end point is shown in Fig. 2.2(b).

An alternative scenario, brought up by de Forcrand and Philipsen [19], is shown in Fig. 2.3(a). In this case the surface bends towards lower masses and no critical chemical potential is found at the physical point. The transition always stays in the crossover region and no critical end point is found in the corresponding QCD phase diagram shown in Fig. 2.3(b). Hints for this scenario have been found in some lattice calculations [20, 21] and recently also in model studies [22].

One cannot a priori exclude the possibility that the critical surface has a more complex shape than the ones shown here. Assuming for now that a critical end point exists, it is still not known where it is located in the phase diagram of QCD. The results of model calculations scatter over the whole region of the QCD phase diagram [23]. As we will see later, the location of the critical end point vitally depends on the parameters used in these models.

2.2. Theoretical approaches

QCD is a non-Abelian quantum-field theory defined by the Lagrangian

$$\mathcal{L}_{\mathrm{QCD}} = \bar{\Psi}\left(i\gamma^{\mu}D_{\mu} - \hat{m}\right)\Psi - \frac{1}{4}F^{a}_{\mu\nu}F^{\mu\nu}_{a} + \mathcal{L}_{\mathrm{gauge}} \ , \tag{2.1}$$

where Ψ denotes the quark field. The gluonic field strength tensor

$$F_{\mu\nu} = \partial_{\mu}A_{\nu} - \partial_{\nu}A_{\mu} - ig[A_{\mu}, A_{\nu}] \tag{2.2}$$

with the coupling constant g and the vector potential A_{μ} describes the gluon dynamics. The covariant derivative D_{μ} is defined as

$$D_{\mu} = \partial_{\mu} - igA_{\mu} \ . \tag{2.3}$$

The matrix $\hat{m}$ denotes the quark masses for the three light flavors. In nature $N_f = 6$ quark flavors exist, but for the energy region of interest, i.e., $\mathcal{O}(10^2)$ MeV, only the three light flavor up, down and strange are relevant. The other flavors are suppressed due to their high masses. The term $\mathcal{L}_{\mathrm{gauge}}$ includes gauge fixing terms and the contribution of the Faddev-Popov ghosts. We will turn to calculations in an effective model later, hence a specification of this term is not required here. Details can be found, e.g., in [24].

The thermodynamics of QCD can be described by the grand canonical partition function

$$Z_{\mathrm{QCD}}\left(T, \mu_f; g, m_f\right) = \int DAD\bar{\Psi}D\Psi e^{-S_g[A_{\mu}]}e^{-S_f[\bar{\Psi},\Psi,A_{\mu}]} \tag{2.4}$$

with the Euclidean gauge and fermion actions

$$S_g[A_{\mu}] = \int_0^{\beta} dx_0 \int_V d^3x \ \frac{1}{2}\mathrm{Tr}\ F_{\mu\nu}F^{\mu\nu} \tag{2.5}$$

and

$$S_f[\bar{\Psi}, \Psi, A_{\mu}] = \int_0^{\beta} dx_0 \int_V d^3x \ \sum_{f=1}^{N_f} \bar{\Psi}_f\left(\gamma^{\mu}D_{\mu} + m_f - \mu_f\gamma_0\right)\Psi_f \ , \tag{2.6}$$

respectively. Here the chemical potential μ and the inverse temperature $\beta = 1/T$ have been introduced. Note that to exclude gauge-equivalent field configurations in the functional integral, one has to include the Faddev-Popov ghosts included in the unspecified term $\mathcal{L}_{\mathrm{gauge}}$. Since we do not want to solve (2.4) directly, we will ignore this for now.

Unfortunately it is not known how to evaluate this partition function exactly. In the region of interest the coupling constant of QCD is strong and perturbation theory is not applicable. In the next subsections we will shortly introduce lattice gauge calculations and studies in effective models.

2.2.1. Lattice Calculations

In this subsection we will briefly discuss lattice calculations and their limitations. The status of the most important results concerning the QCD phase diagram is presented. More detailed reviews of lattice calculations can be found in [13, 25].

Lattice calculations provide one way to solve the thermodynamics of QCD. The continuous theory is reformulated on a discrete lattice with a finite number of lattice points and finite lattice spacing. These lattices usually use a larger number of point for the spatial dimensions (N) than for the temporal direction (N_τ), resulting in lattice sizes of $N^3 \times N_\tau$. The number of points is limited by the available computing resources. The discretized QCD partition function can then be calculated at vanishing chemical potential using Monte Carlo methods.

In these calculations it is technically advantageous to replace the fermionic action with a formulation more suitable for the Monte Carlo calculations S_f^{MC}. Several lattice actions are available with different problems and advantages, e.g., staggered or Wilson fermions. These formulations trade certain properties of QCD like the chiral symmetry for the ability to do simulations on larger lattices or at smaller quark masses. Details can be found, e.g., in [26].

Lattice calculations become more expensive with decreasing quarks masses. Only recently it became possible to reach the region of physical light (up and down) quark masses. A lot of older but also recent calculations have been carried out at too large quark masses and the results have to be extrapolated to realistic masses.

In addition, lattice calculations suffer from inherent problems. The lattices have a finite lattice spacing a and a corresponding volume $V = (Na)^3$. For results close to the continuum and thermodynamic limits, $a \to 0$ and $V \to \infty$ is preferred, but these are contradicting requirements. One therefore has to carefully chose an adequate lattice spacing and check the results for artifacts of the finite volume and lattice spacing. Furthermore, all these calculations are performed in lattice units not uniquely related to physical units. This requires a procedure to translate the results to physical units. The problems described above are severe, but advances in computing and algorithms will allow for larger lattices and more realistic quark masses. Older calculations further suffered from temperature-dependent physical quark masses m_f. The quark mass is fixed in lattice units, i.e., $am_f = \text{const}$. For finite temperatures the lattice spacing is related to the temperature via $T = 1/(aN_\tau)$. Newer calculations are partly performed along the line of constant physics, where this temperature dependence is corrected by adjusting the quark masses in lattice units to keep the physical quark masses at fixed values. Thus, even though lattice calculations are a first-principles approach to QCD thermodynamics, their results come out of a black box. From this point of view, lattice results are closer to experimental measurements than to theoretical studies.

For several years it seemed that the value of the pseudocritical temperature was settled to a value of $T_\chi \approx 175\,\text{MeV}$ for two quark flavors, which is expected to be a good approximation to the realistic 2+1 flavor case [27]. Since 2006 this situation has changed

dramatically. Currently, there are two major lattice groups performing high precision simulations to study the QCD phase diagram with masses close to realistic values.

The RBC-Bielefeld group performed calculations using improved staggered fermions on $N_\tau = 4, 6$ lattices along the line of constant physics, but the ratio of the light and the strange quark mass was still above its physical value [28]. The latest pseudocritical temperature reported by the RBC-Bielefeld collaboration is

$$T_\chi^l = T_d = 192(7)(4)\,\mathrm{MeV} \tag{2.7}$$

for the chiral transition of the light quarks (T_χ^l) and the deconfinement transition (T_d).

The Wuppertal group performed their calculations on lattices with temporal extents $N_\tau = 4, 6, 8, 10$, using so-called stout-link improved fermions at physical quark masses [29]. They report different values for the transition obtained from the chiral susceptibility (T_χ^l), the strange susceptibility (T_χ^s) and the renormalized Polyakov loop (T_d):

$$T_\chi^l = 151(3)(3)\,\mathrm{MeV}\ , \quad T_\chi^s = 175(2)(4)\,\mathrm{MeV}\ , \quad T_d = 176(3)(4)\,\mathrm{MeV}\ . \tag{2.8}$$

The reasons for the different results of the two lattice groups is only partially understood. The most important issue is the conversion of lattice results to physical units. For a more detailed discussion, see [29, 13]. The issue of the transition temperature is clearly not settled and further calculations using finer lattices and physical quark masses are required. In [28] it is stated, that the change from the previously assumed value $T \sim 175\,\mathrm{MeV}$ is mainly due to a different values of the Sommer parameter r_0 used for the scale fixing.

Both groups agree that the transition at vanishing chemical potential is a crossover. This result is extracted from the scaling behavior of the peak of the chiral susceptibility as a function of the system volume V. For a first-order transition the height should scale like V and the width like $1/V$. For a second-order transition the height scales with V^α with a critical exponent α depending on the details of the transition. The current calculations of the Wuppertal group [17] and the RBC-Bielefeld show no volume dependence, indicating a crossover at vanishing chemical potential.

At finite quark chemical potential $\mu_q > 0$, the Monte Carlo evaluation of the QCD partition function is impossible because of the Fermion sign problem. While all physical observables remain real, the Fermion determinant becomes complex due to the γ_5 hermicity of the Dirac operator

$$\not{D}(\mu)^\dagger = (\not{D} + m_f - \mu_f\gamma_0)^\dagger = \gamma_5\not{D}(-\mu^*)\gamma_5\ . \tag{2.9}$$

Hence, it looses its interpretation as a probability weight in the importance sampling of the Monte Carlo simulation.

In the last years several methods have been proposed to tackle this problem, namely Taylor expansion [30, 31, 32], reweighting [33], imaginary chemical potential [34, 35] and canonical ensemble [36, 37]. An overview of these methods can be found in [13].

The Taylor expansion will be discussed in more detail in Chap. 6.

2.2.2. Effective models

While the microscopic degrees of freedom in QCD are the quarks and gluons, the degrees of freedom most suitable for an effective description of the theory depend on the considered scale. At scales above 2 GeV, quarks and gluons are the relevant degrees of freedom. In this region the coupling constant becomes weak and the remaining interactions can be described using perturbation theory on top of a gas of free quarks and gluons. At smaller scales the interaction becomes stronger and composite objects are formed. Below the QCD phase transition the relevant macroscopic degrees of freedom are hadrons.

The hadronic degrees of freedom are color-blind, so for the construction of effective models one has to rely on the chiral symmetry of QCD. We will later use an effective linear sigma model which implements the chiral symmetry in the hadronic sector and incorporate additional quark degrees of freedom. Note, that these models are expected to work best in the vicinity of the phase transition. Probably the most studied model is the Nambu–Jona-Lasinio (NJL) model [38, 39]. This model is not considered in this work, a review can be found in [40].

The gluonic degrees of freedom are integrated out and are only effectively included in the coupling constants, but not as explicit degrees of freedom. Thus, the chiral models do not implement the $Z(N_c)$ symmetry related to the confinement transition. This symmetry can be integrated in the models by coupling the Polyakov loop to the fermionic degrees of freedom, an approach that will be discussed in details in Chap. 4.

2.3. Experimental insights

The extreme conditions at which strongly interacting matter is expected to undergo a phase transition can be reached experimentally in ultra-relativistic heavy-ion collisions. Currently, these experiments are concentrated at the Relativistic Heavy Ion Collider (RHIC) at Brookhaven National Laboratory. Future experiments are planed at the Large Hadron Collider (LHC) at CERN and at the future Facility for Antiproton and Ion Research (FAIR) in Darmstadt.

In heavy-ion collisions, the number of particles is large enough that the system behaves like matter and not like single particles. To allow for the definition of different phases and thermodynamic properties the system has to reach a local (approximate) equilibrium state. The hadrons emitted at the late stage of the collision can be described by fitting a statistical model with parameters T and μ to the measured ratio of particle yields (for a review see e.g., [41]). Since the particle ratios are fixed at this point in the collision, this scenario is dubbed chemical freeze-out. It supports the assumption that at least some equilibration was reached. In Fig. 2.4 we show a plot of chemical freeze-out points in a phase diagram. Additionally predictions of the phase boundary in a Bag-model calculation and in a lattice calculation are shown. The solid line indicates

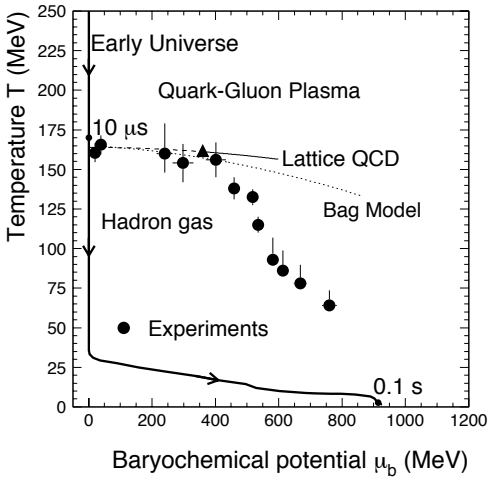

Figure 2.4.: Phase diagram of the chemical freeze-out points determined in experiments. Also shown are lattice predictions and a model calculation in the Bag-model. The solid line indicates the path along which the early universe cooled down and passed the QCD phase boundary. Figure taken from [11].

the path the early universe passed during its evolution at times from $10\,\mu s$ to $0.1s$ after the Big Bang. Note that the shown lattice data still assume a phase transition at zero chemical potential at $T_\chi \sim 175\,\mathrm{MeV}$. Using these older lattice values, there is a striking coincidence of the freeze-out points with lattice data for small chemical potentials. At higher chemical potentials the lattice data are questionable anyway. The interpretation of this phenomenon is somewhat involved and details differ, but it is assumed that the freeze-out curve is closely linked to the deconfinement transition. The LHC experiments will hopefully provide more insight in this region at small chemical potentials.

The freeze-out points are just one information gained from these heavy-ion experiments. Many other observables that encode information on the different stages are available. More information can be found in several reviews, e.g. [11, 41, 42, 43]

The CBM experiment [44] at the planned FAIR facility in Darmstadt will focus on a region at higher chemical potentials and lower temperatures. It might therefore be able – if a critical point exists – to provide further insight on the location of the critical end point. The critical end point is characterized by large fluctuations. To find an experimental signal for the CEP one has to scan the region of the phase diagram around the CEP where fluctuations become dominating. The probability of finding this signal depends on the size of this critical region, which will be subject of Chap. 5.

3. Chiral symmetry restoration

In this chapter we will discuss the effects of the chiral symmetry restoration in strongly interacting matter. In the chiral limit ($m_f = 0$) the QCD Lagrangian (2.1) is invariant under global chiral $U(N_f)_r \times U(N_f)_l$ transformations. The group $U(N_f)_r \times U(N_f)_l$ is isomorphic to the group $U(N_f)_V \times U(N_f)_A$ of axial and vector transformations, $A = r - l$, $V = r + l$. Moreover the $U(N_f)$, group can be split into a product of a special unitary group $SU(N_f)$ and a complex phase, $U(N_f) \cong SU(N_f) \times U(1)$. Thus, finally,

$$U(N_f)_r \times U(N_f)_l \cong SU(N_f)_V \times SU(N_f)_A \times U(1)_A \times U(1)_V \ . \tag{3.1}$$

The vector subgroup $U(1)_V$ corresponds to the baryon number conservation and will be omitted since this symmetry is always satisfied. The axial $U(1)_A$ symmetry is explicitly broken by instantons. This is the $U(1)_A$ anomaly of QCD [45].

Finite quark masses explicitly break all axial symmetries, whereas the vector symmetries are partly conserved for degenerated quark masses. In nature, the up and down quarks have approximately the same mass, $m_u \approx m_d$, and correspondingly a $SU(2)_V$ symmetry is conserved.

Apart from the explicit breaking, the chiral symmetry is broken spontaneously by the finite expectation value of the chiral condensate. According to Goldstone's theorem, a massless Goldstone boson appears for each broken generator [46]. For three quark flavors these are the three pions, four kaons and the η. Due to the explicit chiral symmetry breaking they are not massless. The pions are indeed very light, while the mesons carrying strangeness are heavier because of the stronger breaking of the chiral symmetry in the strange sector.

At high temperatures the symmetry is restored to $SU(N_f)_r \times SU(N_f)_l$ or even $SU(N_f)_r \times SU(N_f)_l \times U(1)_A$, depending on the restoration of the $U(1)_A$ symmetry at higher temperatures. At high temperatures instantons should be screened and an effective restoration of the $U(1)_A$ symmetry is expected [12].

We will discuss the chiral symmetry restoration in the framework of an effective linear sigma model (LσM) with three quark flavors, also known as the quark-meson (QM) model. It includes mesonic and quark degrees of freedom. In the region of the phase transition ($\mathcal{O}(10^2)$ MeV) these are the relevant degrees of freedom, which justifies its use as an effective model for the QCD phase transition. The LσM with three quark flavors has a $SU(3)_r \times SU(3)_l \times U_1(A)$ symmetry. The chiral symmetry will be broken explicitly to obtain a realistic scenario with two light quark flavors and a heavier strange quark. This will break down the symmetry to $SU(2)_V \times U(1)_A$. The influence of the breaking of the $U(1)_A$ symmetry will be explicitly considered. Thus, the LσM can serve as a model to explore the effects of chiral symmetry breaking. Furthermore the LσM with three quark flavor has the benefit of renormalizability.

3.1. Linear sigma model with three quark flavors

The Lagrangian $\mathcal{L}_{qm} = \mathcal{L}_q + \mathcal{L}_m$ of the LσM with three quark flavors consists of the fermionic part

$$\mathcal{L}_q = \bar{q}\left(i\partial\!\!\!/ - gT_a\left(\sigma_a + i\gamma_5\pi_a\right)\right)q \tag{3.2}$$

with a flavor-blind Yukawa coupling g of the quarks to the mesons, and the purely mesonic contribution

$$\begin{aligned}\mathcal{L}_m &= \mathrm{Tr}\left(\partial_\mu\phi^\dagger\partial^\mu\phi\right) - m^2\,\mathrm{Tr}(\phi^\dagger\phi) - \lambda_1\left[\mathrm{Tr}(\phi^\dagger\phi)\right]^2 \\ &\quad -\lambda_2\,\mathrm{Tr}\left(\phi^\dagger\phi\right)^2 + c\left(\det(\phi) + \det(\phi^\dagger)\right) \\ &\quad + \mathrm{Tr}\left[H(\phi + \phi^\dagger)\right]\ .\end{aligned} \tag{3.3}$$

The column vector $q = (u, d, s)$ denotes the quark field for $N_f = 3$ flavors and $N_c = 3$ color degrees of freedom. The ϕ-field represents a complex (3×3)-matrix and is defined in terms of the scalar σ_a and the pseudoscalar π_a meson nonet

$$\phi = T_a\phi_a = T_a\left(\sigma_a + i\pi_a\right)\ . \tag{3.4}$$

The $T_a = \lambda_a/2$ with $a = 0, \ldots, 8$ are the nine generators of the $U(3)$ symmetry, where the λ_a are the usual eight Gell-Mann matrices and $\lambda_0 = \sqrt{\frac{2}{3}}\,\mathbf{1}$.

Chiral symmetry is broken explicitly by the last term in Eq. (3.3), where $H = T_a h_a$ is a (3×3)-matrix with nine components h_a. In general, one could add further explicit symmetry-breaking terms to $\mathcal{L}_m$ which are non-linear in ϕ [47, 48], but this will not be considered in this work. Only three components (h_0, h_3, h_8) of the explicit symmetry-breaking matrix H may be non-zero, because the expectation value of ϕ does not carry the correct quantum numbers of the vacuum otherwise. Since T_0 is proportional to the unit matrix it adds a uniform symmetry breaking to all three quark flavors, i.e., $h_0 \neq 0, h_3 = 0, h_8 = 0$ corresponds to the limit of three degenerate quark flavors. h_8 introduces a splitting between the light (u, d) and the heavier strange (s) quark flavors. This situation will be considered in this work. The $SU(2)_V$ isospin symmetry is broken by a term $\propto T_3$. We will consider only the case $m_u = m_d$ and set $h_3 = 0$. With this explicit symmetry breaking pattern two condensates $(\bar{\sigma}_0, \bar{\sigma}_8)$ develop a non-zero expectation value in the vacuum. A more detailed discussion of the symmetry-breaking patterns in this model can be found in App. A.1 and [49].

3.1.1. Grand potential

In this section the grand potential is derived in a mean-field approximation previously also used in works with two quark flavors [50, 51]. We start from the partition function in Euclidean space. It is defined by a path integral over the quark/antiquark and mesonic fields

$$\mathcal{Z} = \int \prod_a \mathcal{D}\sigma_a \mathcal{D}\pi_a \int \mathcal{D}q\mathcal{D}\bar{q} \exp\left(- \int_0^{1/T} d\tau \int_V d^3x \mathcal{L}^E \right), \tag{3.5}$$

where T is the temperature and V the three-dimensional volume of the system. For three quark flavors the Euclidean Lagrangian $\mathcal{L}^E$ contains three independent quark chemical potentials μ_f in general:

$$\mathcal{L}^E = \mathcal{L}_{qm} + \sum_{f=u,d,s} \mu_f q_f^\dagger q_f \ .$$

The index f denotes the quark flavors. Since we do not consider a breaking of the $SU(2)_V$ isospin symmetry, we will use the index $l = u, d$ for the light up and down quarks, i.e., $\mu_l \equiv \mu_u = \mu_d$ and $m_l \equiv m_u = m_d$. Throughout this work we will further use the notation

$$\mu_q \equiv \mu_B/3 = \mu_l = \mu_s \tag{3.6}$$

for a uniform chemical potential for all quark flavors and $\mu = (\mu_l, \mu_s)$.

In the evaluation of the partition function we neglect quantum and thermal fluctuations of the mesonic fields. The integration over the mesonic fields is dropped and the mesonic fields are replaced by their expectation values $\bar{\phi} = T_0\bar{\sigma}_0 + T_8\bar{\sigma}_8$, resulting in the mesonic potential $U(\sigma_0, \sigma_8)$. The quarks are treated as quantum fields. The integration over the quark fields yields a determinant which can be rewritten as a trace over a logarithm. Using the Matsubara formalism this results in the quark contribution [52]

$$\Omega_{\bar{q}q}(T, \mu) = \nu_c T \sum_{f=u,d,s} \int_0^\infty \frac{d^3k}{(2\pi)^3} \left\{ \ln(1 - n_{q,f}(T, \mu_f)) + \ln(1 - n_{\bar{q},f}(T, \mu_f)) \right\} \tag{3.7}$$

with the usual fermionic occupation numbers for the quarks and antiquarks

$$n_{q,f}\left(T, \mu_f\right) = \frac{1}{1 + \exp\left((E_{q,f} - \mu_f)/T\right)} \ , \quad n_{\bar{q},f}(T, \mu_f) \equiv n_{q,f}(T, -\mu_f) \ . \tag{3.8}$$

The number of internal quark degrees of freedom is denoted by $\nu_c = 2N_c = 6$. The flavor-dependent single-particle energies are

$$E_{q,f} = \sqrt{k^2 + m_f^2} \ , \tag{3.9}$$

with flavor-dependent quark masses m_f which are also functions of the expectation values $\bar{\sigma}_0$ and $\bar{\sigma}_8$.

The total grand potential is given by

$$\Omega(T,\mu) = \frac{-T\ln\mathcal{Z}}{V} = U\left(\bar{\sigma}_0,\bar{\sigma}_8\right) + \Omega_{\bar{q}q}(T,\mu)\ . \tag{3.10}$$

The vacuum condensates $\bar{\sigma}_0$ and $\bar{\sigma}_8$ are members of the scalar ($J^P = 0^+$) nonet and both contain strange and non-strange components. This can also be seen in the expressions for the light and strange constituent quark masses:

$$m_l^2 = \frac{g^2}{12}\left(2\sigma_0^2 + 2\sqrt{2}\sigma_0\sigma_8 + \sigma_8^2\right)\ , \quad m_s^2 = \frac{g^2}{12}\left(2\sigma_0^2 - 4\sqrt{2}\sigma_0\sigma_8 + 4\sigma_8^2\right)\ . \tag{3.11}$$

Using an orthogonal basis transformation from the original octet-singlet basis (σ_0,σ_8) to a non-strange (σ_x) and strange (σ_y) quark-flavor basis

$$\begin{pmatrix}\sigma_x\\ \sigma_y\end{pmatrix} = \frac{1}{\sqrt{3}}\begin{pmatrix}\sqrt{2} & 1\\ 1 & -\sqrt{2}\end{pmatrix}\begin{pmatrix}\sigma_0\\ \sigma_8\end{pmatrix}\ , \tag{3.12}$$

a more convenient notation can be obtained. The light-quark sector decouples from the strange-quark sector (cf. e.g. [53]) and the quark masses simplify to

$$m_l = g\sigma_x/2 \quad , \quad m_s = g\sigma_y/\sqrt{2}\ . \tag{3.13}$$

The meson potential is then explicitly given by

$$\begin{aligned} U(\sigma_x,\sigma_y) = \frac{m^2}{2}\left(\sigma_x^2+\sigma_y^2\right) - h_x\sigma_x - h_y\sigma_y - \frac{c}{2\sqrt{2}}\sigma_x^2\sigma_y \\ + \frac{\lambda_1}{2}\sigma_x^2\sigma_y^2 + \frac{1}{8}\left(2\lambda_1+\lambda_2\right)\sigma_x^4 + \frac{1}{8}\left(2\lambda_1+2\lambda_2\right)\sigma_y^4\ . \end{aligned} \tag{3.14}$$

Here the explicit symmetry-breaking parameters h_0 and h_8 have also been transformed according to Eq. (3.12).

The order parameters for the chiral phase transition are identified with the expectation values $\bar{\sigma}_x$ for the non-strange and $\bar{\sigma}_y$ for the strange sector. They are obtained by minimizing the grand potential (3.10) in the non-strange and strange directions

$$\frac{\partial\Omega}{\partial\sigma_x} = \frac{\partial\Omega}{\partial\sigma_y}\bigg|_{\sigma_x=\bar{\sigma}_x,\sigma_y=\bar{\sigma}_y} = 0\ . \tag{3.15}$$

The solutions of these coupled equations determine the behavior of the chiral order parameters as a function of T and the chemical potentials, μ_l and μ_s. Note that the in-medium condensates are also labeled with a bar over the corresponding fields.

3.1.2. Parameter fits

Using the grand potential of the LσM we now fix the parameters of the mesonic and the quark sector. Taking into account the explicit breaking of the $U(1)_A$ symmetry the mesonic sector requires the determination of six parameters m^2, λ_1, λ_2, c, h_x, h_y and two unknown condensates $\bar{\sigma}_x$ and $\bar{\sigma}_y$. They are fitted to experimental values in the vacuum. For five parameters we can use the well known pseudoscalar masses m_π, m_K, the averaged η, η' masses $m_\eta^2 + m_{\eta'}^2$ and the pseudoscalar decay constants f_π and f_K. Further input from the scalar mass spectrum is required to fix all parameters. This introduces some freedom in the choice of parameters since the mass of the broad sigma resonance is not precisely determined experimentally: the particle data group specifies a range $m_\sigma = 400 \ldots 1200\,\mathrm{MeV}$ [54]. Recent studies favor a value in the lower part of this range, $m_\sigma \sim 400 \ldots 600\,\mathrm{MeV}$ [55, 56].

We use the partially conserved axial-vector current (PCAC) relation to link the vacuum values of the condensates to the pseudoscalar decay constants f_π and f_K:

$$\bar{\sigma}_x = f_\pi \ , \qquad \bar{\sigma}_y = \frac{1}{\sqrt{2}} \left(2f_K - f_\pi\right) \ . \tag{3.16}$$

λ_2 and c can now be calculated using the tree-level expression for the pseudoscalar masses in the vacuum. The explicit formulae are given in App. A.2.

The average squared η and η' meson mass determines the parameter λ_2 by

$$\lambda_2 = \frac{3(2f_K - f_\pi)m_K^2 - (2f_K + f_\pi)m_\pi^2 - 2(m_{\eta'}^2 + m_\eta^2)(f_K - f_\pi)}{\left(3f_\pi^2 + 8f_K(f_K - f_\pi)\right)(f_K - f_\pi)} \ . \tag{3.17}$$

The strength c of the $U(1)_A$ anomaly is fixed by λ_2 and the difference of the squared pion and kaon masses via

$$c = \frac{m_K^2 - m_\pi^2}{f_K - f_\pi} - \lambda_2(2f_K - f_\pi) \ . \tag{3.18}$$

Without $U(1)_A$ breaking the η and η' are pure strange and non-strange states, respectively, and the η' meson is degenerate with the pion. In this case, only five parameters in the mesonic sector are needed and the averaged $m_\eta^2 + m_{\eta'}^2$ mass can be dropped as input. The parameter λ_2 can then be determined from the remaining pseudoscalar input values

$$\lambda_2 = \frac{m_K^2 - m_\pi^2}{(2f_K - f_\pi)}(f_K - f_\pi) \ . \tag{3.19}$$

With the input used so far, we can only determine a relation between λ_1 and m^2, e.g., using the formula for the pion mass and substituting the already known parameters. Using this relation in the expressions for the masses of the $(\sigma - f_0)$ sector, we can eliminate m^2 in these equations and determine λ_1 using m_σ (or m_{f_0}) as further input. m^2 is then also fixed via the relation between m^2 and λ_1.

In the quark sector the only parameter is the flavor-blind Yukawa coupling g. With the value for the non-strange condensate determined above, it is chosen such that

$$m_l = g\frac{\bar{\sigma}_x}{2} = 300\,\mathrm{MeV}. \tag{3.20}$$

Using the equations of motion (3.15) and the tree-level expressions for m_π and m_K (cf. App. A), the Ward identities

$$h_x = f_\pi m_\pi^2\ , \qquad h_y = \sqrt{2} f_K m_K^2 - \frac{f_\pi m_\pi^2}{\sqrt{2}}\ , \tag{3.21}$$

can be derived. They determine the values of the explicit symmetry-breaking parameters in the strange (h_y) and non-strange (h_x) directions. In the mean-field approximation these relations also hold at finite temperature and chemical potential. In this case the fermionic contribution to the equations of motion and masses (Eq. A.11) has to be taken into account.

As already stated above, the mass of the sigma resonance introduces some freedom in the choice of parameters. We will investigate its influence on our results by using different values. In App. A.1 we have collected the parameters for each m_σ (Tab. A.1) with and without explicit $U(1)_A$ breaking. The corresponding predictions of the scalar and pseudoscalar meson masses and mixing angles are listed in Tab. A.2

3.2. Chiral symmetry restoration

In this section the restoration of the chiral symmetry is discussed. A uniform quark chemical potential $\mu \equiv \mu_q$ for all quark flavors is assumed. In the following we will use the notations T_χ^l for the chiral transition of the light and T_χ^s for the chiral transition of the strange quarks. If not otherwise mentioned we refer to the values of T_χ^l, T_χ^s at vanishing chemical potential. Since we focus on the transition of the light quarks, we will also drop the index l when unambiguous, $T_\chi \equiv T_\chi^l$. The coordinates of the critical end point are labeled (T_c, μ_c).

3.2.1. Condensates

The gap equations (3.15) determine the behavior of the condensates as a function of T and μ. In Fig. 3.1(a), the non-strange ($\bar{\sigma}_x$) and strange ($\bar{\sigma}_y$) condensates are shown as a function of temperature at vanishing chemical potential for $m_\sigma = 800\,\mathrm{MeV}$. The solid lines are for the case with explicit $U(1)_A$ symmetry breaking, the dashed lines for the case without. Note that for the non-strange condensate the two lines are indistinguishable in the plots. For simplicity we refrain from showing a curve for the light condensate without $U(1)_A$ anomaly. The condensates start at the vacuum values determined via the PCAC relations (3.16) and show a smooth crossover behavior as the temperature

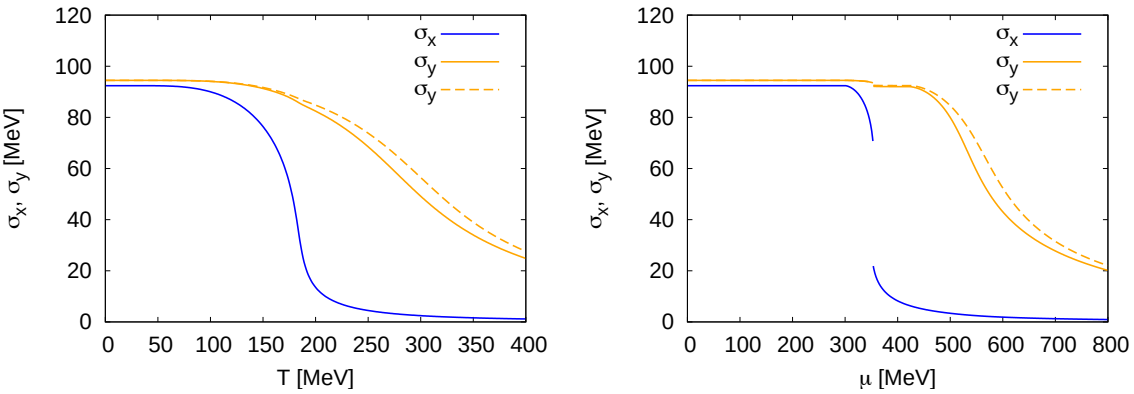

(a) $\mu = 0$ (b) $T = 0$

Figure 3.1.: The non-strange, $\bar{\sigma}_x$, and strange, $\bar{\sigma}_y$, condensates as a function of temperature for vanishing chemical potentials (left panel) and as a function of chemical potential for zero temperature (right panel) with (solid lines) and without $U(1)_A$ anomaly (dashed lines). The anomaly does not modify the non-strange condensate.

increases. The peak in the temperature derivative of the light condensates determines a pseudocritical temperature $T_\chi^l \sim 183\,\text{MeV}$. As expected, the strange condensate melts at higher temperatures due to the higher strange quark mass. Below the pseudocritical temperature T_χ^l the influence of the $U(1)_A$ anomaly is nearly invisible. At higher temperatures the strange condensate melts faster with $U(1)_A$ symmetry breaking. This can partly be understood from the mesonic potential (cf. Eq. 3.14): The anomaly introduces a term $\propto \sigma_x^2\sigma_y$. In the strange direction this term acts like a σ_x-dependent explicit symmetry breaking. At temperatures above the light pseudocritical temperature this additional explicit symmetry breaking in the strange direction is reduced with the melting light condensate and pulls down the strange condensate.

In Fig. 3.1(b) we show the condensates at zero temperature as a function of the chemical potential. Starting at their vacuum values, the condensates stay constant up to their corresponding Fermi surfaces at $\mu = m_l \sim 300\,\text{MeV}$ and $\mu = m_s \sim 433\,\text{MeV}$, respectively. At chemical potentials above the Fermi surface the light condensate starts to melt and exhibits a first order transition at $\mu \sim 352\,\text{MeV}$. The discontinuity in the light condensate also induces a small drop in the strange condensate. This is different from NJL studies where this induced jump is only seen if the $U(1)_A$ anomaly is taken into account. In the LσM with quarks both condensates are still coupled via the remaining terms in the mesonic potential, while in the NJL model the three flavors decouple and the thermodynamic potential is a sum over the quark flavors. The strange condensate shows a crossover behavior for chemical potentials above the strange constituent mass $\mu > m_s$. The explicit $U(1)_A$ symmetry breaking again results in a faster melting of the

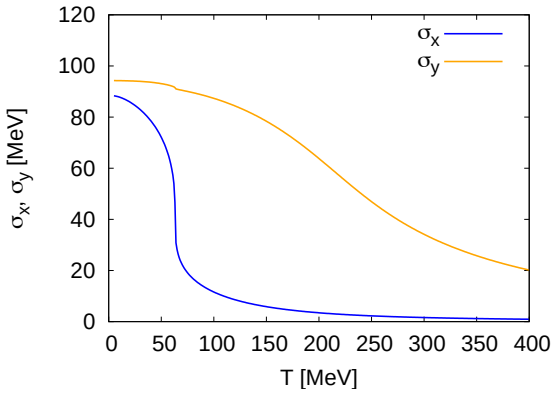

Figure 3.2.: Similar to Fig. 3.1(a) but for $\mu = \mu_c$ and only for the case with explicit $U(1)_A$ symmetry breaking.

strange condensate and no visible difference in the light condensate.

From these considerations we expect a critical end point for the light condensate. In Fig. 3.2 we show the condensates with explicit $U(1)_A$ symmetry breaking as a function of temperature for $\mu = \mu_c \sim 322\,\text{MeV}$. At $T \sim 63\,\text{MeV}$ the light condensate drops with an infinite slope signaling the second order phase transition expected at the critical end point (CEP). The strange condensate shows a very smooth crossover. Without $U(1)_A$ anomaly the behavior is similar though the position of the CEP is slightly shifted. The resulting phase diagram will be discussed in Sect. 3.3.

3.2.2. The scalar-pseudoscalar meson spectrum

To understand the restoration of chiral and $U(1)_A$ symmetry, a study of the meson masses is essential. Similar to the previous section we will discuss the meson spectrum at finite temperature and finite chemical potential as well as at the critical end point. The derivation of the in-medium masses and the mass formulae are collected in App. A.2.

In Figs. 3.3 and 3.4, we show the meson masses as a function of the temperature at vanishing chemical potential for $m_\sigma = 800\,\text{MeV}$. The left panels show the case with explicit $U(1)_A$ symmetry breaking while the right panels show the masses without explicit $U(1)_A$ symmetry breaking. In the broken phase the mesonic contribution to the masses dominates. It melts towards the chiral phase transition. Roughly at the pseudocritical temperature $T_\chi \sim 183\,\text{MeV}$ the masses of the pion and the σ meson degenerate as well as the a_0 and η' mesons. The rise of the masses is caused by the now dominating fermionic contribution. The mesons with net strangeness, K and κ, degenerate at higher temperatures $T \sim 240\,\text{MeV}$ and the f_0 becomes degenerate with its chiral partner η at even higher temperatures of $T \sim 300\,\text{MeV}$. These observations indicate the later chiral symmetry restoration in the strange sector already seen in the condensates (cf. Fig. 3.1(a)), where the inflection point for the strange condensate was

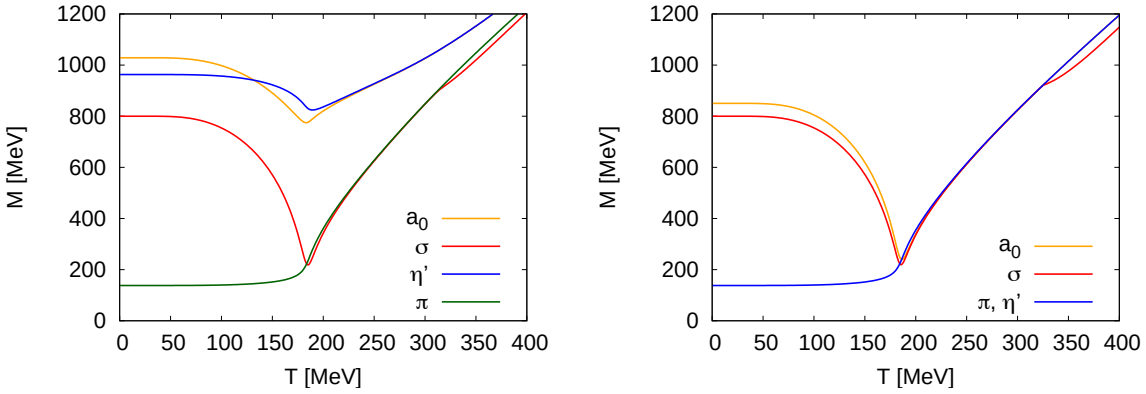

(a) with $U(1)_A$ symmetry breaking (b) without $U(1)_A$ symmetry breaking

Figure 3.3.: In-medium meson masses, (π, σ) and (η', a_0), as a function of temperature for $\mu = 0$ with $U(1)_A$ anomaly (left panel). Without anomaly (right panel) the η' meson mass is degenerate with the pion mass. See text for further details.

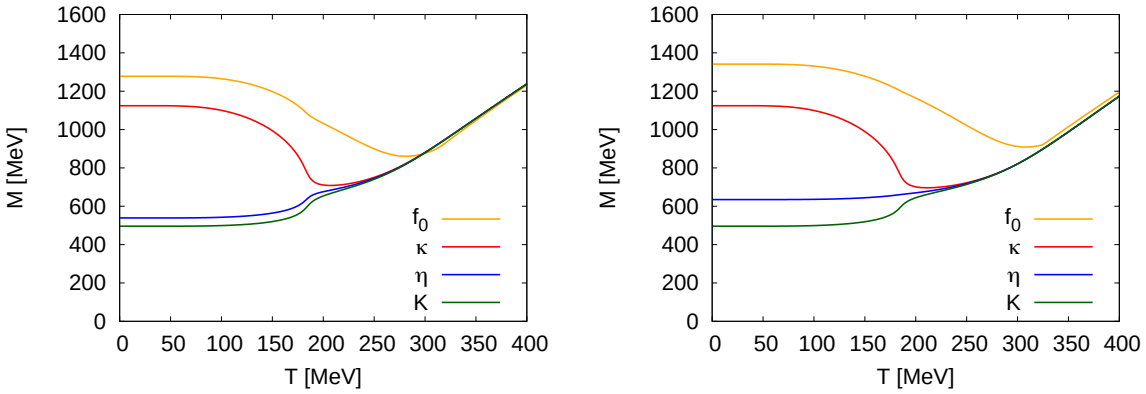

(a) with $U(1)_A$ symmetry breaking (b) without $U(1)_A$ symmetry breaking

Figure 3.4.: Similar to Fig. 3.3 for the chiral partners (η, f_0) and (K, κ) (left panel with $U(1)_A$ anomaly). Without anomaly (right panel) the η meson increases by about 100 MeV in the vacuum.

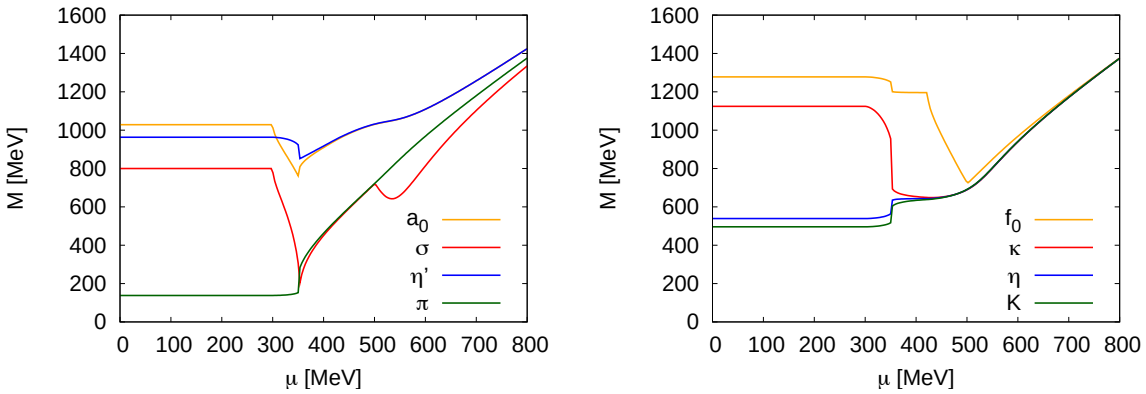

Figure 3.5.: In medium masses of the chiral partners similar to Figs. 3.3(a) and 3.4(a) with $U(1)_A$ anomaly as a function of μ for zero temperature.

found at $T \sim 300\,\mathrm{MeV}$.

Without anomaly (Fig. 3.3(b)) all mesons masses are degenerate at the pseudocritical temperature T_χ, while a gap remains between $m_\pi = m_\sigma$ and $m'_\eta = m_{a_0}$ with anomaly (Fig. 3.3(a)). This gap is due to a contribution of the anomaly with opposite signs to the meson masses (cf. App. A.2) and is proportional to $\sqrt{2}c\bar{\sigma}_y$. The non-strange condensate is already negligible for temperatures $T \gg T_\chi$. For very high temperatures, this mass gap decreases with the melting of the strange condensate and no remainder of the $U(1)_A$ anomaly is visible in the meson spectrum anymore. The kink in the mass of the f_0 meson seen in both cases will be discussed in connection with the flavor-mixing in Sect. 3.2.3.

In Fig. 3.5 the masses are shown for the case with $U(1)_A$ anomaly as a function of chemical potential at zero temperature. All masses stay at their vacuum value until the chemical potential reaches the Fermi surface for the light quarks at $\mu = 300\,\mathrm{MeV}$. The mass of the σ meson drops below the mass of the pion at the first-order transition located at $\mu \sim 352\,\mathrm{MeV}$. The masses of the pseudoscalar mesons stays nearly constant until the phase transition while the scalar mesons show a stronger melting above the Fermi surface for the light quarks. Only in the curve for the f_0 meson the Fermi surface for the strange quarks is clearly visible. The mass of the f_0 stays rather constant after the light phase transition until $\mu \sim m_s$. The slight drop of the f_0 mass at $\mu \sim 352\,\mathrm{MeV}$ is due to the induced drop in the strange condensate discussed in the previous subsection.

In Fig. 3.6 the masses are shown for the case with $U(1)_A$ anomaly as a function of temperature at the critical chemical potential μ_c. The most prominent feature in these plots is certainly the drop of the σ meson mass below the pion mass down to zero at the critical end point. This is a general feature of the LσM since the potential becomes flat at this point in the radial σ direction. In a similar NJL calculation this is not the case [51, 57]. A massless σ-meson can be copiously produced at the critical end point. In experiments these σ-mesons will decay once they leave the collision region and become

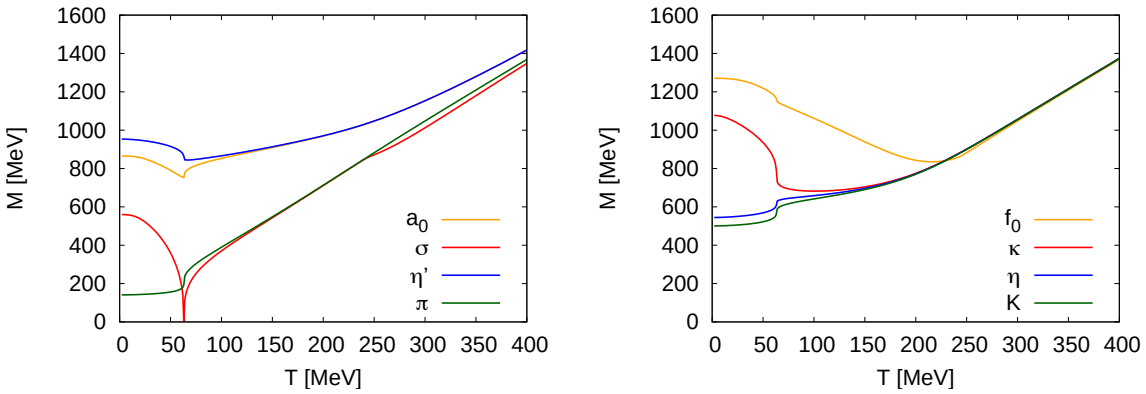

Figure 3.6.: In medium meson masses with $U(1)_A$ symmetry breaking similar to Figs. 3.3(a) and 3.4(a) as a function of T but at the critical chemical potential, $\mu = \mu_c$.

massive again. The resulting pions would be a further signal of the critical end point.

In the chiral limit with $c \neq 0$, a massless pseudoscalar octet and a finite $m_{\eta'} = 767$ MeV due to the $U(1)_A$ symmetry breaking are obtained. All scalar octet masses are degenerate at 840 MeV and the mass of the sigma meson drops to 620 MeV. Without $U(1)_A$ symmetry breaking all nine pseudoscalar mesons are massless and the scalar octet masses are degenerate at 780 MeV and $m_\sigma = 712$ MeV.

3.2.3. Flavor mixing at finite temperature and density

The flavor mixing in the scalar and pseudoscalar sector provides further insight on the $U(1)_A$ symmetry restoration. We will restrict the discussion to vanishing chemical potential and finite temperature. At finite chemical potential the mixing angles reveal the same qualitative behavior in the pseudoscalar as well as the scalar sector.

In the scalar sector the σ and f_0 mesons are admixtures of the singlet and octet states σ_0 and σ_8. The states are related to each other via a rotation:

$$\begin{pmatrix} |f_0\rangle \\ |\sigma\rangle \end{pmatrix} = \begin{pmatrix} \cos\theta_S & -\sin\theta_S \\ \sin\theta_S & \cos\theta_S \end{pmatrix} \begin{pmatrix} |\sigma_8\rangle \\ |\sigma_0\rangle \end{pmatrix} . \tag{3.22}$$

In the pseudoscalar sector the mixing is observed between the η and η' mesons:

$$\begin{pmatrix} |\eta\rangle \\ |\eta'\rangle \end{pmatrix} = \begin{pmatrix} \cos\theta_P & -\sin\theta_P \\ \sin\theta_P & \cos\theta_P \end{pmatrix} \begin{pmatrix} |\eta_8\rangle \\ |\eta_0\rangle \end{pmatrix} . \tag{3.23}$$

Similar relations also apply for the strange and non-strange states instead of the singlet-octet states. The details are given in App. A.3.

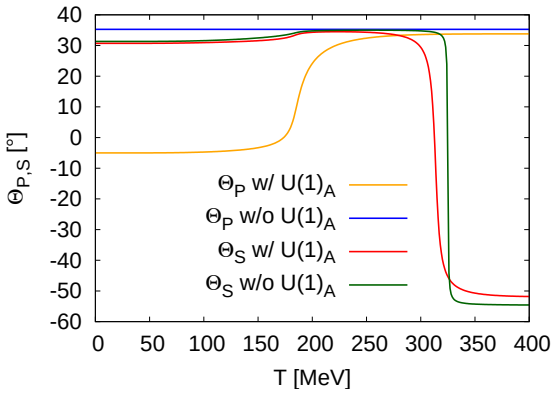

Figure 3.7.: The scalar θ_S and pseudoscalar θ_P mixing angles as a function of the temperature for $\mu = 0$ with and without $U(1)_A$ anomaly.

In Fig. 3.7 the scalar (θ_S) and pseudoscalar (θ_P) mixing angles in the singlet-octet basis are shown as functions of the temperature with and without explicit $U(1)_A$ symmetry breaking. The pseudoscalar mixing angle shows a clear influence of the $U(1)_A$ anomaly below the pseudocritical temperature. With $U(1)_A$ anomaly it starts at $\theta_P \sim -5°$ and rises to $\theta_P \to \arctan 1/\sqrt{2} \sim +35°$, corresponding to an ideal mixing, i.e., the (η, η') mesons are pure strange and non-strange states, respectively.

This can be seen in Fig. 3.8(a) where the η mesons and the corresponding pure strange η_S and non-strange components η_{NS} are shown as a function of the temperature. Above the pseudocritical temperature the η' approaches a pure non-strange state and the η a pure strange state.

Without $U(1)_A$ anomaly no flavor mixing is found in the pseudoscalar sector. The η' is always a pure non-strange state and degenerate with the pion. The mixing angle is ideal.

In the scalar sector the mixing angle θ_S shows no significant influence of the $U(1)_A$ anomaly. Starting with a value close to an ideal mixing ($\theta_S \sim 31°$) it rises towards the ideal value $\theta_S \sim 35°$ at the phase transition. For temperatures $T < 300\,\mathrm{MeV}$ the mixing angle drops from $\theta \sim +35°$ to $\theta \sim -54°$ from one ideal configuration to another ideal configuration. The qualitative behavior is the same with and without $U(1)_A$ anomaly, but the transition between the ideal values is smoother in the former case. The transition occurs slightly earlier at $T \sim 314\,\mathrm{MeV}$ with $U(1)_A$ anomaly, compared to $T \sim 325\,\mathrm{MeV}$ without. These values suggest a relation to the symmetry restoration in the strange sector. As discussed in the previous section, the strange condensate melts faster with $U(1)_A$ anomaly and the crossover happens at temperatures $T \sim 300\,\mathrm{MeV}$. The transition is very smooth in the strange sector and no sharp changes are expected, but the transition between the two ideal mixing angles happens clearly in the vicinity of the strange crossover transition. The transition between the two ideal mixings can be best understood from the comparison of the (σ, f_0) masses with the pure strange and non-strange

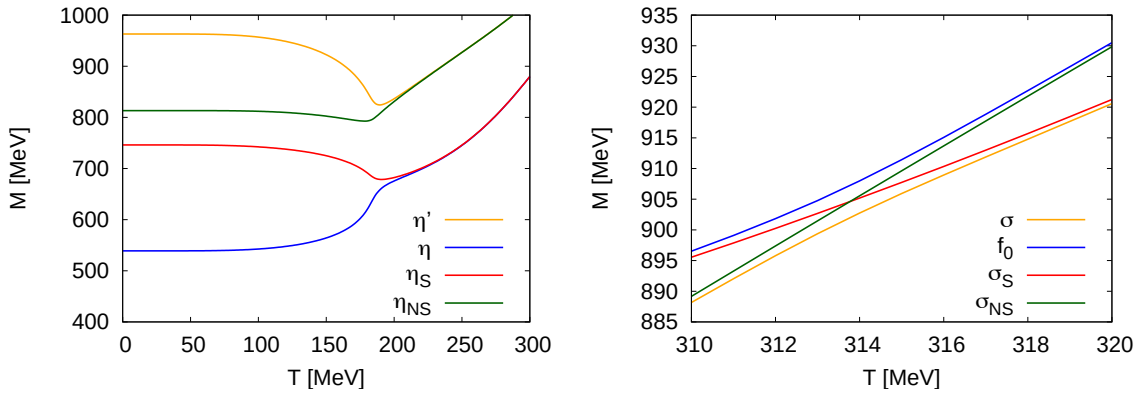

(a) η-η' (b) σ-f_0

Figure 3.8.: Left: Physical η-η' complex in comparison with the η_{NS}-η_{S} complex as a function of temperature at $\mu = 0$ with $U(1)_A$ anomaly. Right: The scalar physical σ-f_0 complex around $T \sim 314$ MeV in comparison with the σ_{NS}-σ_{S} system with $U(1)_A$ anomaly.

components (σ_S, σ_{NS}) shown in Fig. 3.8(b) with $U(1)_A$ anomaly. At $T \sim 310\,\mathrm{MeV}$ the σ is nearly degenerate with the non-strange component and the f_0 with the strange component. While the mass gap between the σ and f_0 meson stays virtually constant within the shown temperature range, the strange and non-strange components intersect at $T \sim 314\,\mathrm{MeV}$. Beyond this temperature the σ meson becomes quasi-degenerate with the strange component. This also explains the kink seen in the discussion of the meson spectrum in the previous section. When σ and f_0 are interchanged in the meson spectrum with anomaly for $T > 314\,\mathrm{MeV}$ the kink vanishes. For very high temperatures $T \gg 800\,\mathrm{MeV}$ the situation is reversed again and the σ becomes the pure non-strange state as the non-strange component drops below the strange component of the masses again.

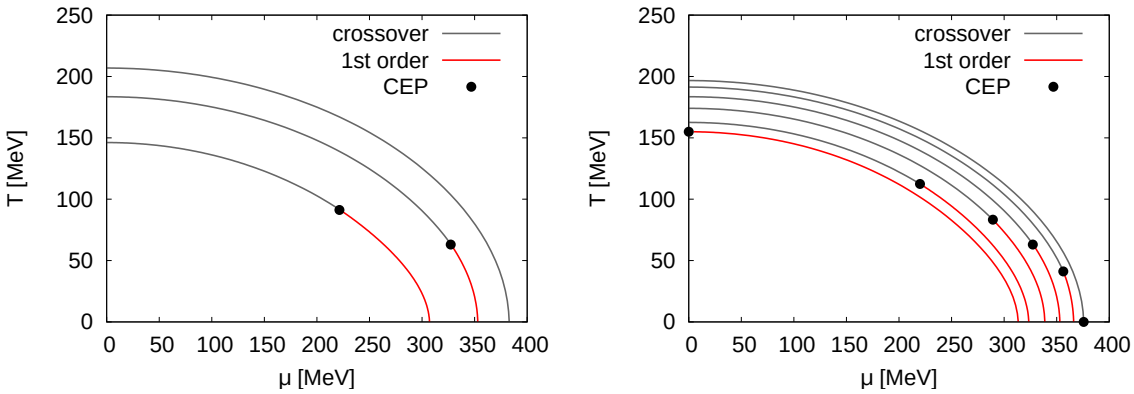

(a) $m_\sigma = 600, 800, 900\,\mathrm{MeV}$ (b) $m_\pi = 0.6 \ldots 1.36\, m_\pi^*$

Figure 3.9.: Left: Phase diagrams with $U(1)_A$ anomaly for different values of $m_\sigma = 600\,\mathrm{MeV}$ (lower line), $800\,\mathrm{MeV}$, $900\,\mathrm{MeV}$ (upper line). Right: Phase diagrams with $U(1)_A$ anomaly for $m_\sigma = 800$ MeV and different pion masses: $m_\pi/m_\pi^* = 0.488$ (lower line), $0.6, 0.8, 1.0, 1.2, 1.36$ (upper line), $m_\pi^* = 138\,\mathrm{MeV}$, $m_K^* = 496\,\mathrm{MeV}$. The ratio $m_\pi/m_K = m_\pi^*/m_K^*$ is kept fixed.

3.3. Phase diagram and the chiral critical surface

In this section we will discuss the influence of various parameters on the phase diagram of the LσM with three quark flavors. The phase diagram is constructed in the following way: for realistic pion and kaon masses (the so-called physical point) the light condensate always melts faster with T and/or μ than the strange condensate because the strange quark is heavier than the light quarks. The chiral phase boundary is determined by the inflection point in the non-strange condensate.

Later on, we will also vary the meson masses and calculate the corresponding phase diagrams. As a consequence, the ordering of the non-strange and strange condensates can be inverted since the kaon can become lighter than the pion. In such cases, the strange condensate drops more rapidly than the non-strange condensate, and the chiral phase transition is triggered by the strange condensate. This has to be taken into account systematically, in particular for the calculation of the chiral critical surface. The faster melting condensate has been used in order to localize the phase boundary.

In Fig. 3.9(a) the phase diagrams for various values of the mass of the σ-meson are shown. For each curve the parameters are refitted; the values of the parameters and the predicted meson masses and mixing angles can be found in App. A.2. The explicit $U(1)_A$ symmetry breaking affects the phase diagram at the physical point only weakly, hence only the curves with explicit $U(1)_A$ symmetry breaking are shown. The crossover phase transition observed at zero chemical potential shows a significant dependence on

the value of m_σ. The pseudocritical temperatures are $T_\chi^l \sim 146, 183, 207\,\mathrm{MeV}$ for σ-meson masses 600, 800, 900 MeV, respectively. This is compatible with the range given by recent lattice calculations (cf. Sect. 2.2.1, [17, 28]), although the lowest and highest values are at the outer bounds of the error band. Moreover it is known that models without Polyakov loop fail in a description of lattice results and these comparisons should not be overstressed. For zero temperature we find a crossover transition for $m_\sigma = 900\,\mathrm{MeV}$ and correspondingly no CEP is observed. For lower values of m_σ a first order transition at zero temperature is observed and a CEP is found. The weak influence of the $U(1)_A$ anomaly on the phase diagram can be seen in the location of the CEPs. For a σ mass of $m_\sigma = 800\,\mathrm{MeV}$, the CEP is located at $(T_c, \mu_c) = (63, 327)\,\mathrm{MeV}$ with $U(1)_A$ anomaly and only slightly shifted to $(T_c, \mu_c) = (63, 328)\,\mathrm{MeV}$ without. For a lower sigma mass $m_\sigma = 600\,\mathrm{MeV}$ the influence is stronger but still weak. The CEP moves from $(T_c, \mu_c) = (91, 221)\,\mathrm{MeV}$ with anomaly to $(T_c, \mu_c) = (89, 228)\,\mathrm{MeV}$ without anomaly. The weak influence of the anomaly for physical pion and kaon masses also shows up in the chiral critical surface which will be discussed later in this section.

As a first step towards the chiral critical surface, the dependence of the phase diagrams on the pion and kaon masses is shown in Fig. 3.9(b). We interpolate from the chiral limit to the physical point denoted by the values $m_\pi^* = 138\,\mathrm{MeV}$ and $m_K^* = 496\,\mathrm{MeV}$, using a common scaling factor for both masses

$$m_\pi = a\, m_\pi^* \,, \quad m_K = a\, m_K^* \,, \tag{3.24}$$

thereby keeping the ratio $m_\pi/m_K = m_\pi^*/m_K^*$ fixed. Only the explicit symmetry breaking parameters h_x and h_y are varied to tune pion and kaon masses to the desired values. All other parameters are kept fixed at their values obtained at the physical point. The transition lines shrink towards the origin for smaller pion and kaon masses. When the axes are rescaled with the corresponding critical values all curves fall on top of each other. For a pion mass $m_\pi \sim 0.488 m_\pi^*$, the critical end point is found on the T-axis, while for even smaller values of the pion mass the transition is always first order. A similar result has been found in a two-flavor calculation where the CEP also vanishes for a pion mass of $m_\pi \sim 69\,\mathrm{MeV}$, but for a different sigma mass $m_\sigma = 600\,\mathrm{MeV}$ and without $U(1)_A$ anomaly [50]. Using RG arguments it has been shown that for three quarks a first order transition is expected in the chiral limit [18], thus the vanishing of the CEP is expected. For higher pion masses, the critical end point moves towards higher chemical potentials, reaches the μ-axis for $m_\pi = 1.36 m_\pi^*$ and vanishes for even higher pion masses. The transition is always a crossover in these cases.

When we allow the kaon and pion mass to be tuned independently, we can calculate the critical surface. It is defined by the value of the critical chemical potential μ_c of the CEP for a given mass pair (m_π, m_K). For $\mu > \mu_c$ the chiral transition is of first order, while for values below the surface the transition lies in the crossover region. We have chosen to tune the masses of the light pseudoscalar mesons m_π and m_K instead of the bare quark masses, since the latter are not directly accessible in the model. This approach

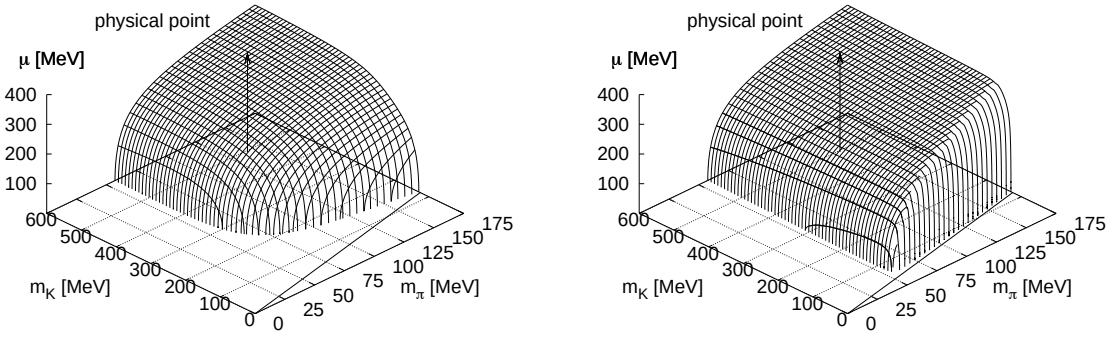

(a) with $U(1)_A$ anomaly (b) without $U(1)_A$ anomaly

Figure 3.10.: The chiral critical surface in the (m_π, m_K) plane for $m_\sigma = 800$ MeV. The arrow points to the critical quark chemical potential at realistic pion and kaon masses (physical point). The solid line corresponds to $m_K = m_\pi\sqrt{f_\pi/2f_K}$.

has also been used in previous works within the $L\sigma M$ with and without quarks [53, 58]. The explicit symmetry breaking parameters used to tune the pseudoscalar masses can be related to the bare quark masses [58, 9].

In Fig. 3.10, the chiral critical surface is shown with (left panel) and without (right panel) $U(1)_A$ anomaly. The physical point is indicated by an arrow. From the requirement $h_y > 0$ one can derive the condition $m_K > m_\pi\sqrt{f_\pi/2f_K}$. The resulting boundary is drawn as solid line in the (m_π, m_K)-plane. With and without anomaly the critical surface grows perpendicular from the (m_π, m_K)-mass plane at $\mu = 0$. The tangent plane to the critical surface has a decreasing slope for larger masses, as expected from Fig. 3.9(b). Thus, this model study excludes the so-called non-standard scenario where the first-order region shrinks as the chemical potential is turned on (cf. Sect. 2.1, [19]). In this non-standard scenario the bending of the critical surface has the opposite sign, and the physical mass point remains in the crossover region for any μ.

The phase transition is found to be first order everywhere for pion masses $m_\pi \lesssim 50\,\text{MeV}$, and no critical end point is found. This first order region is larger with $U(1)_A$ anomaly. For $m_\pi = 0$ no critical kaon mass is found. This is probably an artifact of the used mean-field approximation. For very high kaon masses the strange quarks are completely suppressed due to their mass and the dynamics is only driven by the two light flavors. In two-flavor mean field calculations a first-order transition was found in the chiral limit [50]. From universality arguments a second-order transition is expected, which was also found in a renormalization group (RG) calculation [50]. We expect to find a critical kaon mass when calculations are performed using RG techniques.

Only for very small kaon masses below the pion mass the chiral critical surface drops towards zero and the critical end point vanishes. Note that the strange quark becomes

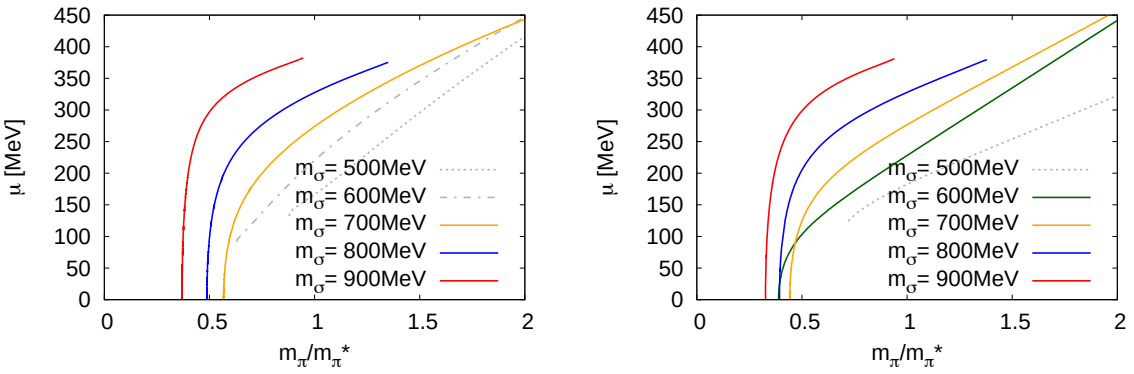

(a) with $U(1)_A$ anomaly (b) without $U(1)_A$ anomaly

Figure 3.11.: Five cross sections of the chiral critical surface (left panel with, right panel without anomaly) for $m_\sigma = 500, \ldots 900$ MeV. As trajectory in the (m_π, m_K) plane we have chosen the path through the physical point towards the chiral limit, i.e., we have kept the ratio of $m_\pi/m_K = m_\pi^*/m_K^*$ fixed. m_π^* and m_K^* denote the physical masses. See text for details.

lighter than the up and down quarks in this region. In general, the variation of the kaon mass has only a limited impact on the critical surface at finite μ without $U(1)_A$ anomaly. With anomaly, the influence of the kaon mass is weak only for kaon masses $m_K \gtrsim 400\,\text{MeV}$. In this region, both surfaces are nearly identical and no influence of the $U(1)_A$ anomaly is discernible. The influence of the strange quark on the phase transition in this region is strongly suppressed by the high strange quark mass. This is in accordance with the findings from the comparison of phase diagrams at the physical point with two and three flavors[1]. The dynamics of the strange quarks effectively decouples from the light sector that drives the chiral phase transition

The rather symmetric shape under the exchange of m_π and m_K without $U(1)_A$ anomaly can be understood from the mesonic potential. For $c = 0$ it is nearly invariant under a transformation $\sigma_x \leftrightarrow \sigma_y$ and $h_x \leftrightarrow h_y$. Only the coupling of the quartic term (cf. Eq. 3.14) changes from $\frac{1}{8}(2\lambda_1 + \lambda_2)$ to $\frac{1}{8}(2\lambda_1 + 2\lambda_2)$. In the fermionic sector the degeneracy of the up and down quark and the factor of $\sqrt{2}$ in the constituent masses is changed. This is an additional effect only present in the $L\sigma M$ with quarks. With $U(1)_A$ anomaly the term $\frac{c}{2\sqrt{2}}\sigma_x^2\sigma_y$ in the mesonic potential also changes the functional form of the mesonic potential.

The mass of the sigma meson has already proven to have a significant impact on the location of the CEP (cf. Fig.3.9(a)). Instead of plotting the whole chiral critical surface the path from the chiral limit to the physical point with $m_\pi/m_K = m_\pi^*/m_k^*$ is considered as in Fig.3.9(b). The resulting cuts are shown in Fig. 3.11 with and without

[1]Two-flavor results can be found in [50].

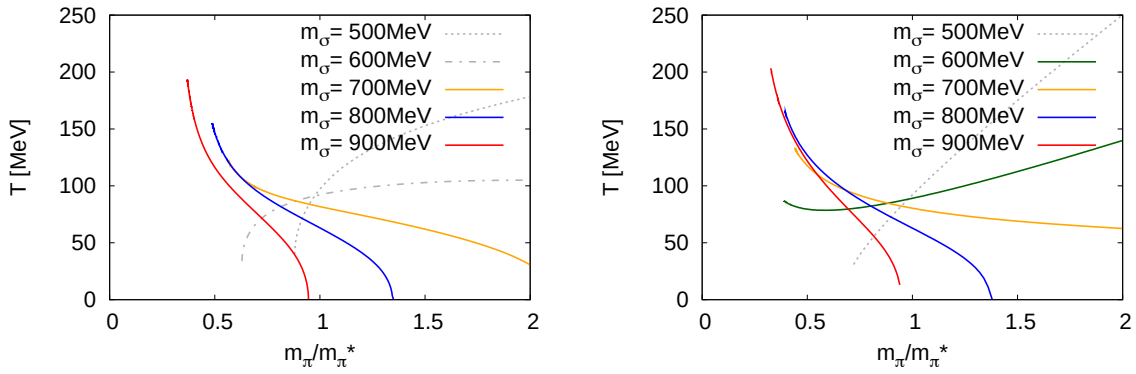

(a) with $U(1)_A$ anomaly

(b) without $U(1)_A$ anomaly

Figure 3.12.: Similar to Fig. 3.11, but the critical chemical potentials are replaced by the corresponding critical temperatures.

$U(1)_A$ anomaly. The critical lines are displayed for sigma meson masses in the range $m_\sigma = 500 \ldots 900\,\mathrm{MeV}$. The lines for $m_\sigma = 800\,\mathrm{MeV}$ were already included in the chiral critical surface in Fig. 3.10. All curves bend towards higher pion masses corresponding to the standard scenario of the QCD phase diagram. For $m_\sigma = 900\,\mathrm{MeV}$, the critical line ends for pion masses below the physical pion mass. This was already expected since no CEP was found in the phase diagram (cf. Fig.3.9(a)) for this value of the sigma mass. At the physical point the CEP is already pushed below the μ axis. To gain further insight it is instructive to consider the critical temperature T_c as a function of the meson masses as well. This is shown Fig. 3.12, where the critical chemical potential has been replaced with the critical temperature T_c.

With decreasing σ mass the critical line extends to higher pion masses and bends towards higher masses already at lower chemical potentials. For $m_\sigma = 700\,\mathrm{MeV}$, the critical end point is not pushed on the μ-axis in the shown range and a critical end point is always found. For the lower sigma masses, $m_\sigma = 500, 600\,\mathrm{MeV}$ (with anomaly) and $m_\sigma = 500\,\mathrm{MeV}$ (without anomaly) the parameter m^2 becomes positive (cf. A.1). For these values no spontaneous symmetry breaking is found in the chiral limit and therefore, the extrapolation to the chiral limit is questionable for these parameters. For these curves the critical temperature increases with increasing pion mass. This is an opposite behavior to the curves with $m^2 < 0$. The critical chemical potential shows a similar behavior as the other curves for higher sigma masses.

The only parameter in the quark sector of the grand potential is the Yukawa coupling g. Its value was determined by requiring a light constituent quark mass of $m_l = 300\,\mathrm{MeV}$. In Fig. 3.13(a) we show the influence of a variation of the Yukawa coupling on the phase diagram for $m_\sigma = 800\,\mathrm{MeV}$ in the presence of the $U(1)_A$ anomaly. We vary the Yukawa coupling in the range $g = 0.97g^* \ldots 1.15g^*$. g^* denotes the value for $m_l = 300\,\mathrm{MeV}$.

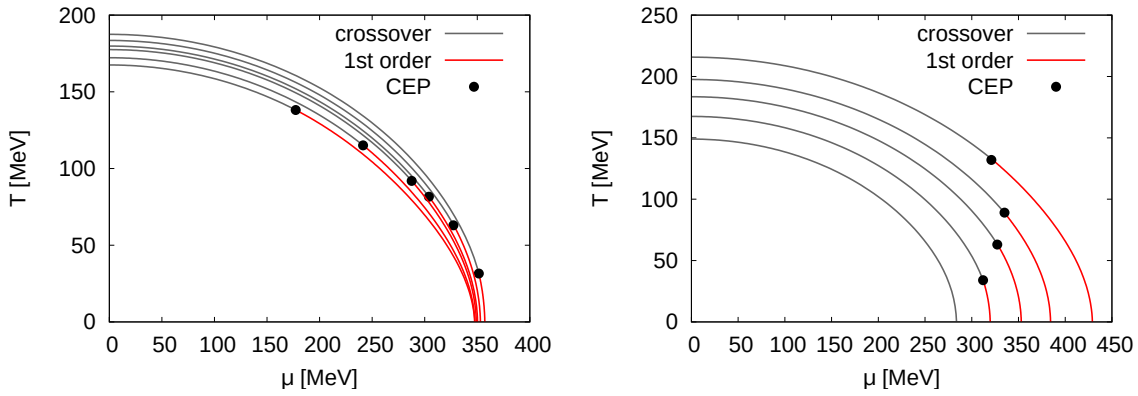

(a) Yukawa coupling

(b) $U(1)_A$ anomaly strength

Figure 3.13.: Left: Phase diagrams with $U(1)_A$ anomaly ($m_\sigma = 800$ MeV) for different values of the Yukawa coupling g. The lines correspond to $g = 1.15g^*$ (upper line), $1.10g^*, 1.05g^*, 1.03g^*, 1.0g^*$ and $0.97g^*$ (lower line). g^* denotes the value for $m_l = 300\,\mathrm{MeV}$. Right: Similar to the left figure but for various values of the $U(1)_A$ anomaly strength c. The lines correspond to $c = 0.6c^*$ (lower line), $0.8c^*$,$1.0c^*$, $1.2c^*$ and $c = 1.5c^*$ (upper line). c^* denotes the value at the physical point

The constituent quark masses depend linearly on the Yukawa coupling (cf. Eq. 3.13) so the relative change in the Yukawa coupling translates to the same relative change in the constituent quark masses. The pseudocritical temperatures slightly decreases for a reduced Yukawa coupling. The overall change of the pseudocritical temperature is within a range of $\sim 20\,\mathrm{MeV}$. This is an effect of roughly 10% for a variation of the Yukawa coupling within 20%. The effect in the μ direction is much weaker. The phase boundaries hit the μ-axis within in a range of $\sim 10\,\mathrm{MeV}$, corresponding to a relative change within 3%. The critical end point moves towards higher chemical potential and lower temperatures for a decreased Yukawa coupling. For $g \lesssim 0.95g^*$, the critical end point vanishes and the transition is always a crossover. For $g > 1.2g^*$ the critical end point vanishes as well, resulting in a first-order transition for the whole phase diagram.

The influence of the anomaly on the CEP has been discussed in several works, e.g. [59]. With a μ-dependent anomaly as suggested in [60] it is possible to create a scenario in PNJL models in which the surface bends towards lower bare quark masses, corresponding to the non-standard scenario suggested by de Forcrand and Philipsen [61].

For the phase diagrams shown in Fig. 3.13(b) we have modified the strength of the anomaly in the range $c = 0.6c^* \ldots 1.5c^*$. c^* denotes the value from the fit at the physical point. All other parameters are kept fixed at their values obtained for $m_\sigma = 800\,\mathrm{MeV}$. The modification of the anomaly changes all meson masses and the vacuum values are no longer the ones at the physical point. Setting $c = 0$ in this setup is therefore different

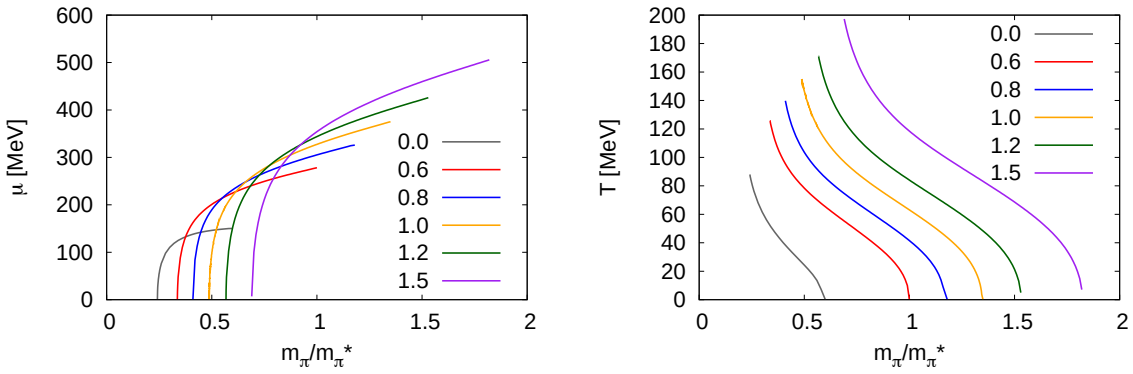

(a) μ_c (b) T_c

Figure 3.14.: The critical chemical potential (left panel) and critical temperature (right panel) as function similar to Figs. 3.11 (left panel) and 3.12 (right panel) for $m_\sigma = 800\,\mathrm{MeV}$. The lines correspond to different values of the anomaly strength $c = (0.6, 0.8, 1.0, 1.2, 1.5)c^*$. c^* denotes the value of the anomaly strength at the physical point.

from the previously discussed case, where the meson masses have been fitted to their physical values for $c = 0$. The situation is comparable to Fig. 3.9(b). For $c = 0.6c^*$ the critical end point vanishes and the transition is always a crossover. For increasing anomaly strength the CEP moves towards higher temperatures but does not vanish in the considered range.

As a first step towards the investigation of the influence on the critical surface it is instrumental to consider the critical lines, the cuts of the critical surface as discussed in Fig. 3.11, for different values of the anomaly strength c. In Fig. 3.14 we show the critical chemical potential and temperature choosing the path from the chiral limit to the physical again. For decreasing anomaly strength, the critical line starts at lower pion masses and the bending towards higher masses starts at a lower chemical potential. For $c = 0.6c^*$ the critical line ends before reaching the physical pion mass. This is again supplemented by Fig. 3.14(b), where the critical temperature reaches the m_π axis just before m_π^*. In order to construct a non-standard scenario from these considerations the anomaly strength must drop significantly before reaching a chemical potential $\mu \sim 150\,\mathrm{MeV}$. Using a μ-dependent anomaly strength that drops from $c = c^*$ at vanishing chemical potential to a value as discussed above it might be possible to construct a critical line that bends to the left. For $\mu = 0$ this critical line would start on the $c = c^*$ line and bend to the left towards the lines for reduced anomaly strength at finite μ. This view is however oversimplified since each point in the critical line represents a phase diagram calculated at a different anomaly strength, but within each phase diagram the anomaly strength was fixed and not μ-dependent.

Ignoring this consideration and using an μ-dependent anomaly strength as suggested in [60]

$$c(\mu) = c_0 \exp\left(-\left(\frac{\mu}{\mu_0}\right)^2\right) \tag{3.25}$$

the discussion above suggests a value of $\mu_0 \sim 210\,\mathrm{MeV}$. For very low values of $\mu_0 \sim 100\,\mathrm{MeV}$ we found indeed a critical line that slightly bends towards lower masses for $\mu \lesssim 100\,\mathrm{MeV}$. However, the strong bend to higher masses seen also for $c = 0c^*$ at chemical potentials $\mu \gtrsim 150\,\mathrm{MeV}$ was also found in the scenario with μ-dependent anomaly. Furthermore, if a μ-dependence of the anomaly is considered one should also take into account a temperature dependence [62], which will probably lead to further changes. A detailed study, including also a more physical motivation for the value of μ_0, should be carried out. We further note that the inclusion of vector-channel interactions also affects the location of the critical end point and may allow for the non-standard scenario [63, 22].

4. Deconfinement

Chiral effective models cannot describe the effects of gluonic degrees of freedom in QCD. The accompanying lack of confinement in these models results in a non-zero quark number density already in the confined phase. One approach to incorporate these effects explicitly is the coupling of these effective models to the Polyakov loop. Polyakov-NJL (PNJL) models with two (e.g., [64, 65, 66, 67, 68, 69, 70, 71]) and three (e.g., [60, 72, 73, 74]) flavors and also the Polyakov–quark-meson (PQM) model with two flavors ([75]) have been widely studied recently. In this chapter we will introduce the Polyakov loop and setup the PQM model with three quark flavors. Therein we will discuss the restoration of chiral symmetry and the deconfinement transition.

The definition of confinement is a delicate issue (for a review see e.g., [76]). The confining mechanism is not yet understood and there is a lot of ongoing work in this direction. For this work we will apply a rather pragmatic approach and use the Polyakov loop as an extension of the chiral models that allows for an effective incorporation of confinement in the chiral effective models. These type of model calculations cannot provide any insight on confinement, but they do provide a successful description of the equation of state when compared to lattice data at $\mu = 0$. Further these models allow for studies at finite chemical potential where lattice calculations fail.

4.1. Motivation

At vanishing temperature quark confinement can be defined using the Wilson-Wegner loop

$$W = \mathrm{Tr}\,\mathcal{P}\exp\left(i\oint dx^{\mu}A_{\mu})\right) \ , \tag{4.1}$$

where $\mathcal{P}$ denotes the path ordering and A_μ is the vector potential describing the gluon degrees of freedom (cf. Eq. 2.2). For confining theories the action of a Wilson-Wegner loop is proportional to its area. In non-confining theories it is proportional to its perimeter [77].

In this work we will use the Polyakov loop to take into account confinement. The Polyakov loop operator is a Wilson-Wegner loop in temporal direction

$$P(\vec{x}) = \mathcal{P}\exp\left(i\int_0^{\beta} d\tau A_0(\vec{x},\tau)\right) \tag{4.2}$$

where $A_0(\vec{x},\tau)$ is the temporal component of the Euclidean gauge field A_μ. τ denotes the Euclidean time component and $\beta = 1/T$ the inverse temperature. The Polyakov

loop winds around the Euclidean time component, since A_μ is periodic in the Euclidean time direction, $A_\mu(\vec{x},0) = A_\mu(\vec{x},\beta)$.

The creation operator of a static quark at spatial position $\vec{x}$ is obtained from the Polyakov loop by taking the trace over color space. The normalized Polyakov loop variables

$$\Phi\left(\vec{x}\right) = \frac{1}{N_c}\langle \mathrm{tr}_C\, P\left(\vec{x}\right)\rangle_\beta \ , \quad \bar{\Phi}\left(\vec{x}\right) = \frac{1}{N_c}\langle \mathrm{tr}_C\, P^\dagger\left(\vec{x}\right)\rangle_\beta \ , \tag{4.3}$$

are related to the free energy of a static, infinitely heavy test quark (F_q) and of an antiquark ($F_{\bar{q}}$), respectively:

$$\langle\Phi\rangle = \exp\left(-\beta F_q\right) \ , \quad \left\langle\bar{\Phi}\right\rangle = \exp\left(-\beta F_{\bar{q}}\right) \ . \tag{4.4}$$

The order parameter Φ vanishes in the confined phase as the free energy of a single static quark diverges. In the deconfined phase F_q takes a finite value and so does Φ.

The correlation function of two Polyakov loops with distance $\vec{r} = \vec{x} - \vec{y}$

$$\frac{1}{N_c^2}\langle \mathrm{tr}_C\, P\left(\vec{x}\right)\ P^\dagger\left(\vec{x}\right)\rangle_\beta = e^{-\beta F_{q\bar{q}}(\vec{r})} \tag{4.5}$$

can be related to the string tension σ in the Cornell potential

$$V(r) = \sigma r - \frac{\alpha(0)}{r} + \text{const.} \ . \tag{4.6}$$

At zero temperature the free energy is identical to the Cornell potential, describing the force between two heavy quarks, thus the string tension can be extracted.

The relation to the $Z(N_c)$[1] symmetry can be seen when applying gauge transformations. The gluons are described by the bosonic vector potential A_μ which obeys periodic boundary conditions

$$A_\mu(\vec{x},0) = A_\mu(\vec{x},\beta) \ . \tag{4.7}$$

Gauge transformations U that satisfy these boundary conditions themselves

$$U(\vec{x},0) = U(\vec{x},\beta) \ , \tag{4.8}$$

obviously retain the boundary conditions for the gauge fields A_μ.

One can also apply gauge transformations which are periodic up to a global twist matrix $z \in SU(N_c)$

$$U(\vec{x},0) = zU(\vec{x},\beta) \ . \tag{4.9}$$

When applying these type of gauge transformations to the gluon fields

$$\begin{aligned} A_\mu(\vec{x},\beta) \to A'_\mu(\vec{x},\beta) &= U(\vec{x},\beta)\left(A_\mu(\vec{x},\beta) + \partial_\mu\right) U^\dagger(\vec{x},\beta) \\ &= zU(x,0)\left(A_\mu(\vec{x},\beta) + \partial_\mu\right) U(x,0)z^\dagger \\ &= zA'_\mu(\vec{x},0)z^\dagger \ . \end{aligned} \tag{4.10}$$

[1] $Z(N_c)$: cylic group with N_c elements.

The boundary conditions for A_μ can only be fulfilled when z commutes with A_μ. This requires that z is an element of the center $Z(N_c)$ of $SU(N_c)$,

$$z = e^{i\phi} \ , \quad \phi = \frac{2\pi k}{N_c} \quad \text{with } k = 0, 1, \ldots, N_c - 1 \ . \tag{4.11}$$

The gauge action is symmetric under the discussed gauge transformations, but the Polyakov loop transforms as

$$\Phi \to z\Phi \ . \tag{4.12}$$

Thus, the center symmetry is only preserved if $\Phi = 0$, while it is spontaneously broken for $\Phi > 0$. The Polyakov loop variable Φ is an order parameter for the $Z(N_c)$ center symmetry.

The situation changes when dynamical quarks are introduced. The boundary conditions for fermions are anti-periodic, $\Psi(\vec{x}, 0) \to -\Psi(\vec{x}, \beta)$. When applying a gauge transformation U the fermions transform as

$$\Psi(\vec{x}, 0) \to \Psi'(\vec{x}, 0) = U(\vec{x}, 0)\Psi(\vec{x}, 0) \tag{4.13}$$

$$\Psi(\vec{x}, \beta) \to \Psi'(\vec{x}, \beta) = zU(\vec{x}, 0)\Psi(\vec{x}, \beta) = -zU(\vec{x}, 0)\Psi(\vec{x}, 0) \neq \Psi'(\vec{x}, 0) \tag{4.14}$$

and the boundary conditions are only fulfilled for $z = 1$, i.e., $\Phi = 0$. The center symmetry is explicitly broken and consequently Φ is no longer an exact order parameter. In the presence of dynamical quarks the free energy of a static quark does not diverge anymore and Φ is always nonvanishing.

Despite the explicit symmetry breaking with dynamical quarks it is possible to use the Polyakov loop as a tool to incorporate confinement effects in chiral models. The expectation values of Φ and $\bar{\Phi}$ are given by the minima of an effective Polyakov loop potential $\mathcal{U}$ and serve as approximate order parameters. The final form of the effective potential $\mathcal{U}$ is constructed in terms of the Polyakov loop variables Φ and $\bar{\Phi}$ and preserves the center symmetry of the pure Yang-Mills theory [78, 79]. The choice of the Polyakov loop potential is a delicate issue since the precise form of the effective potential is not known directly from lattice QCD simulations.

4.2. Polyakov loop potentials in pure gauge

In this section we discuss the choice of the Polyakov loop potential in pure gauge, i.e., without the presence of dynamical quarks. The functional form of the potential is motivated by the symmetries of QCD in the pure gauge limit. In the last years, several potentials have been proposed [64, 68, 60]. All of them reproduce a first-order transition at $T \sim 270\,\mathrm{MeV}$ in the pure gauge limit with $N_c = 3$ colors.

The simplest choice for a potential is based on a Ginzburg-Landau ansatz. Since the $Z(3)$ symmetry is only broken spontaneously it should be respected by the potential.

This results in a polynomial form

$$\frac{\mathcal{U}_{\text{poly}}}{T^4} = -b_2\left(|\Phi|^2 + |\bar{\Phi}|^2\right) - b_3(\Phi^3 + \bar{\Phi}^3) + b_4\left(|\Phi|^2 + |\bar{\Phi}|^2\right)^2 \tag{4.15}$$

with a temperature-dependent coefficient

$$b_2(T) = a_0 + a_1\left(\frac{T_0}{T}\right) + a_2\left(\frac{T_0}{T}\right)^2 + a_3\left(\frac{T_0}{T}\right)^3 . \tag{4.16}$$

The term $(\Phi^3 + \bar{\Phi}^3)$ breaks down the $U(1)$ symmetry present in the other terms of this ansatz to $Z(3)$. The parameters have been obtained by fitting the potential to reproduce the equation of state and the Polyakov loop data obtained in pure gauge lattice calculations. We use the numerical values given in [64]:

$$a_0 = 6.75\,, \quad a_1 = -1.95\,, \quad a_2 = 2.625\,, \quad a_3 = -7.44\,, \quad b_3 = 0.75\,, \quad b_4 = 7.5\,. \tag{4.17}$$

The parameter $T_0 = 270\,\text{MeV}$ defines the transition temperature in pure gauge.

An improved ansatz for the Polyakov loop potential guided by [80] is

$$\frac{\mathcal{U}_{\text{log}}}{T^4} = -\frac{1}{2}a(T)\bar{\Phi}\Phi + b(T)\ln\left[1 - 6\bar{\Phi}\Phi + 4\left(\Phi^3 + \bar{\Phi}^3\right) - 3\left(\bar{\Phi}\Phi\right)^2\right] , \tag{4.18}$$

with the temperature dependent coefficients

$$a(T) = a_0 + a_1\left(\frac{T_0}{T}\right) + a_2\left(\frac{T_0}{T}\right)^2 \tag{4.19}$$

and

$$b(T) = b_3\left(\frac{T_0}{T}\right)^3 . \tag{4.20}$$

The first term in this ansatz results from the kinetic part. The logarithm is due to the Haar measure of SU(3) group integration required when integrating out the excess degrees of freedom. The potential was also fitted to reproduce pure gauge lattice data. We adopt the parameters given in [68]:

$$a_0 = 3.51\,, \quad a_1 = -2.47\,, \quad a_2 = 15.2\,, \quad b_3 = -1.75\,. \tag{4.21}$$

A third form with only two parameters has been proposed in [60] by Fukushima. The potential is inspired from strong-coupling analyses,

$$\mathcal{U}_{\text{Fuku}} = -bT\left[54e^{-a/T}\Phi\bar{\Phi} + \ln\left(1 - 6\Phi\bar{\Phi} - 3(\Phi\bar{\Phi})^2 + 4(\Phi^3 + \bar{\Phi}^3)\right)\right] \tag{4.22}$$

with only two parameters a and b. The first term is a reminiscent of the nearest neighbor interaction and the logarithmic term is due to the Haar measure as in (4.18). The parameter a controls the deconfinement transition, i.e., also the transition temperature

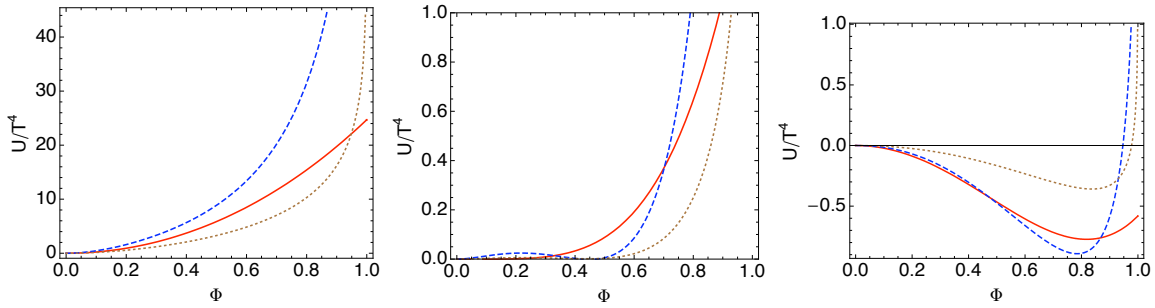

(a) $T = 0.5T_0$ (b) $T = 1.0T_0$ (c) $T = 1.5T_0$

Figure 4.1.: The polynomial (red solid line), logarithmic (blue dashed line) and Fukushima (brown dotted line) Polyakov loop potential $\mathcal{U}/T^4$ as function of the Polyakov loop for temperatures below (left), at (middle) and above (right) the phase transition.

in pure gauge, while b controls the mixing of the chiral and the deconfinement transition. This potential has been fixed to reproduce a transition temperature $T_0 \sim 270\,\mathrm{MeV}$ in pure gauge and a coincidence of the chiral and deconfinement transitions at $T \sim 200\,\mathrm{MeV}$ in a PNJL calculation. The adopted parameters are:

$$a = 664\,\mathrm{MeV}\ , \quad b = (196.2\,\mathrm{MeV})^3\ . \tag{4.23}$$

Note that this potential was not fitted to pure gauge lattice data as the other two potentials discussed before. A further significant difference is its contribution to the pressure at high temperatures. At very high temperatures both the unconfined transverse gluons as well as the Polyakov loop corresponding to the longitudinal gluons should contribute to the pressure. The Polyakov loop potentials fitted to pure gauge lattice data reproduce the pressure of the longitudinal and the transverse gluons just with the Polyakov loop, hence they contain the effect of the transverse gluons and might therefore overcount the degrees of freedom. The ansatz by Fukushima does not include the contribution of the transverse gluons. This difference will become important when comparing thermodynamic quantities calculated with different Polyakov loop potentials and lattice data. At temperatures $T \lesssim 1.5T_0$ the contribution to the Polyakov loop pressure is comparable for all three potentials [60]. The logarithmic divergence in the second and third potential limits the Polyakov loop to values $\Phi < 1$. This is different from the polynomial ansatz. In Fig. 4.1 we compare the potentials for temperatures below, at, and above the transition temperature T_0.

In Fig. 4.2(a) we show the temperature behavior of the Polyakov loop expectation values for all three ansätze. Note that although the polynomial and logarithmic potentials are fitted to reproduce the same pure gauge lattice data, the logarithmic form yields a much stronger first-order transition. At $T \sim 2T_0$ all three potentials approach the same value, while near T_0 the Fukushima ansatz has the steepest rise. The poly-

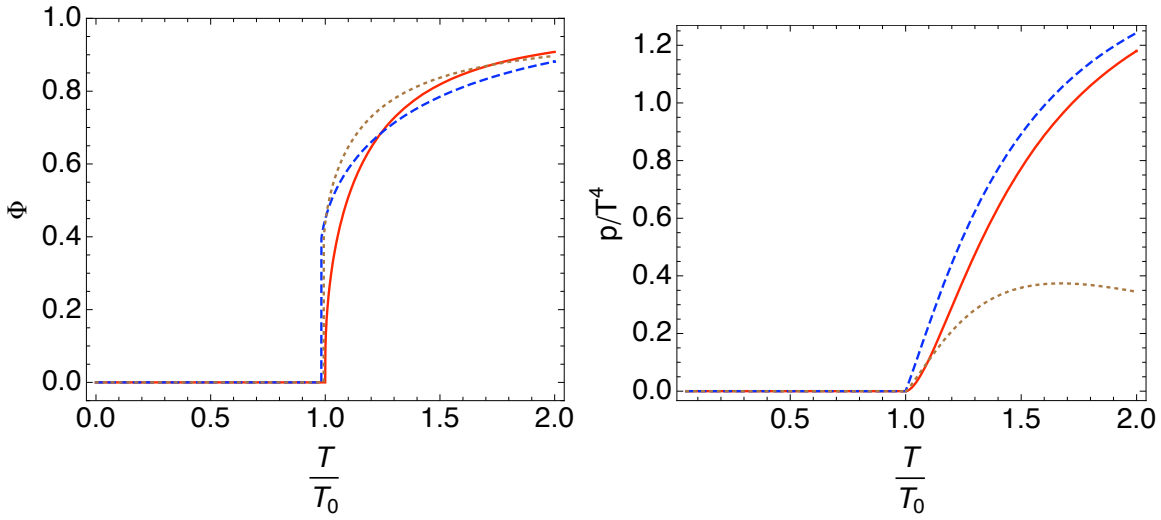

(a) Polyakov loop Φ

(b) Polyakov loop pressure

Figure 4.2.: Left: Polyakov loop expectation value Φ for the polynomial (red solid line), the logarithmic (blue dashed line) and the Fukushima (brown dotted line) Polyakov loop potential as a function of temperature. Right: The pressure in the pure gauge sector as a function of temperature for the three different Polyakov loop potentials.

nomial ansatz exhibits a weaker first-order transition but rises to higher values than the logarithmic ansatz. In Fig. 4.2(b) the pressure associated to the three potentials is shown in the pure gauge sector. While the Polyakov loop expectation values show a similar behavior for all potentials, the pressures behave quite differently. The polynomial and the logarithmic potential show a very similar behavior because they are fitted to the same pure gauge lattice data. The curve for the polynomial potential seems to be slightly shifted towards higher temperatures. The form suggested by Fukushima also shows a similar rise up to $T \sim 1.1T_0 \sim 300\,\mathrm{MeV}$, but then approaches a maximum at $T \sim 1.5T_0$. The logarithmic and the polynomial potential reach the Stefan-Boltzmann limit $\frac{p_{SB}}{T^4} = 2(N_c^2-1)\frac{\pi^2}{90} = 16\frac{\pi^2}{90} \sim 1.75$ at very high temperatures while the Fukushima potential reaches a maximum value of roughly $0.2p_{SB}$ and drops again for higher temperature. Here the different approach concerning the transverse gluons is most prominent.

4.3. Coupling to quarks

In order to address the connection between the chiral symmetry restoration and deconfinement, we employ the Polyakov-Quark-Meson (PQM) model which is a combination of a chiral linear σ-model with quarks, augmented with Polyakov loop degrees of freedom. For two quark flavors this model has been recently introduced in [75]. In this work

we consider the PQM model for three light quark flavors. The PQM Lagrangian $\mathcal{L}_{\mathrm{PQM}}$ consists of a quark-meson part $\mathcal{L}_{qm}$ where a uniform temporal background gauge field $A_\mu = \delta_{\mu 0} A^0$ is added to the quarks, and of a Polyakov loop potential $\mathcal{U}(\Phi[A], \bar{\Phi}[A])$:

$$\mathcal{L}_{\mathrm{PQM}} = \mathcal{L}_{qm} + \bar{q}\gamma_0 A_0 q - \mathcal{U}(\Phi[A], \bar{\Phi}[A]) \ . \tag{4.24}$$

The underlying quark-meson Lagrangian

$$\mathcal{L}_{qm} = \mathcal{L}_q + \mathcal{L}_m \tag{4.25}$$

is identical to the one in Eqs. 3.2 and 3.3. Its parameters have been discussed in Chap. 3.

The grand potential is obtained using a similar mean-field approximation as in Chap. 3. It is given by the sum of the contributions of the mesons, fermions and Polyakov loop.

The mesonic potential is not modified by the presence of the Polyakov loop and is therefore identical to (3.14). The Polyakov loop potential is affected by the presence of light quarks, but the functional form will not be modified in this work. A modification of the parameter T_0 depending on the numbers of quark-flavors N_f and chemical potential μ has been proposed in [75] and will be discussed later in this section.

Without the Polyakov loop, the trace over the color space during the derivation of the fermionic potential results merely in a factor N_c since the expressions are proportional to the unit matrix in color space.

The derivation of the fermionic grand potential with the Polyakov loop P leads to

$$\Omega_{\bar{q}q}(T,\mu) = -2T \sum_{f=u,d,s} \int \frac{d^3p}{(2\pi)^3} \,\mathrm{tr}_c \left\{ \ln\left[1 + P \exp\left(-\frac{E_{q,f} - \mu_f}{T}\right)\right] + \ln\left[1 + P^\dagger \exp\left(-\frac{E_{q,f} + \mu_f}{T}\right)\right]\right\} \tag{4.26}$$

with the trace over color still to be evaluated. Using the identity $\mathrm{tr}\ln A = \ln\det A$ the fermionic part of the grand potential is explicitly given as

$$\Omega_{\bar{q}q}(T,\mu) = -2T \sum_{f=u,d,s} \int \frac{d^3p}{(2\pi)^3} \left\{ \ln\left[1 + 3(\Phi + \bar{\Phi} b_f^{(+)}) b_f^+ + \left(b_f^{(+)}\right)^3\right] + \left[1 + 3(\bar{\Phi} + \Phi b_f^{(-)}) b_f^{(-)} + \left(b_f^{(-)}\right)^3\right]\right\} \ , \tag{4.27}$$

where we use the notation

$$b_f^{(\pm)} = b_f^{(\pm)}(T, \mu_f) = \exp\left(-\frac{E_{q,f} \mp \mu_f}{T}\right) \ . \tag{4.28}$$

The grand potential of the PQM model is finally given as

$$\Omega(T,\mu) = U(\sigma_x, \sigma_y) + \Omega_{\bar{q}q}(T,\mu) + \mathcal{U}(\bar{\Phi}, \Phi) \ . \tag{4.29}$$

This notation hides the implicit dependencies: $\Omega_{\bar{q}q}$ depends on the values of $\bar{\sigma}_x$ and $\bar{\sigma}_y$ via the constituent quark masses, and also on the Polyakov loop expectation values $\left\langle\bar{\Phi}\right\rangle$ and $\langle\Phi\rangle$. The four equations of motion

$$\frac{\partial\Omega}{\partial\sigma_x}=\frac{\partial\Omega}{\partial\sigma_y}=\frac{\partial\Omega}{\partial\Phi}=\frac{\partial\Omega}{\partial\bar{\Phi}}\bigg|_{\sigma_x=\bar{\sigma}_x,\sigma_y=\bar{\sigma}_y,\Phi=\langle\Phi\rangle,\bar{\Phi}=\left\langle\bar{\Phi}\right\rangle}=0\ . \tag{4.30}$$

have to be solved simultaneously in order to minimize the thermodynamic potential. They define the T and μ dependence of the thermal expectation values $\bar{\sigma}_x,\bar{\sigma}_y,\langle\Phi\rangle$ and $\left\langle\bar{\Phi}\right\rangle$. In the following we will use Φ, and $\bar{\Phi}$ also for the thermal expectation values whenever the meaning is unambiguous.

Before solving these equations of motion numerically, we discuss the way confinement is mimicked in Polyakov-loop-enhanced chiral models. It is instructive to consider the limits of the Polyakov loop expectation values for confined and unconfined matter.

Dropping common prefactors, the transition from the fermionic potential for the quarks without the Polyakov loop to the one with is achieved via the replacement

$$-N_c\ln\left[\frac{1}{1+n_{q,f}(T,\mu)}\right]\to\ln\left[1+N_c(\Phi+\bar{\Phi}b_f^{(+)})b_f^{+}+\left(b_f^{(+)}\right)^{N_c}\right] \tag{4.31}$$

and likewise for the anti-quarks. In the deconfined phase with $\Phi=\bar{\Phi}=1$ we can transform the expression with the Polyakov loop,

$$\begin{aligned}\ln\left[1+N_c(\Phi+\bar{\Phi}b_f^{(+)})b_f^{+}+\left(b_f^{(+)}\right)^{N_c}\right]&\to\ln\left[1+N_c(1+b_f^{(+)})b_f^{+}+\left(b_f^{(+)}\right)^{N_c}\right]\\&=\ln\left[\left(1+b_f^{(+)}\right)^{N_c}\right]\\&=-N_c\ln\left[\frac{1}{1+n_{q,f}(T,\mu)}\right]\ ,\end{aligned} \tag{4.32}$$

returning to the expression without the Polyakov loop.

The effective confinement can be understood by applying $\Phi=\bar{\Phi}=0$ for the confined phase:

$$\begin{aligned}\ln\left[1+N_c(\Phi+\bar{\Phi}b_f^{(+)})b_f^{+}+\left(b_f^{(+)}\right)^{N_c}\right]&\to\ln\left[1+\left(b_f^{(+)}\right)^{N_c}\right]\\&=-\ln\left[\frac{1}{1+n_{N_cq,f}(T,\mu)}\right]\ .\end{aligned} \tag{4.33}$$

Instead of single quark states, a baryon-like object of $N_c=3$ quarks contribute to the thermodynamic potential now.

So far only the influence of the Polyakov loop potential on the fermionic sector has been considered. The Polyakov loop potential was adopted from pure gauge. In the presence

N_f	0	1	2	2+1	3
T_0[MeV]	270	240	208	187	178

Table 4.1.: The N_f-dependent critical temperature $T_0(N_f)$ for N_f massless flavor according to [75]. The value for 2+1 flavors has been obtained for a massive strange quark with $m_s = 150\,\mathrm{MeV}$.

of dynamical quarks, the running coupling is changed due to fermionic contributions. This has been investigated in detail in [75] using the polynomial potential. At zero temperature, Λ_{QCD}, becomes dependent on the number of dynamical quark flavors N_f, which can be translated to a N_f-dependence of T_0. The results are summarized in Tab. 4.1. We will investigate the influence of different values of T_0 for the logarithmic and polynomial potential on the phase structure.

The authors of [75] further suggested an μ-dependence of the Polyakov loop potential

$$T_0(\mu) = T_\tau \exp\left(-1/\left(\alpha_0 b(\mu)\right)\right) \ , \quad b(\mu) = \frac{27}{6\pi} - \frac{48}{\pi}\frac{\mu^2}{T_\tau^2} \tag{4.34}$$

with the parameters $\alpha_0 = 0.304$ and T_τ, whose value is flavor-dependent and chosen so that $T_0(\mu = 0)$ reproduces the values given in Tab. 4.1. This approach was motivated from the QCD β-function and hard dense loop (HDL)/hard thermal loop (HTL) loop results.

The modifications of T_0 are first approximations, but they show that the influence of the dynamical fermions on the Polyakov loop has to be carefully investigated and is not yet understood.

4.4. Results at vanishing chemical potential

Having set up the model, we will explore the phase structure at $\mu = 0$ in this section. We will use the same notation for the temperatures of the chiral transition as defined in Sect. 3.2, i.e., $T_\chi \equiv T_\chi^l$ and T_χ^s for the chiral transitions of the light and strange quarks, respectively. Additionally, we label the deconfinement transition temperature as T_d.

As already discussed, the coincidence of the chiral and deconfinement transitions is often assumed, but the situation is not quite clear. Lattice data led to the conjecture that there is some locking of both transitions at $\mu = 0$. Recent calculations reported different pseudocritical temperatures at $\mu = 0$, and also different scenarios concerning the coincidence of both transitions. The RBC-Bielefeld group reported the chiral and the deconfinement transition at the same critical temperature [28]. The Wuppertal group report a higher temperature for the peak in the Polyakov loop susceptibility than for the chiral susceptibility [29] (cf. also Sect. 2.2.1).

In our model calculations we have some freedom in the choice of parameters that affect the chiral transition, e.g., the mass of the σ-meson, and parameters that change

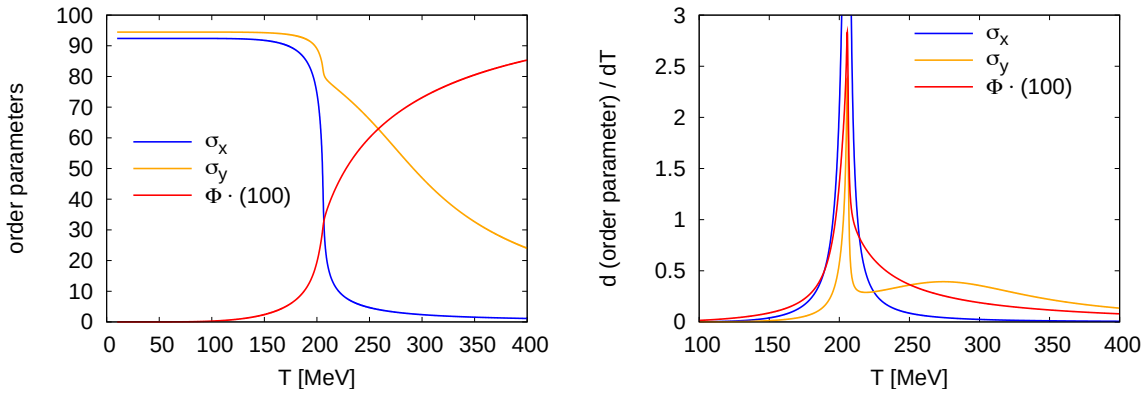

(a) Logarithmic potential $T_0 = 270\,\mathrm{MeV}$ (b) Logarithmic potential $T_0 = 270\,\mathrm{MeV}$

Figure 4.3.: The order parameters σ_x, σ_y and $\Phi = \bar{\Phi}$ as a function of temperature at vanishing chemical potential for $m_\sigma = 600\,\mathrm{MeV}$ with the logarithmic Polyakov loop potential ($T_0 = 270\,\mathrm{MeV}$). The left panel shows the values of the order parameters. The right panel shows the corresponding temperature derivatives. The values of the Polyakov loop expectation value have been scaled by a factor of 100. For the strange and non-strange condensate $-d\sigma_{x,y}/dT$ is shown.

the deconfinement transition like T_0. Since these transitions are coupled, we cannot tune the chiral and deconfinement transition temperatures completely independently.

In our mean-field approximation the thermodynamics is implemented in the fermionic degrees of freedom. As long as the Polyakov loop suppresses the fermionic contribution significantly, we cannot find a chiral transition in our model at all because the driving mechanism is strongly suppressed. Together with the requirement that QCD with dynamical massless quarks cannot be confining in the chirally restored phase [75], a coincidence scenario is preferred in our model calculations.

In Fig. 4.3(a), the order parameters for the phase transitions as a function of the temperature are shown at vanishing chemical potential. For the underlying quark-meson model we have chosen $m_\sigma = 600\,\mathrm{MeV}$ and taken into account the explicit breaking of the $U(1)_A$ symmetry. For the logarithmic Polyakov loop potential (4.18) $T_0 = 270\,\mathrm{MeV}$ was used. The strange and non-strange condensates stay constant up to temperatures of $T \sim 150\,\mathrm{MeV}$. The non-strange condensate shows a very rapid crossover at $T \sim 207\,\mathrm{MeV}$. The strange condensate shows a drop of roughly $10\,\mathrm{MeV}$ at the chiral transition of the light quarks and very smooth crossover beyond the transition. The Polyakov loop expectation value is vanishing up to temperatures of $T \sim 100\,\mathrm{MeV}$ and then slightly rises to $\Phi \sim 0.1$ just below the chiral phase transition of the light quarks. At the phase transition it reaches $\Phi \sim 0.45$ and then very slowly approaches 1. The detailed behavior of Φ is somewhat model-dependent and we will discuss the predictions of the different

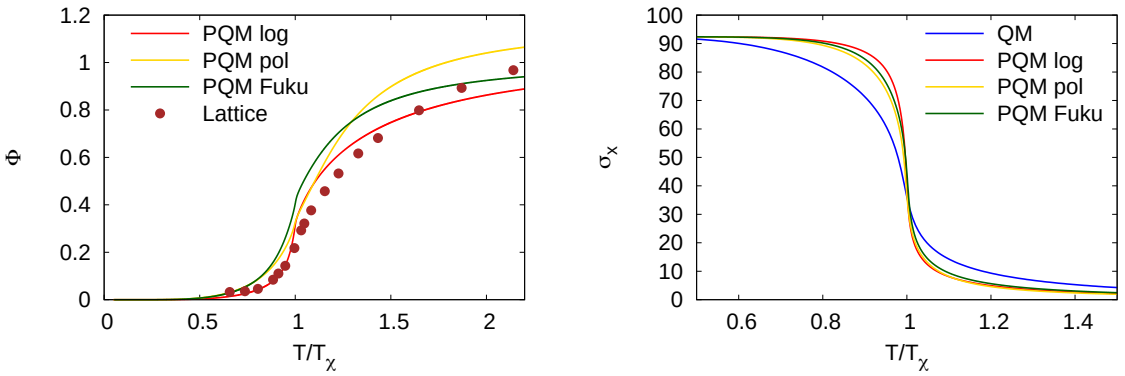

(a) Polyakov loop expectation value Φ

(b) non-strange condensate σ_x

Figure 4.4.: Left: Polyakov loop expectation value as a function of temperature for different Polyakov loop potential. For comparison also lattice data for $N_\tau = 6$ taken from [81] are shown. Right: The non-strange condensate as a function of temperature for different Polyakov loop potentials. Also shown is the result without Polyakov loop (QM).

Polyakov loop potentials later.

In Fig. 4.3(b), the corresponding temperature derivatives are shown. A strong peak in all order parameters is found at $T \sim 207\,\mathrm{MeV}$, indicating the rapid crossover. The very smooth crossover in the strange condensate shows up as a rather small bump at $T \sim 274\,\mathrm{MeV}$. No separate peak is found for the Polyakov loop, indicating a coincidence of the chiral and the deconfinement transitions.

In Fig. 4.4 the Polyakov loop and non-strange condensate are compared for different choices of the Polyakov loop potential. For $T_0 = 270\,\mathrm{MeV}$ we find coincidence of the chiral and the deconfinement transition for the logarithmic and the polynomial potential. For the Polyakov loop expectation value we also compare our results with $2+1$ flavor lattice data obtained with $N_\tau = 6$ [81]. While Φ vanishes for all potentials for $T < 0.5T_\chi$ the three different potentials result in different behaviors of the Polyakov loop above T_χ. For temperatures in the range $0.5T_\chi < T < T_\chi$ the Fukushima potential results in the fastest increase but overall it is similar to the result for the polynomial potential. The logarithmic potential agrees very nicely with the lattice data up to T_χ. Above T_χ the polynomial potential results in an overshooting of the lattice values and Φ is not limited to values below one. The Fukushima and the logarithmic potential rise faster than the values obtained in lattice calculations and start to flatten at $T \sim 1.5T_\chi$ leading to somewhat smaller values than the lattice data at $T \sim 2T_\chi$. For both potentials the shape is very similar: a very fast rise of the Polyakov loop near T_χ and a small kink at T_χ with a flattening at higher temperatures. The lattice data and the polynomial potential show a smoother crossover.

The influence of the different potentials on the non-strange condensate is shown in Fig. 4.4(b). For comparison, the condensate from a calculation without the Polyakov loop is displayed as well. Without the Polyakov loop the non-strange condensate already starts to melt at $T \sim 0.5T_\chi$ and still has not reached its final value at $T \sim 1.5T_\chi$. Note that the value of T_χ is significantly smaller without the Polyakov loop ($T_\chi \sim 150\,\mathrm{MeV}$) than with Polyakov loop ($T_\chi \sim 200\,\mathrm{MeV}$) and so the temperature range shown for the model without Polyakov loop is somewhat smaller and shifted towards lower temperatures. The Polyakov loop suppresses the fermionic degrees of freedom in the broken phase resulting in a higher temperature for the chiral transition. In the pure gauge limit the Polyakov loop is zero until $T_0 = 270\,\mathrm{MeV}$. The chiral transition is pulled to higher temperatures by the Polyakov loop.

With Polyakov loop the condensate stays constant up to $T \sim 0.8T_\chi$. For temperatures above T_χ the condensate is very similar for all different Polyakov loop potentials and the differences are negligible for $T > 1.2T_\chi$, although the values of the Polyakov loop Φ differ significantly. In the range $0.8T_\chi$ to T_χ the effect of the different potentials is most prominent. While the Fukushima and polynomial potential show a similar behavior, the melting sets in later for the logarithmic potential. At $T \sim T_\chi$ this effect is already compensated. At $T \sim m_l$ the condensates agree for the model with and without Polyakov loop as expected for the deconfined phase.

Since the different Polyakov loop potentials and different choices of m_σ allow for a wide range of possible scenarios we have summarized the pseudocritical temperatures for the different transitions in Tab. 4.2. For the logarithmic (4.18) and polynomial potential (4.15) the transition temperature was varied according to the different scenarios discussed in [75] and Sect. 4.3 to take into account the effect of dynamical quarks on the Polyakov loop. The last column indicates whether the deconfinement transition and the chiral transition for the light quarks coincide. As a general trend the chiral transition temperature is significantly increased by the Polyakov loop. For the logarithmic and the polynomial potential the chiral transition temperature for the same value of m_σ and T_0 are very similar. The deconfinement transition occurs at smaller temperatures with the logarithmic than with the polynomial potential. This also affects the coincidence of the chiral and the deconfinement transition, which is only found for two combinations of T_0 and m_σ for the logarithmic potential. The Fukushima potential yields the lowest transition temperatures and a coincidence of the chiral and deconfinement transition is found for $m_\sigma = 500, 600\,\mathrm{MeV}$.

The exact reason for the different behavior of the potentials is not quite obvious. Recalling the results for the different potentials in pure gauge, (cf. Sect. 4.2) some indications can be found. First, we consider the Polyakov loop expectation value in pure gauge: The logarithmic potential causes a stronger first order transition than the polynomial potential. In the PQM model, however, a crossover transition is observed hence the influence of the quark-meson model has to weaken the first-order transition. A remnant of this stronger first-order transition is also observed in PQM model, where the crossover occurs more rapidly for the logarithmic potential. The Fukushima potential

$\mathcal{U}$	T_0[MeV]	m_σ[MeV]	T_χ^l[MeV]	T_χ^s[MeV]	T_d[MeV]	$T_\chi^l \approx T_d$
-	–	800	184	278	–	
-	–	600	146	248	–	
-	–	500	129	238	–	
poly	270	800	228	306	227	$\star$
poly	208	800	204	297	178	
poly	187	800	197	295	161	
poly	178	800	194	273	154	
poly	270	600	204	262	204	$\star$
poly	208	600	179	270	179	$\star$
poly	187	600	171	267	171	$\star$
poly	178	600	166	236	166	$\star$
poly	270	500	193	254	220	
poly	208	500	168	239	168	$\star$
poly	187	500	159	237	159	$\star$
poly	178	500	156	236	156	$\star$
log	270	800	228	302	208	
log	208	800	208	293	166	
log	187	800	204	251	150	
log	270	600	207	274	207	$\star$
log	208	600	180	286	165	
log	187	600	172	283	150	
log	270	500	198	264	198	
log	208	500	168	255	168	$\star$
log	187	500	159	252	150	
Fuku	–	800	214	289	193	
Fuku	–	600	189	260	189	$\star$
Fuku	–	500	179	250	179	$\star$

Table 4.2.: Pseudocritical temperatures of the chiral transition for the light (T_χ^l) and strange (T_χ^s) condensate and the deconfinement transition (T_d) at $\mu = 0$ for different Polyakov loop potentials and different values of m_σ. In the last column we indicate whether the chiral and deconfinement transitions coincide ($\star$).

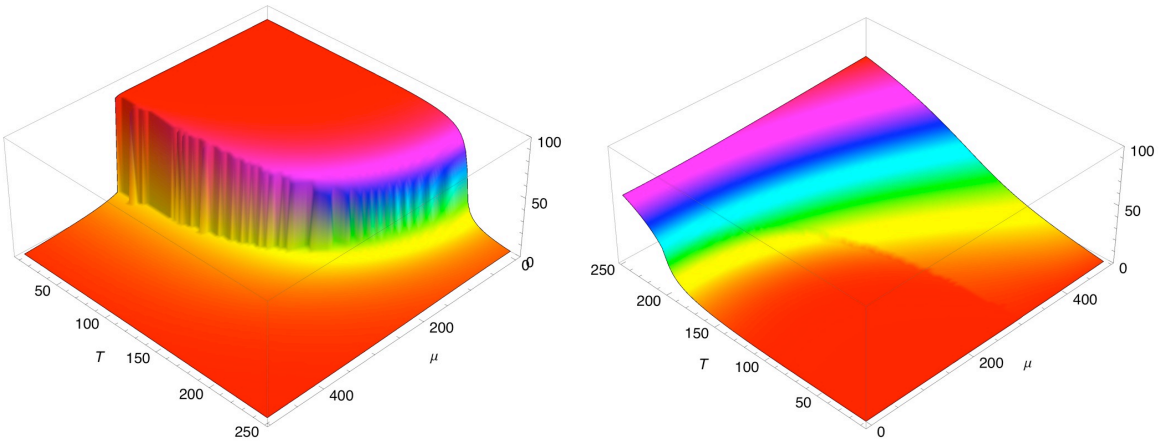

(a) σ_x (b) 100Φ

Figure 4.5.: Non-strange chiral condensate σ_x (left) and Polyakov loop expectation value Φ (right) as function of temperature and chemical potential. The Polyakov loop expectation value has been multiplied with 100. Note the different view points.

also produces a strong first-order transition in the pure gauge limit, but the depth of the potential is much lower than for the logarithmic potential, cf. Fig. 4.1. When coupled to the quarks the influence of the Polyakov loop is therefore weaker for the Fukushima potential than for the logarithmic potential. The strength of the polynomial potential is comparable to the logarithmic potential but it is missing the logarithmic divergence for $\Phi \to 1$ and is therefore somewhat smoother. In the PQM model calculations it shows the smoothest crossover behavior for the Polyakov loop expectation value. A smoother transition of the Polyakov loop seems to support a coincidence of the chiral and deconfinement transitions in Polyakov loop models. Compared to lattice calculations, where both transitions coincide, one also finds a very smooth crossover for the Polyakov loop.

4.5. Finite chemical potential

The situation at finite μ is more complicated, because there is no guidance from lattice data. The Polyakov loop potentials are motivated and fitted to pure gauge lattice data and do not contain any effects of dynamical quarks. Some modifications to account for finite μ proposed in [75] have been already discussed in Sect. 4.3.

In Fig. 4.5 we show the order parameters σ_x and Φ as a function of temperature and chemical potential μ for the logarithmic Polyakov loop potential. Since we focus on the coincidence of the chiral and deconfinement transitions we refrain from showing the strange condensate. It always undergoes a smooth crossover at temperatures larger than

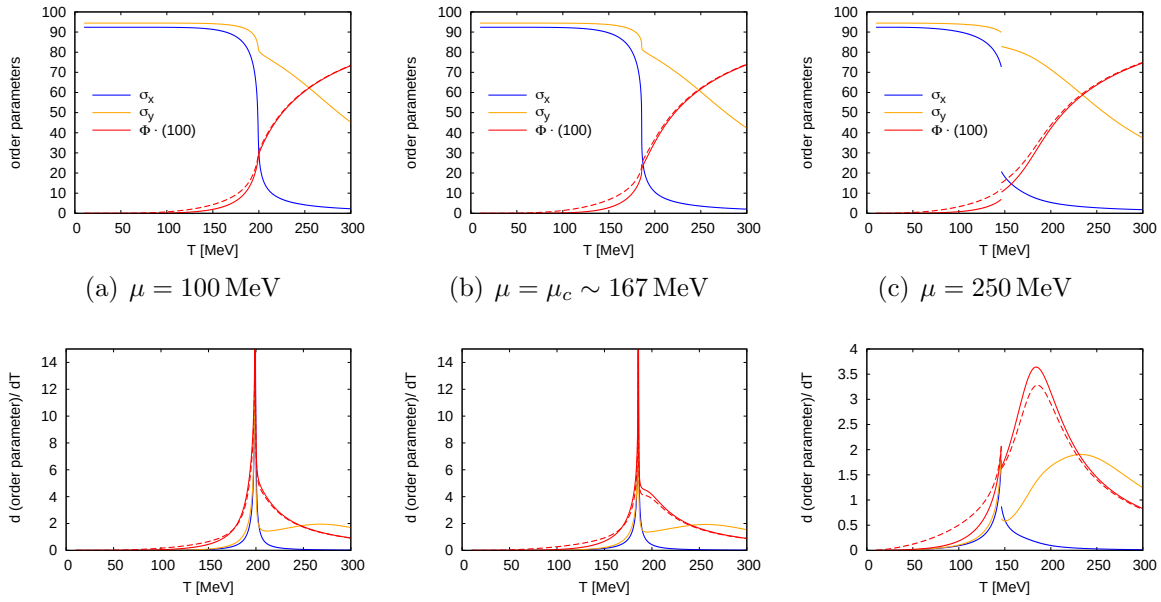

(a) $\mu = 100\,\mathrm{MeV}$ (b) $\mu = \mu_c \sim 167\,\mathrm{MeV}$ (c) $\mu = 250\,\mathrm{MeV}$

(d) $\mu = 100\,\mathrm{MeV}$ (e) $\mu = \mu_c \sim 167\,\mathrm{MeV}$ (f) $\mu = 250\,\mathrm{MeV}$

Figure 4.6.: The order parameters in the PQM model with logarithmic potential ($T_0 = 270\,\mathrm{MeV}$) as a function of temperature for different values of μ. The Polyakov loop expectation values Φ (solid line) and $\bar{\Phi}$ (dashed line) have been multiplied with a factor 100. The lower panels show the corresponding temperature derivatives similar to Fig. 4.3.

the transition temperature of the non-strange condensate, with only minor modifications due to the inclusion of the Polyakov loop. $\bar{\Phi}$ is not shown since its qualitative behavior is identical to Φ.

The chiral condensate shown in the left panel shows the expected crossover at vanishing chemical potential and a first-order transition is found at $\mu \sim 300\,\mathrm{MeV}$ and small temperatures. A critical end point is observed at $(T_c, \mu_c) \sim (185, 167)\,\mathrm{MeV}$. In the right panel the Polyakov loop Φ is shown. While the chiral phase transition describes a curve towards the μ-axis the Polyakov loop shows only a slight dependence on μ. At $\mu \sim 300\,\mathrm{MeV}$ and low temperatures a small structure occurs induced by the first-order transition in the chiral condensate. At zero temperature the Polyakov loop is vanishing in the broken phase and very small even in the chirally restored phase at small temperatures. This is a first hint that there might be a *quarkyonic* phase [82] in which chiral symmetry is restored and the quarks are still confined. The resulting phase diagrams as well as the influence of different Polyakov loop potentials will be discussed later.

In Fig. 4.6 we show the order parameters including $\bar{\Phi}$ and the strange condensate σ_y as functions of the temperature for $\mu = 100\,\mathrm{MeV}$, μ_c, $250\,\mathrm{MeV}$, as well as the corresponding temperature derivatives. The Polyakov loop expectation values have been scaled by a

factor of 100. For the chiral condensates we show $-d\sigma_{x,y}/dT$ so that the peak is positive for all order parameters. The derivatives for the strange condensate and for the Polyakov loop have been scaled with a factor of 5 for clarity. At finite chemical potential, Φ and $\bar{\Phi}$ are no longer related by hermitian conjugation and in general $\bar{\Phi} \neq \Phi$. An intuitive explanation is that a static antiquark can be screened more easily than a quark in a medium with more quarks. The resulting smaller free energy of an antiquark $F_{\bar{q}} < F_q$ corresponds to $\bar{\Phi} = \exp(-\beta F_{\bar{q}}) > \exp(-\beta F_q) = \Phi$.

At $\mu = 100\,\mathrm{MeV}$ no significant differences from the situation at vanishing chemical potential are observed. The chiral and deconfinement transitions coincide at $T \sim 200\,\mathrm{MeV}$. As expected, $\bar{\Phi} > \Phi$ is found, but the qualitative behavior is identical and the quantitative difference is rather small. The coincidence is also observed in the temperature derivative. The rapid phase transition in the non-strange chiral condensate always induces a peak in the strange condensate and the Polyakov loop expectation values. At the critical chemical potential $\mu = \mu_c \sim 167\,\mathrm{MeV}$, still only one peak for the chiral and the deconfinement transition is found. However the peak in the Polyakov loop expectation values shows now a more prominent shoulder at temperatures slightly above $T_c \sim 186\,\mathrm{MeV}$. This might be a first indication of two distinct phase transitions. Unlike the chiral condensate, the Polyakov loop does not show a very sharp peak indicating a second-order transition. The peak in the chiral condensate is very sharp and has been clipped to fit in the figure while the peak in the Polyakov loop expectation value is rather broad indicating a crossover transition. At the critical end point the Polyakov loop expectation values have reached a value of $\Phi \sim 0.3 < 0.5$.

At $\mu = 250\,\mathrm{MeV}$ a first-order transition is observed in the chiral condensate. This also induces a small jump in the Polyakov loop but the expectation value of Φ is still very small ($\Phi \lesssim 0.1$). The temperature derivative shows a broad peak at higher temperatures. In this region the chiral and deconfinement transitions clearly do not coincide. Note that for all considered chemical potentials including $\mu = 0$ we find $\Phi \sim 0.3$ at the peak in our model setup. This is surely not a general feature, as for $\mu = 0$ the value of Φ at the transition is slightly model dependent, cf. Fig 4.4(a). Anyhow, this feature might help in the determination of the phase transition since the numerical distinction of two overlapping peaks is somewhat involved.

In Figs. 4.7, 4.8 and 4.9 we show the temperature derivatives of the order parameters σ_x and Φ as a function of T and μ. Qualitatively, the chiral condensate depends only weakly on the chosen Polyakov loop potential. The detailed location of the CEP will move, as explained below when the resulting phase diagrams are discussed. The stronger peak in the crossover regime stems from the fact that for a first-order transition only a jump is found in the first derivative as already discusses above. Further the sampling used for the plot and the temperature derivative, which is for small T nearly parallel to the phase transition might not catch the full height of the peak.

For the temperature derivatives of the Polyakov loop expectation value Φ, shown in the right panels the situation is different. With the polynomial potential we find a splitting of the peaks already at small chemical potentials. The peak at low temperatures

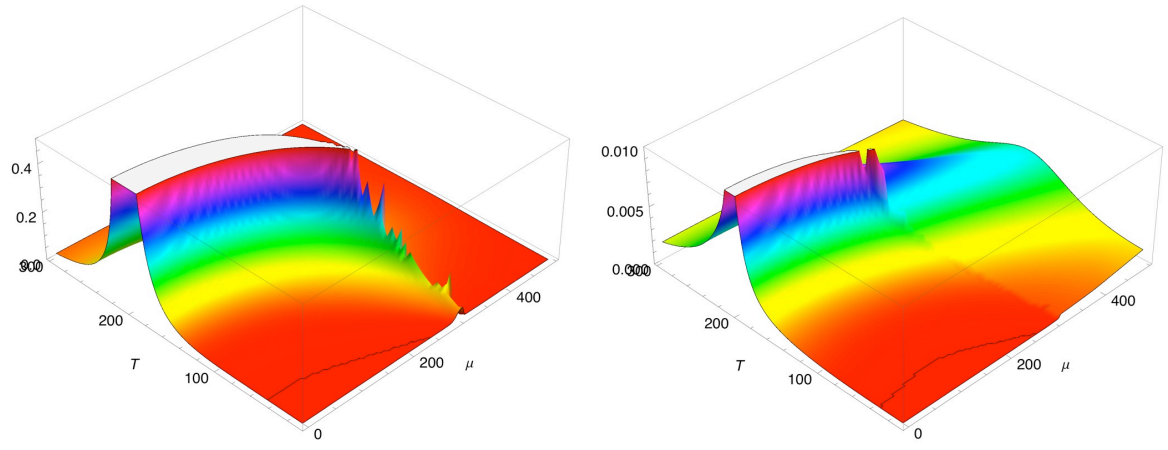

(a) $-d\sigma_x/dT$ (b) $d\Phi/dT$

Figure 4.7.: The temperature derivatives of the order parameters σ_x (left panel) and Φ (right panel) for the logarithmic Polyakov loop potential ($T_0 = 270\,\mathrm{MeV}$). Note, that in the left panel $-d\sigma_x/dT$ is displayed.

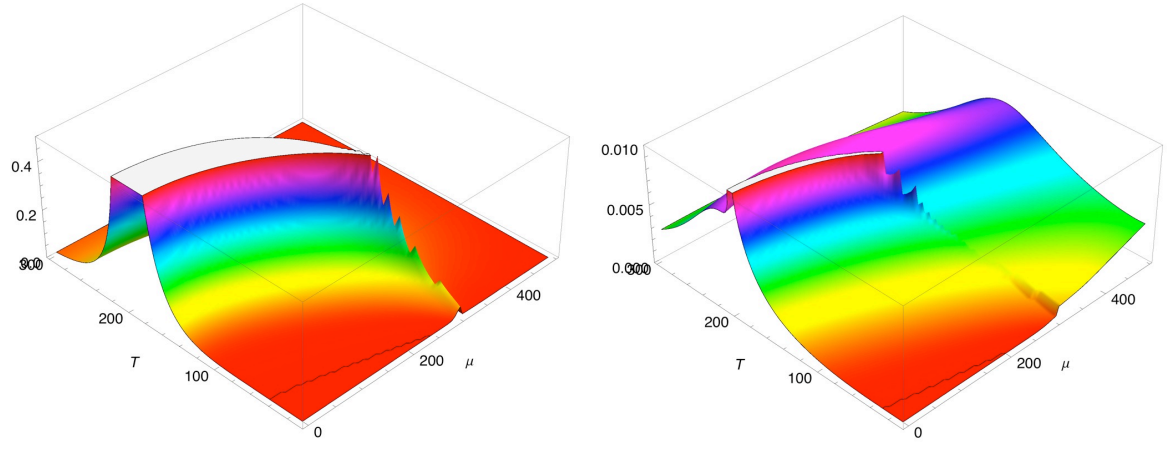

(a) $-d\sigma_x/dT$ (b) $d\Phi/dT$

Figure 4.8.: Similar to Fig. 4.7 but for the polynomial Polyakov loop potential ($T_0 = 270\,\mathrm{MeV}$).

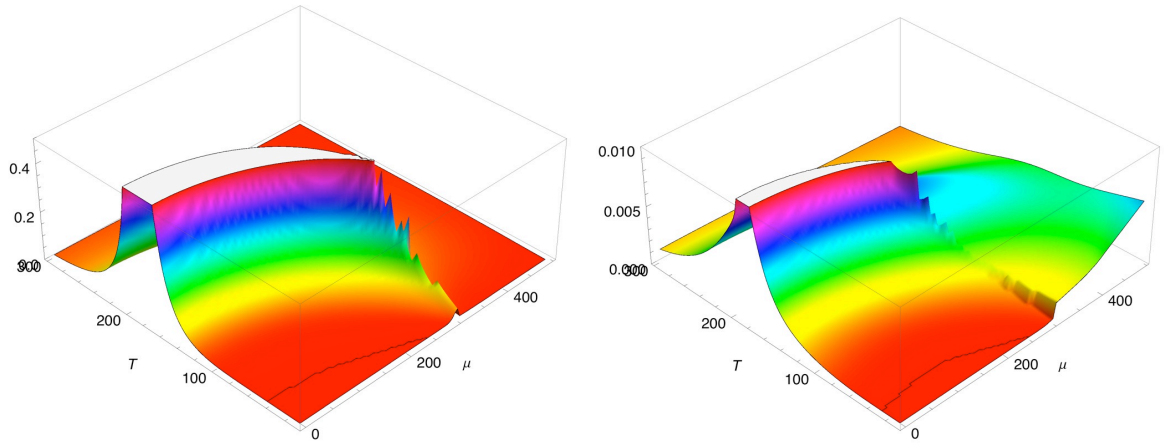

(a) $-d\sigma_x/dT$ (b) $d\Phi/dT$

Figure 4.9.: Similar to Fig. 4.7 but for the Fukushima Polyakov loop potential.

is induced by the strong chiral phase transition while the peak at higher temperatures results from the rise in Φ. Similar to the situation with the logarithmic potential almost no bending towards the μ-axis is observed. At small temperatures we find a small jump resulting from the first-order transition in the chiral condensate.

For the Fukushima potential both transitions split at higher chemical potentials and a bending towards the μ-axis is found. For this potential the influence of the chiral transition seems to be stronger also at finite chemical potential, but at small temperatures both transitions split, too.

4.6. Phase structure

Although a criterion for the deconfinement transition is not obvious at finite μ, we show the phase diagrams for different Polyakov loop potentials. The boundary of the deconfinement transition is determined from the peak in the temperature derivative of the Polyakov loop expectation value. Similarly we determine the chiral phase boundaries for the light quark condensate.

As already seen in the discussion of the order parameters, the chiral and the deconfinement transition are not locked and may spread at finite chemical potential. Since both transitions are smooth crossovers – at least at small chemical potential – the corresponding peaks are not sharp and a clear distinction may technically be difficult, in particular if both peaks are close together or even overlap. This may lead to a picture where both transitions seem to be at the same temperature but a jump apart once the peaks become distinguishable. For the interpretation of the results one should also keep in mind that the deconfinement transition in particular, is rather smooth hence the line is more to guide the eye. The chiral transition for the light quarks is rather sharp and

Potential	Log	Log	Pol	Pol	Fuku	without
$T_0[\,\mathrm{MeV}]$	270	$270, T_0(\mu)$	270	208	-	-
$(T_c, \mu_c)[\,\mathrm{MeV}]$	$(186, 167)$	$(172, 169)$	$(162, 207)$	$(140, 208)$	$(162, 175)$	$(92, 221)$

Table 4.3.: The location of the critical end points (T_c, μ_c) for different Polyakov loop potentials as shown in Fig. 4.10.

can be determined precisely, as well as the critical end point.

In Fig. 4.10, we show a selection of phase diagrams for different Polyakov loop models. All these models have been tuned to reproduce a coincidence (within a few MeV) of the chiral and deconfinement transitions at vanishing chemical potential. For comparison, we also show the phase diagram for the model without Polyakov loop as discussed in Chap. 3. The pseudocritical temperatures for the different models are summarized in Tab. 4.2. For the logarithmic potential we show results with a constant $T_0 = 270\,\mathrm{MeV}$ in Fig. 4.10(a) and with a μ-dependent $T_0(\mu)$ (cf. Eq. 4.34) in Fig. 4.10(b). At $\mu = 0$ a value of $T_0(\mu = 0) = 270\,\mathrm{MeV}$ is used, so that both phase diagrams are identical at vanishing chemical potential. For the polynomial potential we vary the value of T_0 and use the values $T_0 = 270\,\mathrm{MeV}$ and $T_0 = 208\,\mathrm{MeV}$ in Figs. 4.10(c) and 4.10(d), respectively. In addition, we show the results with the Fukushima potential in Fig. 4.10(e) and the model without Polyakov loop (Fig. 4.10(f)).

The generally higher chiral transition temperature T_χ^l and the more rapid crossover with Polyakov loop at vanishing chemical potential affect the location of the critical end point. The whole chiral phase boundary is pulled towards higher temperatures with the Polyakov loop and the first-order transition extends towards lower chemical potentials. With the logarithmic potential the critical end point is found at the lowest values of μ and the most rapid crossover at zero chemical potential is observed. It is noticeable that the critical end point is found at nearly the same chemical potential with a constant and a μ-dependent T_0, despite the lower phase boundary at intermediate chemical potential for the μ-dependent T_0. At very small temperatures the boundaries for the μ-dependent and constant T_0 coincide again. The decreased but constant value of T_0 in the polynomial potential causes a phase boundary at lower temperatures. Here the chiral phase boundaries for the different values of T_0 are located at different temperatures already at zero chemical potential, while they again coincide at small temperatures. With the Fukushima potential we find a critical end point at chemical potentials similar to the values found with the logarithmic potential, but at the expected lower temperatures because the Fukushima potential leads to a lower chiral phase boundary. The locations of the critical end points are listed in Tab. 4.3. For all shown models including the model without Polyakov loop the first-order transition at zero temperature commences at $\mu \sim 307\,\mathrm{MeV}$.

Summarizing the effect of the Polyakov loop potential on the chiral phase boundary, we can state that the Polyakov loop leads to a chiral restoration at higher temperatures. In

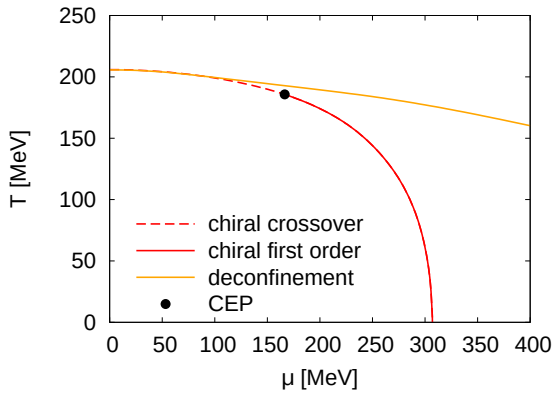

(a) Logarithmic $T_0 = 270\,\mathrm{MeV}$

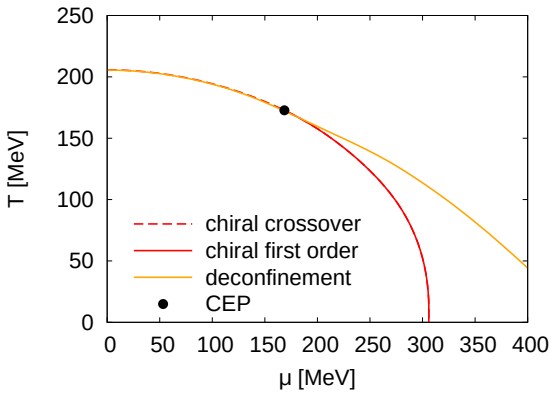

(b) Logarithmic $T_0(\mu), T_0(\mu = 0) = 270\,\mathrm{MeV}$

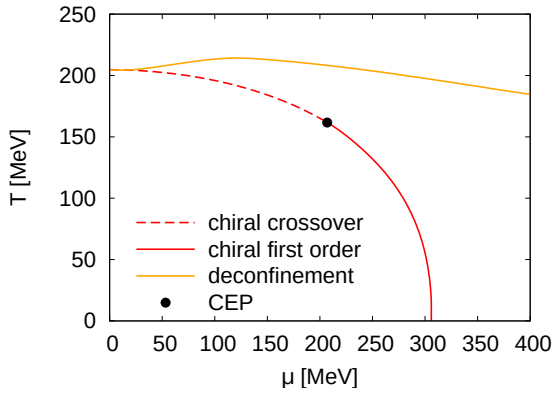

(c) Polynomial $T_0 = 270\,\mathrm{MeV}$

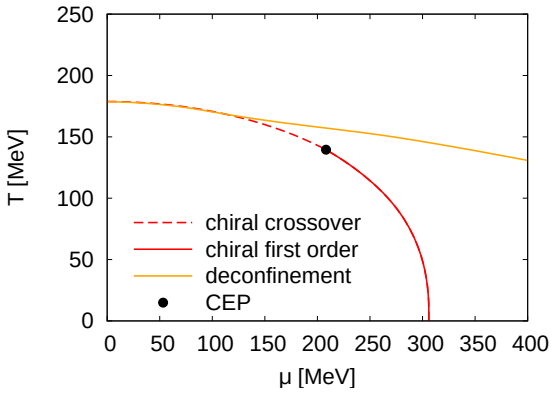

(d) Polynomial $T_0 = 208\,\mathrm{MeV}$

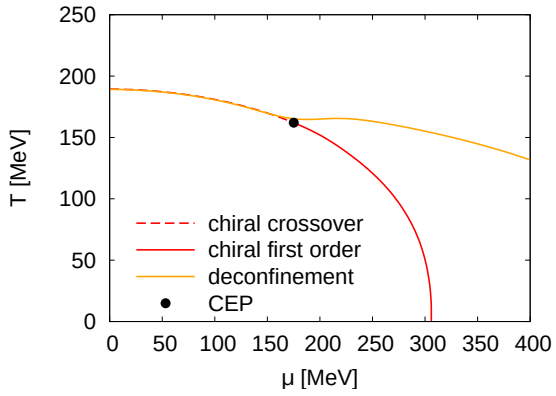

(e) Fukushima

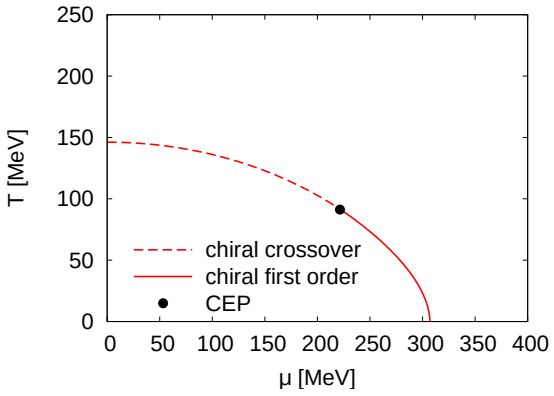

(f) QM

Figure 4.10.: Phase diagrams of the PQM model for different Polyakov loop potentials. For the underlying QM model $m_\sigma = 600\,\mathrm{MeV}$ was used and the $U(1)_A$ anomaly has been taken into account.

the μ-direction the influence is weak and vanishes at zero temperature. The critical point moves towards lower chemical potential due to the more rapid crossover at vanishing potential. The details, however, are model dependent.

Also shown in the phase diagrams is the deconfinement transition. For all potentials – including the modifications of T_0 for a finite number of quark flavors and finite chemical potential – the chiral and deconfinement transition split at some finite value of μ. This can be interpreted as the existence of a *quarkyonic* phase [82] in the PQM model. A similar effect has also been found in a PNJL study with three quark flavors [60]. Note that there a slightly different criterion ($\Phi = 0.5$) was used to determine the deconfinement transition. In general this leads to a deconfinement phase boundary at higher temperatures and a larger quarkyonic phase.

For the logarithmic potential we investigate the influence of the μ-dependent T_0. The deconfinement boundary is found at lower temperatures as T_0 is decreased with higher chemical potentials. This leads to a coincidence of the transitions up to $\mu \sim 200\,\mathrm{MeV}$. Without the modification, the transitions separate already at $\mu \sim 125\,\mathrm{MeV}$. For the Fukushima potential a similar behavior is seen as for the logarithmic potential with constant T_0.

A similar effect is seen when a lower value of T_0 is used to account for dynamical quarks, as shown for the polynomial potential. For a lower value of T_0 the transitions coincide up to $\mu \sim 150\,\mathrm{MeV}$. This is caused by the smaller gap of the deconfinement transition in the pure gauge limit and the chiral transition without Polyakov loop in this setup. For $T_0 = 270\,\mathrm{MeV}$ the transitions split already for very small values of μ. This indicates that already there the transitions are not really coinciding and it is just not possible to distinguish the two different transitions in the peak structure of the order parameters. A small rise in the deconfinement temperature is seen after the split of the transition. Whether this is a pure artifact of the way we determine the transition or has a actual physical significance is unclear. It might be that both transitions attract each other if they are not to far separated. In this case the transition that occurs first might trigger the other transition. Once the transitions are to far separated this triggering might not be sufficient to force the other transition. This has to be investigated in more detail.

Aside from the question of the right order parameter for the deconfinement transition at finite μ the situation is rather unsatisfying. While the coincidence of both transitions at zero chemical potential provides a guide on how to choose a Polyakov loop potential, many questions currently remain unanswered at finite chemical potential. For the fermionic sector the step to finite density is straightforward and even the freedom in the parameters of the underlying QM model is reduced if coincidence of both transitions in the range of the lattice results is required. The Polyakov loop potentials have been constructed in the pure gauge sector. Possible modifications to account for a finite number of quark flavors and at finite chemical potential, while certainly necessary, are presently only estimated roughly. Currently, this introduces some new ambiguities in the model calculations.

5. Thermodynamics

In this chapter the bulk thermodynamics of the PQM and the QM model is discussed. For vanishing chemical potential a comparison to lattice data obtained with $2+1$ flavors is carried out. Further results in the vicinity of the critical end point are discussed and compared among the models. Throughout this chapter we use $m_\sigma = 600\,\mathrm{MeV}$ for the QM model and take into account the $U(1)_A$ anomaly (cf. Chap. 3). For the polynomial and logarithmic Polyakov loop potentials $T_0 = 270\,\mathrm{MeV}$ is used.

The thermodynamic quantities can be derived from the grand potential Ω. E.g., the pressure is given by

$$p(T,\mu) = -\Omega\,(T,\mu) \tag{5.1}$$

with the normalization $p(0,0) = 0$. Other quantities like the quark number density or the specific heat discussed later in this chapter require the calculation of derivatives of the grand potential w.r.t T and μ. Instead of numerical derivatives a technique based on *algorithmic differentiation (AD)* has been used for the evaluation, allowing for very precise calculations. See App. B for details.

5.1. Results at vanishing chemical potential

In this section the results at vanishing chemical potential are discussed and compared with results obtained in lattice calculations. Recent lattice simulations by the RBC-Bielefeld cooperation [81] have been performed with physical strange quark masses but still not at physical light quark masses. These translate to $m_K = 503\,\mathrm{MeV}$ and $m_\pi = 220\,\mathrm{MeV}$ in physical units. For a better comparison of our model results with lattice results the pion and kaon masses have been tuned to these values using the explicit symmetry breaking parameters (cf. Chap.3). We will refer to these values as 'lattice point'.

The tuning results only in slightly heavier constituent quark masses,

$$m_q \approx 322\,\mathrm{MeV}\,(300\,\mathrm{MeV})\ , \quad m_s \approx 438\ \mathrm{MeV}(433\,\mathrm{MeV})\ , \tag{5.2}$$

where the masses at the physical point are given in parentheses. The influence on the bulk thermodynamics is expected to be weak. The phase diagram is slightly changed. The pseudocritical temperature rises from e.g. $T_\chi \approx 146\,\mathrm{MeV}$ to $T_\chi \approx 162\,\mathrm{MeV}$ in the model without Polyakov loop.

In general, one should keep several caveats in mind for the comparison with lattice data. The effect of the too high quark masses in lattice calculations may be different

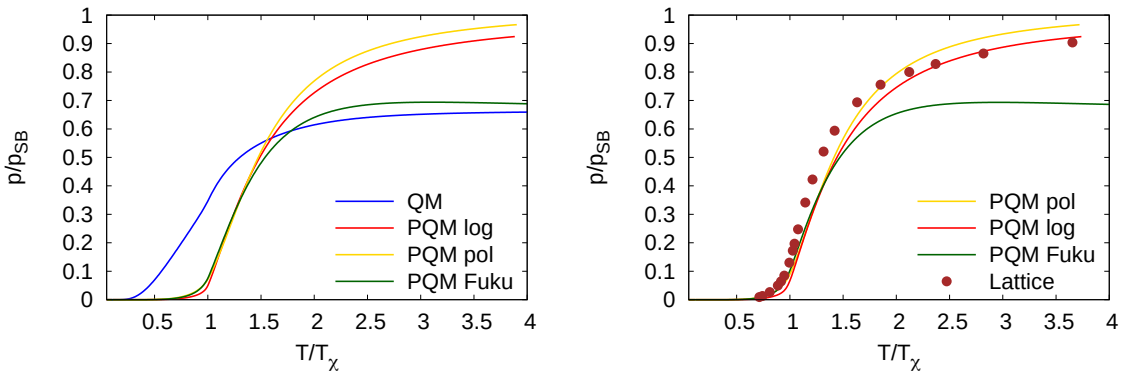

(a) physical point (b) lattice point

Figure 5.1.: The pressure normalized to the Stefan-Boltzmann value as a function of temperature for the different Polyakov loop potentials. In the left panel the pressure is shown for physical pion and kaon masses. For comparison also the result with Polyakov loop is shown. In the right panel the pressure is compared with lattice data ($N_\tau = 6$) from [81] at the lattice point. See text for details.

from what is achieved by our choice of the lattice point. Most lattice simulations have been performed on lattices with temporal extent $N_\tau = 4, 6$. The change when going from $N_\tau = 4$ to $N_\tau = 6$ is rather large. The step from $N_\tau = 6$ to $N_\tau = 8$ seems to be smaller, cf.[81]. Anyhow, the results are not yet converged and might change on larger lattices.

We begin our discussion of the thermodynamics with the pressure. Due to the asymptotic freedom an ideal gas behavior is expected at high temperatures: the asymptotic behavior should be given by the Stefan-Boltzmann (SB) value

$$\frac{p_{SB}}{T^4} = (N_c^2 - 1)\frac{\pi^2}{45} + N_c N_f \frac{7\pi^2}{180} \,. \tag{5.3}$$

The first term is the contribution of the gluons for N_c colors and the second the contribution of the N_f quark flavors.

We normalize the pressure to the SB value for the PQM model. Since the quark-meson model is lacking the contribution of the gluons it cannot reach a value of one. The corresponding SB limit for the QM model is $p_{SB}^{QM} \sim 0.66 p_{SB}^{PQM}$.

In Fig. 5.1 the pressure is shown for the different models at the physical point and in comparison with lattice data at the lattice point. In the QM model the pressure has already grown to $p \sim 0.5 p_{SB}^{QM}$ at the phase transition, while only $p \sim 0.1 p_{SB}^{PQM}$ is reached with an included Polyakov loop. The Polyakov loop suppresses the contribution of fermions below $T_d \approx T_\chi$, as expected. All Polyakov loop potentials result in a very

similar pressure up to $T \sim 1.2T_\chi$, with a slightly stronger suppression occurring for the logarithmic potential. This agrees nicely with the behavior of the condensates discussed in the previous chapter. For temperatures $T \gtrsim 1.5T_\chi$ the quarks are unconfined and their contribution agrees with the result of the QM model. The difference between the QM and PQM in the total pressure is the contribution of the Polyakov loop potential. As already discussed for the pure gauge sector the Fukushima potential does not contain the contribution of the transverse gluons at high temperatures. At high temperatures, where their contribution becomes important, the pressure obtained using the Fukushima potential is therefore closer to the value of the QM model. The polynomial and logarithmic potential contain transverse gluonic contribution as they are fitted to reproduce the pressure of pure gauge lattice calculations. Consequently, the pressure with this models approaches the SB value.

Note that we show the values for the models up to very high temperatures $T = 4T_\chi \sim 800\,\mathrm{MeV}$. Strictly, this is far beyond the region where the models are expected to work. The values there are only given for a rough comparison and to check expectations at very high temperatures.

In the right panel we compare the pressure with recent lattice data from [81]. A nice agreement with lattice data is found, however the model curves are shifted towards somewhat higher temperatures. This might be due to different ways of determining the pseudocritical temperature and errors in its value. Moreover, the suppression of the fermionic degrees of freedom might be too strong for the logarithmic potential. Note that it can however reproduce the lattice data at higher temperatures where the polynomial potential overestimates the pressure.

When comparing with lattice calculations below T_χ, one should keep in mind that in the QM and PQM models in mean-field approximation the contributions of mesonic fluctuations are neglected and the pressure is too low in the broken phase. The nice agreement with lattice data is assisted by the way the pressure is obtained in lattice calculations. In Monte Carlo calculations, the partition function is not directly accessible. Instead the trace of the energy-momentum tensor $\Theta^\mu_\mu = (\epsilon - 3p)/T^4$ is measured and the pressure is obtained via the integration [25]

$$p(T) = \int_{T_i}^{T} dT' \frac{1}{T'^5} \Theta^\mu_\mu \tag{5.4}$$

with some integration constant $p(T_i)$. The temperature T_i is chosen such that $p(T_i)$ is as small as possible, e.g., $T_i \sim 100\,\mathrm{MeV}$ [83]. Anyhow, the integration constant is nonzero, thus the contribution of the mesonic fluctuations missing in the mean-field approximation is also not fully included in the lattice data. Another possibility for the normalization of the lattice data is to use the value of $p(_i)$ from the hadron resonance gas which provides a realistic description of the pressure in the broken phase. These calculations show that $p(T_i) > 0$ and thus this shifts the lattice data to slightly higher values. In model calculations the mesonic fluctuation can be taken into account beyond

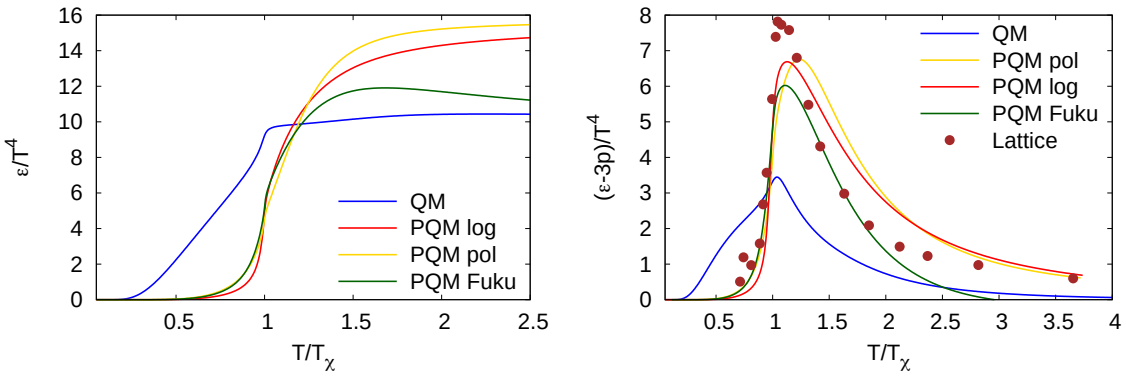

(a) Energy density

(b) Interaction measure

Figure 5.2.: Left panel: The energy density ϵ/T^4 as a function of temperature at the physical point, similar to Fig. 5.1(a). Right panel: The interaction measure $(\epsilon - 3p)/T^4$ as function of temperature at the lattice point. Lattice data ($N_\tau = 6$) taken from [81].

mean-field. There are calculations that take the contribution of the mesonic fluctuations into account, e.g., for the PNJL model [84].

To complete the discussion of the equation of state we show the energy density ϵ and the interaction measure $(\epsilon - 3p)$ in Fig. 5.2. The energy density at vanishing chemical potential is given by

$$\epsilon = -p + Ts \ , \tag{5.5}$$

with the entropy density

$$s = -\frac{d}{dT}\Omega \ . \tag{5.6}$$

The energy density behaves similar to the pressure. In the QM model the energy density reaches it final value already close to T_χ. The models with Polyakov loop show a suppression and reach the SB limit at higher temperature. The Fukushima potential leads to an overshoot around $T \sim 1.5 T_\chi$.

The interaction measure $(\epsilon - 3p)$ can be calculated using ϵ and p or directly from the grand potential as

$$\frac{\epsilon - 3p}{T^4} = T\frac{\partial}{\partial T}\frac{p}{T^4} = -T\frac{\partial}{\partial T}\frac{\Omega}{T^4} \ . \tag{5.7}$$

In the right panel (Fig. 5.2(b)) we compare the interaction measure also to lattice data with $N_\tau = 6$. Up to T_χ the Polyakov loop models are in reasonable agreement with lattice data. All models cannot reproduce the height of the peak at T_χ. Recall again that the height of the peak might change on larger lattices. Typically the peak is remarkable higher on smaller lattices $N_\tau = 4$ (cf. [81]) and might decrease with even larger lattices.

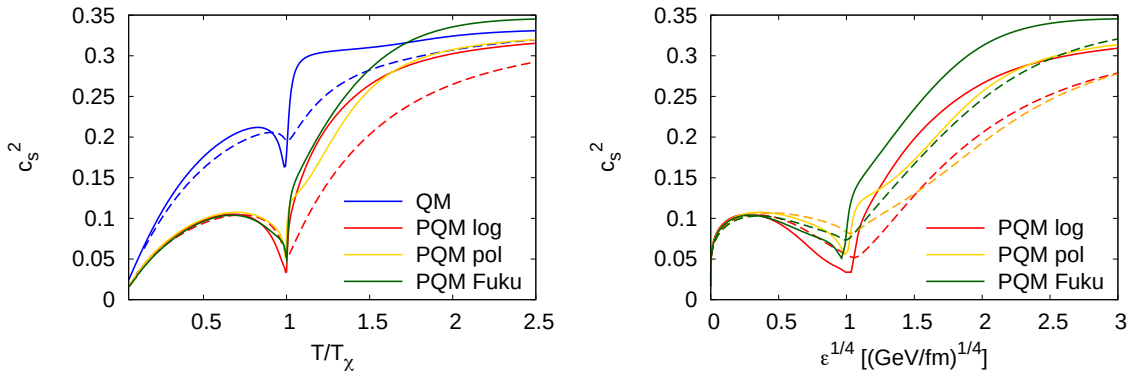

Figure 5.3.: The speed of sound c_s^2 (solid lines) as a function of temperature (left panel) and as a function of $\epsilon^{1/4}$ (right panel). For selected models also the ratio p/ϵ (dashed lines) is displayed.

In the symmetric phase the polynomial and logarithmic potential overestimate the interaction measure and approach the lattice value not until $T \sim 3.5T_\chi$. The Fukushima potential agrees better with the lattice data in the region $T_\chi < T < 2.0T_\chi$, but this is probably of no deeper physical meaning as it certainly cannot describe the energy density and the pressure for $T > 1.5T_\chi$.

The speed of sound, defined by

$$c_s^2 = \frac{dp}{dE} = \frac{dp}{dT} \Big/ \frac{d\epsilon}{dT} \tag{5.8}$$

is shown in Fig. 5.3 as a function of temperature in the left panel and a function of $\epsilon^{1/4}$ in the right panel. The speed of sound can be approximated by the ratio p/ϵ, which should be realized in the high-temperature limit

$$c_s^2 \to \frac{p}{\epsilon} \to \frac{1}{3} \, . \tag{5.9}$$

In the broken phase, p/ϵ is a rather good approximation when compared to the exact calculation. At the critical temperature a sharp dip is observed indicating the crossover. The dip is more pronounced in c_s^2 than in p/ϵ. For temperatures slightly above the phase transition c_s^2 is significantly smaller than p/ϵ. At high temperatures $c_s^2 \to p/\epsilon$ is found. p/ϵ has been calculated also in recent lattice simulations [81] as a function of $\epsilon^{1/4}$. In the right panel our results are also shown as functions of $\epsilon^{1/4}$. They nicely agree with lattice data for p/ϵ, indicating again a reasonable description of the equation of state with the PQM model. The speed of sound is an important input for the description of heavy ion collisions using hydrodynamics. The conditions in these collisions reach temperatures of the order of the pseudocritical temperature. The dip at the phase transition affects the

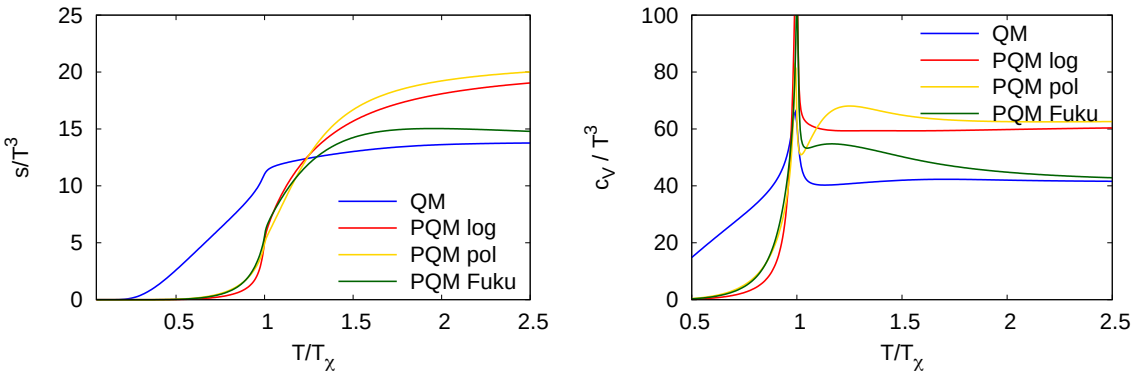

(a) Entropy

(b) c_V

Figure 5.4.: Left: The entropy density s/T^3 as function of temperature at the physical point for the various models. Right: The specific heat capacity at constant volume c_V/T^3 as a function of temperature.

stability of the hydrodynamical description of the collisions, cf., e.g., [85]. At the dip the equation of state has its softest point [86].

The entropy density (5.6) and the specific heat capacity at constant volume,

$$c_V = -T\frac{\partial^2\Omega}{\partial T^2}\ , \tag{5.10}$$

are displayed in Fig. 5.4. The entropy density shows a similar behavior as the energy density. The specific heat capacity shows a strong peak at the phase transition. Without the Polyakov loop a slow rise is observed in the broken phase, whereas with the Polyakov loop the values are very small and then rise steeply for $T \gtrsim 0.5T_\chi$. In the symmetric phase a constant value is reached.

The Fukushima potential shows a small plateau in the range of temperatures slightly above T_χ and approaches the QM model value for higher temperatures. The plateau is caused by modeling the gluonic degrees of freedom with the Polyakov loop potential. As already discussed in the Fukushima potential the Polyakov loop contribution vanishes at high temperatures. The contribution of transverse gluons that take over at high temperatures is not included in the model. The drop in the heat capacity after the plateau corresponds to the vanishing of the effective gluonic degrees of freedom in the Fukushima potential. The polynomial potential produces an oscillation above T_χ, it drops below the value of the logarithmic potential directly after the phase transition. This might indicate that the quarks are not yet fully deconfined in the polynomial model. The slight overshooting before the constant value is reached might also be a hint for a slightly delayed deconfinement transition for this potential.

In the considered 2+1 flavor scenarios we can examine the quark number densities for

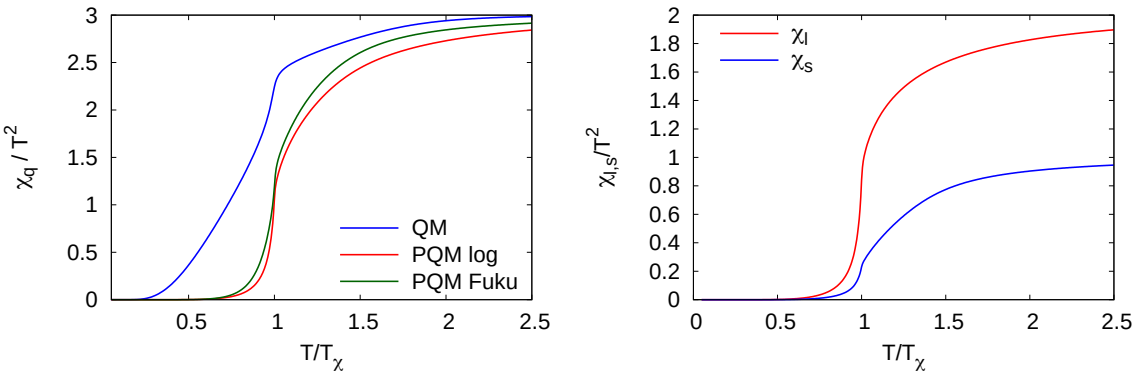

(a) χ_q (b) $\chi_{l,s}$

Figure 5.5.: Left: The total quark number susceptibility χ_q/T^2 for different Polyakov loop potentials as function of T at vanishing chemical potential. Right panel: Similar to left panel, but for the strange (χ_s/T^2) and non-strange (χ_l/T^2) quark number susceptibilities.

the total quark number

$$n_q = -\frac{\partial\Omega}{\partial\mu_q} = -3\frac{\partial\Omega}{\partial\mu_B} \tag{5.11}$$

and the light and strange quarks

$$n_l = -\frac{\partial\Omega}{\partial\mu_l} \ , \quad n_s = -\frac{\Omega}{\partial\mu_s} \ , \tag{5.12}$$

respectively. Obviously the total quark number density is the sum of the strange and non-strange quark densities

$$n_q = n_l + n_s \ .$$

Analogously we can calculate the total quark number susceptibility

$$\chi_q = \frac{\partial n_q}{\partial\mu_q} = -\frac{\partial^2\Omega}{\partial\mu_q^2} \tag{5.13}$$

as well as the light and strange quark number susceptibilities

$$\chi_l = \frac{\partial n_l}{\partial\mu_l} \ , \quad \chi_s = \frac{\partial n_s}{\partial\mu_s} \ . \tag{5.14}$$

At very high temperatures the susceptibilities should approach the Stefan-Boltzmann value $\chi_q/T^2 \to N_c N_f/3$.

In Fig. 5.5 the total quark number susceptibility is shown for different Polyakov loop potentials. Without the Polyakov loop, the susceptibility reaches values $\chi_q/T^2 > 2$

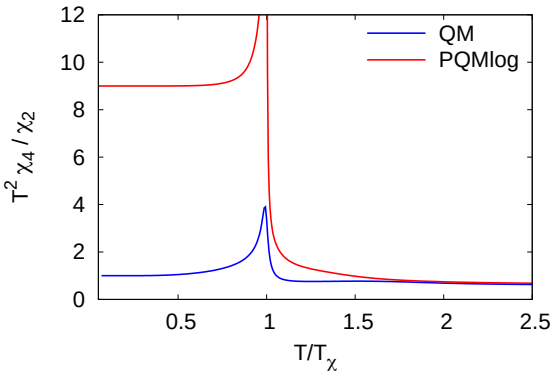

Figure 5.6.: The ratio of the 4-th and 2-nd derivatives w.r.t. the different chemical potentials as function of temperature for the QM model and the PQM model with logarithmic potential.

already at the chiral phase transition and approaches $\chi_q/T^2 \sim 3$ at higher temperatures. A slight delay is caused by the restoration of chiral symmetry in the strange sector at higher temperatures. With the Polyakov loop the rise of the susceptibility occurs at higher temperatures and only values $\chi_q/T^2 \sim 1.5$ are reached at the phase transition.

In the right panel (Fig. 5.5(b)) the strange and non-strange susceptibilities are shown for the model with logarithmic Polyakov loop potential. At $T = T_\chi$ the non-strange susceptibility χ_l shows a steep rise while the strange susceptibility jumps only a little. At high temperatures the susceptibilities reach their Stefan-Boltzmann values of $\chi_l/T^2 \sim 2$ and $\chi_s/T^2 \sim 1$ for two light and one strange flavor, respectively.

The ratio of the 4-th derivative of the grand potential w.r.t. μ, $\chi_{q,4} = -\partial^4\Omega/\partial\mu_f^4$, with the quark number susceptibility χ_q can be used as a measure for confinement,

$$R_{q(4,2)} = \frac{\chi_{q,4}}{\chi_{q,2}} = \frac{\chi_{q,4}}{\chi_q} \,. \tag{5.15}$$

It gives the squared number of quark content in the excited particles carrying baryon number. In a confined phase this ratio should be $R_{q(4,2)} = 3^2$. This corresponds to colorless three quark states in the model. In an unconfined phase the value should be roughly 1^2. At very high temperatures the SB value $R^{SB}_{q(4,2)} \to 6/\pi^2$ is approached (see also [87]).

In Fig. 5.6 $R_{q(4,2)}$ is shown for the PQM model and the QM model. In the QM model the quarks are never confined, the ratio is one already in the broken phase. In the PQM model the ratio is nine, as expected in the broken phase. At the phase transition the ratio shows a peak, which is more pronounced in the model with Polyakov loop due to the more rapid crossover.

5.2. Finite chemical potential

The quark number density (5.11) is an enlightening quantity concerning the suppression of the quarks by the Polyakov loop. In the confined phase a significantly lower quark number density is expected.

For finite μ it is instructive to consider the quark number density in the (T, μ)-plane. Since it increases strongly with T and μ we normalize it to its free, ideal gas value

$$n_q^{\text{free}} = N_c N_f \left(\frac{\mu^3}{3\pi^2} + \frac{T^2 \mu}{3} \right) \ . \tag{5.16}$$

At high temperatures or high chemical potentials a value of $n_q/n_q^{\text{free}} \to 1$ is expected.

In Fig. 5.7 the quark number density is shown for the QM and the PQM model with the logarithmic Polyakov loop potential. Without the Polyakov loop the quark number density increases significantly already in the broken phase. At the chiral phase boundary it reaches a value of $n_q/n_q^{\text{free}} \sim 2/3$. This is roughly the contribution of the two light quarks as $n_l^{\text{free}}/n_q^{\text{free}} = 2/3$ or correspondingly $n_l/n_l^{\text{free}} \sim 1$. This rise is mainly due to the nearly chirally restored light quarks. Since a small contribution from the strange quarks is already included, we still have $n_l/n_l^{\text{free}} < 1$.

A value of $n_q/n_q^{\text{free}} \sim 1$ is reached when the chiral symmetry has also been restored in the strange sector (cf. Chap.3). At small temperatures, the first-order transition in the light sector at $\mu \sim 300\,\text{MeV}$ and the crossover in the strange sector at $\mu \sim 450\,\text{MeV}$ are clearly visible in the figure.

With the Polyakov loop, the quark number density is zero in the broken phase and rises only slightly towards the crossover transition at small chemical potential. At the chiral phase transition it reaches a value of $n_q/n_q^{\text{free}} \sim 1/3$, corresponding to $n_l/n_l^{\text{free}} \sim 1/2$. Except from the suppression in the broken phase, the overall behavior is similar to the case without the Polyakov loop at small μ.

At higher chemical potentials, the behavior is different. At $T \sim 150\,\text{MeV}$ and $\mu \gtrsim 250\,\text{MeV}$ we find a region with a suppressed quark number density. The quark number density increases for higher temperatures and chemical potentials, as expected, but also towards lower chemical potentials resulting in the circular shape seen in Fig. 5.7(b). This is a qualitatively new feature in the model with Polyakov loop. To understand this feature it is helpful to recall the behavior of the order parameters in this region, cf. Fig 4.5. The Polyakov loop is always very small at zero temperature and only slightly bends towards the μ-axis, hence it mainly suppresses the quark number density caused by finite temperature. The suppression of the quark number density and the rise towards higher temperatures in this region is caused by the rise of the Polyakov loop in this region. The rise towards smaller temperatures indicates that the Polyakov loop does not suppress the quark number density at small chemical potentials. This region corresponds to *quarkyonic matter* [82] in the PQM model. The quark number density in this region is clearly distinguished from the hadronic phase, thus quark degrees of freedom are relevant. For chemical potentials below the Fermi energy the fermionic

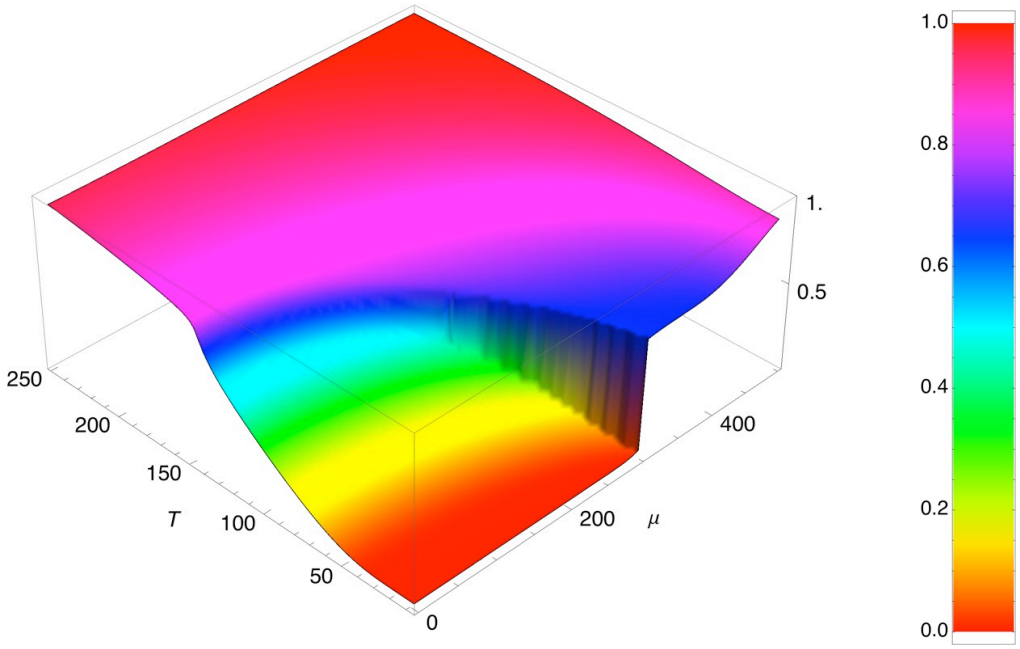

(a) QM

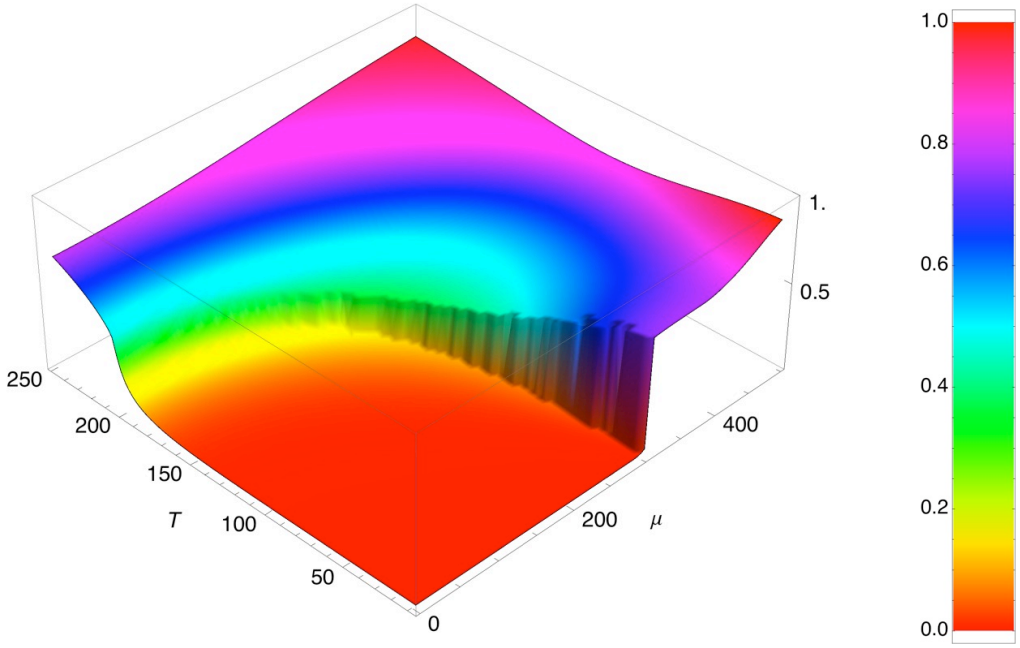

(b) PQM

Figure 5.7.: The normalized quark number density n_q/n_q^{free} as a function of T and μ for the QM and PQM model with logarithmic Polyakov loop potential ($T_0 = 270\,\text{MeV}$).

contribution to the grand potential is vanishing. In this region the Polyakov loop is also vanishing. The Polyakov loop potential itself does not feel the quark chemical potential and the Polyakov loop potential is identical to the on in the vacuum. As stated in [60] for chemical potentials above the Fermi surface the term $\exp\left(-3(E_q-\mu)/T\right)$ in the fermionic contribution (cf. Eq. 4.27) dominates in the low temperature region. This term represents an occupation for three quarks and does not break the $Z(3)$ symmetry.

In Fig. 5.8 we show the quark number susceptibility in the (T,μ)-plane normalized by its free value

$$\chi_q^{\text{free}} = N_c N_f \left(\frac{\mu^2}{\pi^2} + \frac{T^2}{3}\right) \ . \tag{5.17}$$

with and without Polyakov loop[1]. As the quark number susceptibility is closely related to the quark number density several features, like the suppression in the broken phase and the chiral phase boundary, are also observed in the susceptibility. However, at the CEP a peak is observed and the susceptibility is enhanced in the vicinity of the CEP. The peak at the CEP is sharper in the model with the Polyakov loop. We will discuss the behavior at and around the CEP in the next section in more detail.

[1]The structure in the peaks is caused by the sampling in the (T,μ) plane used for the creation of the plot.

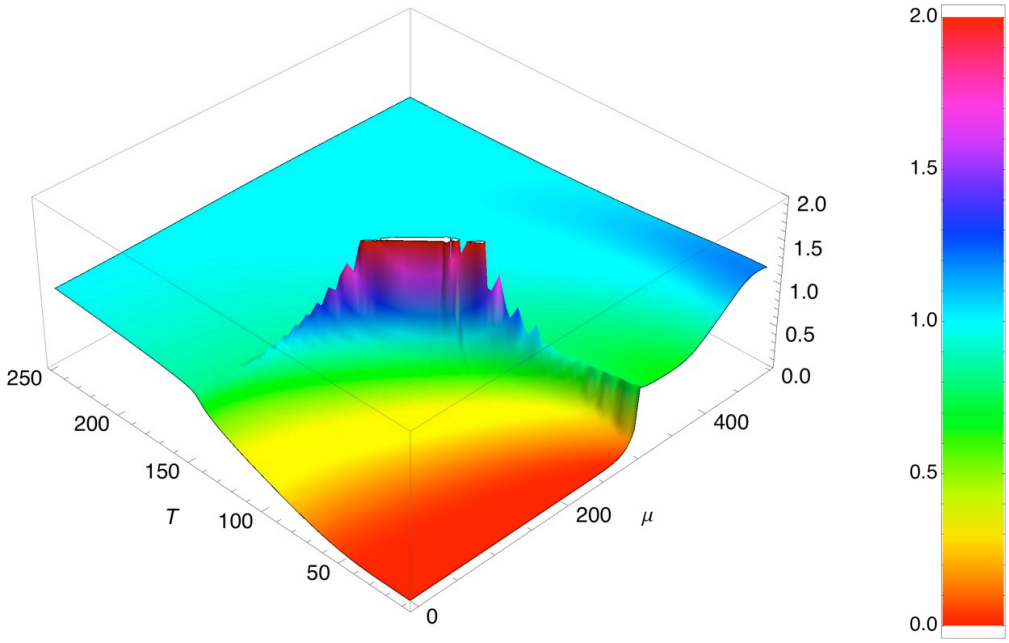

(a) QM

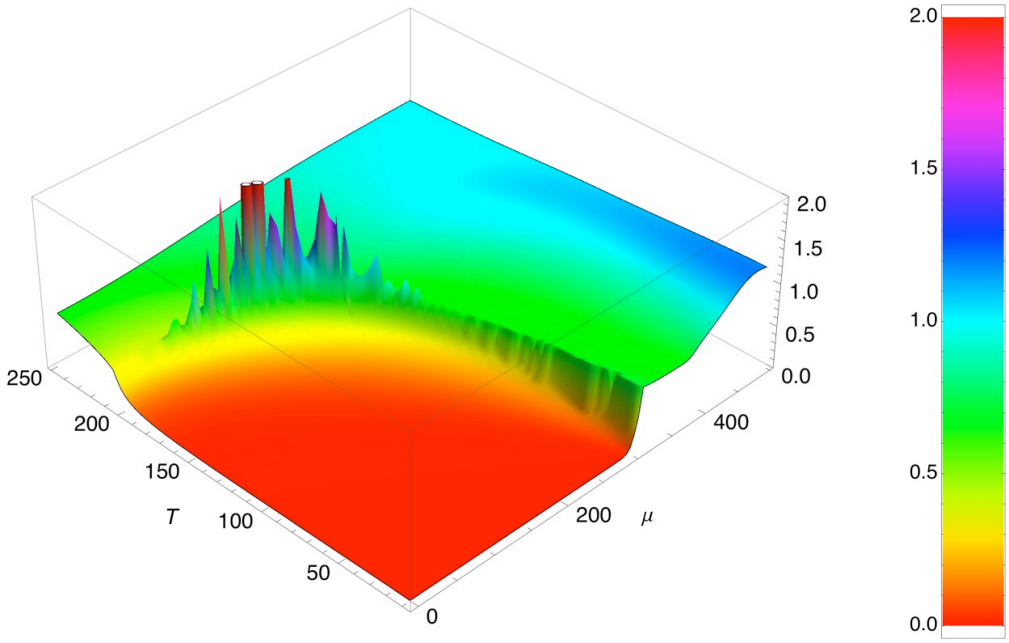

(b) PQM

Figure 5.8.: The normalized quark number susceptibility $\chi_q/\chi_q^{\text{free}}$ as a function of T and μ for the QM and PQM model with logarithmic Polyakov loop potential ($T_0 = 270\,\text{MeV}$).

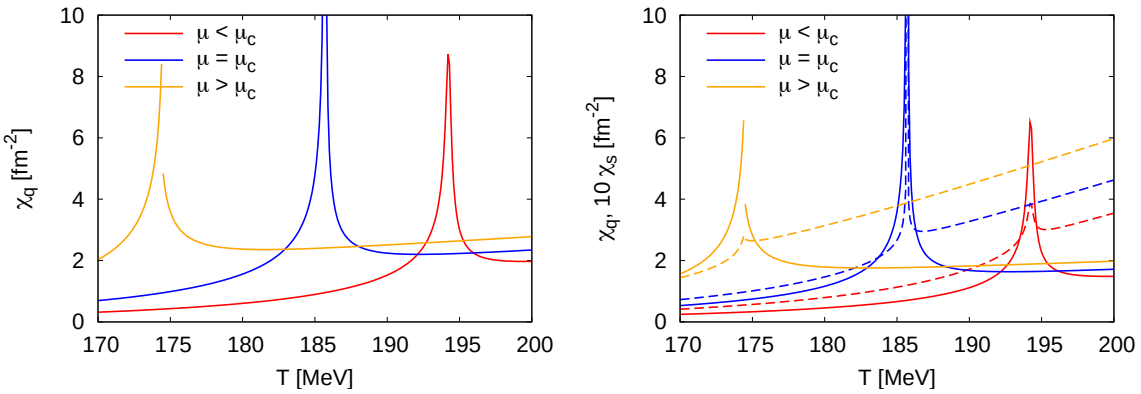

(a) χ_q (b) χ_l, $10\chi_s$

Figure 5.9.: Left: The quark number density χ_q as function of temperature for chemical potentials below, at and above the critical chemical potential in the PQM model with the logarithmic potential. Right: Similar to the left plot, but for the strange χ_s (dashed lines) and non-strange χ_l (solid lines) quark number susceptibilities. Note, that the results for the strange susceptibility has been multiplied by a factor of ten.

5.3. Results in the critical region

At the critical end point the phase transition is of second order and the order parameter has an infinite slope. A consequence of this infinite slope or divergence in the derivative of the order parameter are divergences in several thermodynamic quantities. These divergences provide a clear signal for the critical end point. In the models the critical end point can also be extracted from the order parameter directly, but the order parameters are not measurable in the experiments. The effect of the divergences of thermodynamic quantities, however, can be measured.

We start our discussion with the quark number susceptibilities in the PQM model shown in Fig. 5.9 as function of temperature for $\mu < \mu_c$, $\mu = \mu_c$ and $\mu > \mu_c$. The total quark number susceptibility χ_q displayed in the left panel shows a finite peak for $\mu < \mu_c$ since the transition is a smooth crossover. At the critical end point the curve for $\mu = \mu_c$ shows a divergence and for $\mu > \mu_c$ a finite peak with a jump due to the first order transition is observed. The contributions of the light (χ_l) and the strange quarks (χ_s) are shown in the right panel. The total quark number susceptibility is dominated by the contribution of the light quarks χ_l. The value for the strange quark number susceptibility has been multiplied with a factor of 10 for visibility. For $\mu \neq \mu_c$ the strange quark number susceptibility only has a small peak at the transition while it shows a prominent peak at the critical end point.

The isothermal compressibility κ_T is related to the quark number susceptibility and

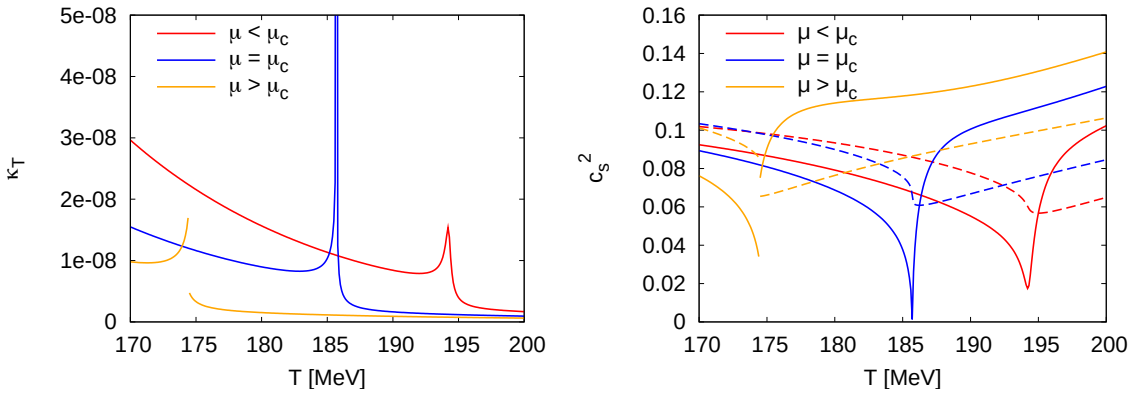

(a) κ_T (b) c_s^2

Figure 5.10.: Left: The isothermal compressibility κ_T as function of temperature for various chemical potentials similar to Fig. 5.9. Right: Same as left but for the speed of sound c_s^2 (solid lines) and the ratio p/ϵ (dashed line).

density via

$$\kappa_T = \frac{\chi_q}{n_q^2} \ . \tag{5.18}$$

It also diverges since the quark number density is finite while the quark number susceptibility diverges. A diverging compressibility indicates that the system is easy to compress and the interactions are more attractive at the critical end point [88]. In the isothermal compressibility shown in Fig 5.10(a) a very sharp peak is observed at the critical end point. For $\mu \neq \mu_c$ the values are finite, similar to the quark number susceptibility.

The speed of sound already discussed at vanishing chemical potential should drop to zero at the critical end point. In Fig. 5.10(b) we show the speed of sound c_s^2 as well as the ratio p/ϵ which should approach the speed of sound at high temperatures. The ratio p/ϵ has a drop at the phase transition for all shown chemical potentials. A drop to zero is not expected since the pressure and energy density are finite at the critical end point. The speed of sound drops to zero at the critical end point but stays finite for the curves with $\mu \neq \mu_c$. The speed of sound is related to the specific heat capacity by

$$c_s^2 = -\frac{1}{c_V}\frac{\partial \Omega}{\partial T} = \frac{s}{c_V} \ . \tag{5.19}$$

The drop to zero of the speed of sound is connected to the divergence in the specific heat because the entropy density s is always finite.

The specific heat is shown for the QM and PQM model in Fig. 5.11. In general the specific heat rises with temperature and chemical potential. The overall behavior of the peaks is very similar to the susceptibilities already discussed. The detailed behavior of the divergences at the critical end point is discussed in the next section.

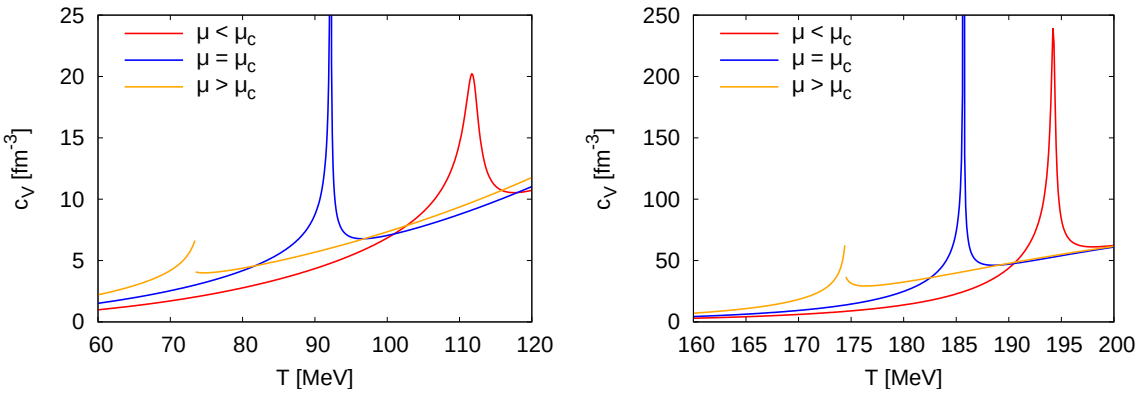

(a) QM (b) PQM

Figure 5.11.: The specific heat capacity at constant volume c_V as function of temperature similar to Fig. 5.9. The left panel shows the result in the QM model, the right panel in the PQM model with logarithmic Polyakov loop potential.

5.3.1. Critical exponents

As previously discussed several quantities diverge at the critical point. In the scaling region these divergences can be described by a power law with a characterizing exponent. Due to long-range fluctuations in the scaling region the microscopic details of the system are irrelevant and the exponents of the power laws are universal. Different physical systems in one universality class, i.e., with the same critical exponents, share the same critical behavior. For an introduction see, e.g., [89].

Despite the fact that the mean-field approximation is known to fail in reproducing the correct exponents due to missing fluctuations a scaling behavior is observed. Being able to calculate derivatives with high precision using algorithmic differentiation (AD) the scaling can be explored over many order of magnitudes.

In general, the shape of the divergence depends on the route by which the critical point is approached. The only direction distinguished in the (T, μ) plane is the one parallel to the phase boundary. For an approach along this direction critical exponents might take different values than along any other path [90].

We define the reduced variables

$$\hat{t} = \frac{T - T_c}{T_c} , \qquad \hat{\mu} = \frac{\mu - \mu_c}{\mu_c} . \tag{5.20}$$

To approach the CEP from arbitrary directions in the (T, μ) plane we use polar coordinates around the CEP

$$(\hat{\mu}, \hat{t}) = (r \cos\varphi, r \sin\varphi) \tag{5.21}$$

with an angle φ specifying the direction and the reduced distance from the CEP given

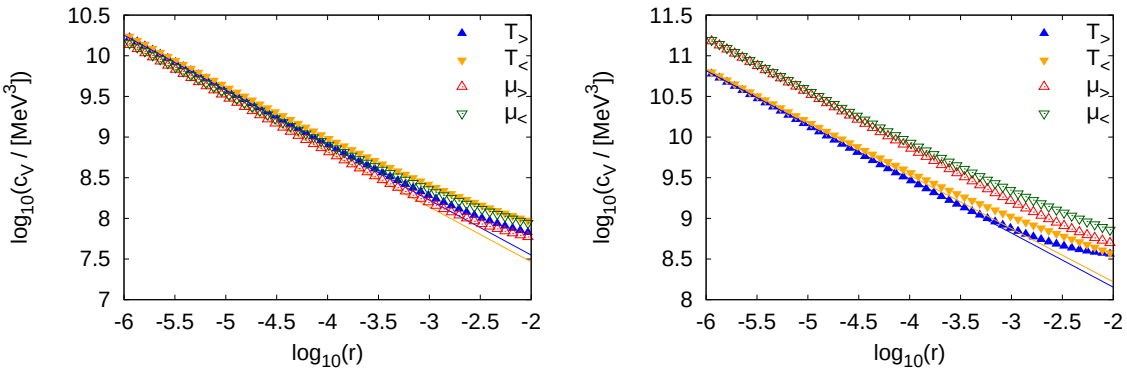

(a) QM (b) PQM

Figure 5.12.: The logarithm of the specific heat capacity c_V as a function of $\log_{10}(r)$ at the critical point. $T_>$ and $T_<$ ($\mu_>$ and $\mu_<$) denote a path towards the critical point at $\mu = \mu_c$ ($T = T_c$) for $T > T_c$ and $T < T_c$ ($\mu > \mu_c$ and $\mu < \mu_c$), respectively. The left panel shows the result in the QM model, the right panel in the PQM model. The solid lines are linear fits to the data.

as

$$r = \sqrt{\hat{t}^2 + \hat{\mu}^2} \ . \tag{5.22}$$

For an approach towards the critical end point from an arbitrary direction it is not unambiguous whether to use some reduced distance as defined above or to use $\hat{t}$ and $\hat{\mu}$ when applicable. Our definition of r follows the considerations in [90].

In Fig. 5.12, the exponent α related to the specific heat

$$c_V \propto r^{-\alpha} \tag{5.23}$$

is shown for the QM and PQM models. The divergence is approached along a path with $\mu = \mu_c$ and temperatures below ($T_<$) and above ($T_>$) T_c as well as for path with $T = T_c$ and chemical potentials above and below the critical value denoted by $\mu_>$ and $\mu_<$, respectively.

The value of α has been determined using a linear fit. In the QM and PQM model with the logarithmic Polyakov loop potential a value in agreement with $\alpha = 2/3$ is obtained for the considered directions. The numerical value tends to be a bit smaller than 2/3 in the broken phase and a bit larger in the symmetric phase. This effect is more pronounced in PQM model. However, the values still agree with each other within errors. The same effect is seen also for the exponent ϵ discussed below. The detailed values of our calculation are summarized in Tab. 5.1. For a larger distance $\log_{10}(r) \gtrsim -4$ a deviation from the scaling solution is found. This deviation depends on the direction from which the CEP is approached.

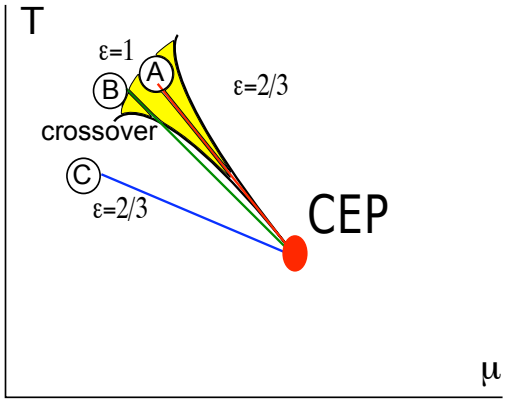

Figure 5.13.: The region with the critical exponent $\epsilon = 1$. Also shown are three different paths towards the critical end point, on exactly parallel (A) to the phase boundary and two with an increasing deviation (B,C). See text for details.

We emphasize that it is crucial to determine the CEP very precisely and check that the scaling region is really reached. For larger values of r, small regions, e.g., for $-4 < \log_{10}(r) < -3$ of about one order of magnitude, can be found which could be interpreted as scaling regions. We have determined the location of the critical end point with a precision of at least $\hat{t}, \hat{\mu} < 10^{-6}$. This value has been determined from the scaling behavior at small values of r. For values of r on the order of the precision of the determination of the CEP a deviation from the scaling is found. The path bypasses the CEP sideways. In Fig. 5.12 no deviation from the scaling is found for a distance from the CEP down to $\log_{10}(r) \sim -6$.

The value of the condensate near the critical point scales with the exponent β. Since the critical end point is a feature of the non-strange condensate σ_x we consider its deviation from the critical value $\sigma_{x,c}$. The exponent is extracted from

$$(\sigma_x - \sigma_{x,c}) \propto r^{\beta} \ . \tag{5.24}$$

We find a value of $\beta \sim 1/3$, again with slight deviations depending on wether the divergence is approached from the broken or the symmetric phase (cf. Tab 5.1).

For the exponent ϵ related to the quark number susceptibility

$$\chi_q \propto r^{-\epsilon} \tag{5.25}$$

we consider the approach in different directions. As already in seen in Fig. 5.8 the susceptibility is enhanced along the phase transition. This is the only distinguished direction in the (T, μ) plane. For a path parallel to this direction a value of $\epsilon = 1$ is expected. For any other direction a value of $\epsilon = 1 - 1/\delta = 2/3$ is expected, because $\delta = 3$ in mean-field.

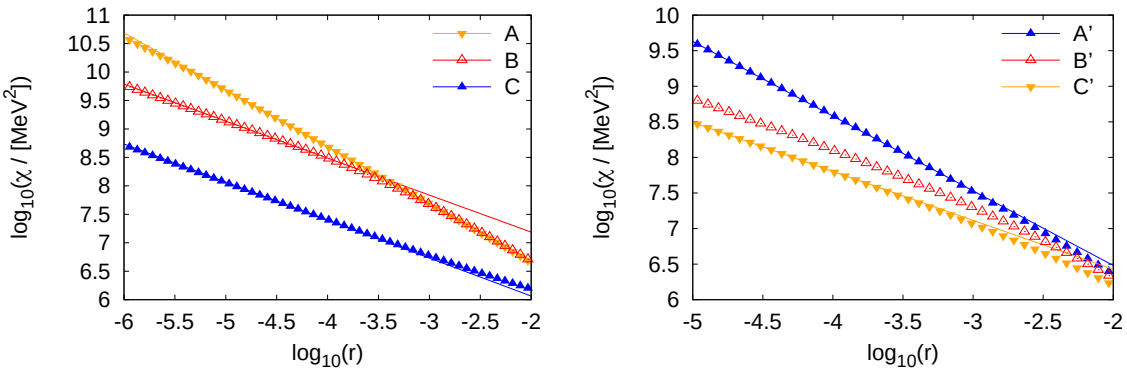

(a) QM (b) PQM

Figure 5.14.: The logarithm of the quark number susceptibility χ_q as a function of $\log_{10}(r)$. The left figure shows the results for a path parallel (A) and with slight deviation from the crossover transition (B,C) in the QM model. The right panel shows a paths parallel to the first order transition (A') and with slight deviation (B',C') in the PQM model. See text for details.

In Fig. 5.13 we show different paths towards the CEP. The black lines limit the yellow region in which $\epsilon = 1$ is expected. For the blue line (C) a value of $\epsilon = 2/3$ is expected. For the red line (A) exactly parallel to the phase boundary $\epsilon = 1$ is expected. The most interesting behavior is expected for the path (B) with deviates only slightly from the parallel path. For small values of r, a value of $\epsilon = 2/3$ is expected. At larger values of r it enters the $\epsilon = 1$ region. A crossover behavior between the two exponents is expected along this path. From the position of this crossover the boundaries of the $\epsilon = 1$ region can be determined. In this generic figure we have shown the $\epsilon = 1$ region only in the direction of the crossover transition. The same behavior is also expected in the direction of the first-order transition. We denote the corresponding paths as A', B' and C'.

In Fig. 5.14 we show the scaling for the three directions discussed above. In the left panel we show the approach along the crossover ($\mu < \mu_c, T > T_c$) in the QM model. In the right panel a path along the first-order transition ($\mu > \mu_c, T < T_c$) was chosen in the PQM model. For both figures we also show a linear fit for the directions A (A') and C (C'). From this fit a value of $\epsilon \sim 1$ is extracted for the paths exactly parallel to the first-order transition (A) and (A') in the QM and PQM model, respectively. For slightly changed values of φ (curves B and B') in both models a crossover between an exponent $\epsilon \sim 1$ and $\epsilon \sim 2/3$ is observed. For even stronger deviations (curves C and C') $\epsilon \sim 2/3$ is found. Note that the deviations between A (A') and C (C') are very small, $\Delta\varphi \sim 0.5^\circ$ (0.1°).

One can define critical exponents for various other quantities that show a scaling relation. The different critical exponents are not all independent, but linked via several

(a) QM

exponent	direction	value
α	$\hat{t} > 0$	0.67 ± 0.01
α	$\hat{t} < 0$	0.66 ± 0.01
α	$\hat{\mu} > 0$	0.67 ± 0.01
α	$\hat{\mu} < 0$	0.66 ± 0.01
β	$\hat{t} > 0$	0.32 ± 0.01
β	$\hat{t} < 0$	0.34 ± 0.01
β	$\hat{\mu} > 0$	0.32 ± 0.01
β	$\hat{\mu} < 0$	0.34 ± 0.01
ϵ	$\hat{t} > 0$	0.67 ± 0.01
ϵ	$\hat{t} < 0$	0.66 ± 0.01
ϵ	$\hat{\mu} > 0$	0.67 ± 0.01
ϵ	$\hat{\mu} < 0$	0.66 ± 0.01
ϵ	A'	1.00 ± 0.01
ϵ	A	1.01 ± 0.01

(b) PQM

exponent	direction	value
α	$\hat{t} > 0$	0.67 ± 0.02
α	$\hat{t} < 0$	0.65 ± 0.02
α	$\hat{\mu} > 0$	0.67 ± 0.02
α	$\hat{\mu} < 0$	0.65 ± 0.02
β	$\hat{t} > 0$	0.32 ± 0.01
β	$\hat{t} < 0$	0.34 ± 0.01
β	$\hat{\mu} > 0$	0.32 ± 0.01
β	$\hat{\mu} < 0$	0.34 ± 0.01
ϵ	$\hat{t} > 0$	0.67 ± 0.01
ϵ	$\hat{t} < 0$	0.66 ± 0.01
ϵ	$\hat{\mu} > 0$	0.67 ± 0.01
ϵ	$\hat{\mu} < 0$	0.66 ± 0.01
ϵ	A'	1.00 ± 0.02
ϵ	A	1.01 ± 0.02

Table 5.1.: Summary of the critical exponents in the QM model and the PQM model with logarithmic Polyakov loop potential ($T_0 = 270\,\mathrm{MeV}$).

scaling relations. With the exponents calculated so far we can check the scaling relation

$$2\beta + \epsilon = 2 - \alpha \ . \tag{5.26}$$

Using e.g. the values for the QM model for an approach at $\mu = \mu_c$ and $t < 0$ we find for the left hand side $2\beta + \epsilon \approx 1.34$ and for the right hand side $2 - \alpha \approx 1.34$ and (5.26) is satisfied. The scaling relation can be checked also for the other values given in Tab. 5.1 and is always satisfied within the errors.

5.3.2. Size of the critical region

The quark number susceptibility diverges at the critical end point. For the experimental search it is necessary to understand how this divergence affects the complete T, μ plane. As discussed in Sect. 2.3, an experimental search can only scan in certain directions in the (T, μ) plane. The probability of finding signatures of the critical end point in experiments is therefore related to the size of the region where fluctuations are significantly increased. We define the critical region as the area in which the ratio of the susceptibility and the free susceptibility (cf. Eq. 5.17) is above a certain limit, following [50, 91]. For the quark number susceptibility the ratio is defined as

$$R(T, \mu) = \frac{\chi_q(T, \mu)}{\chi_q^{\mathrm{free}}(T, \mu)} \ . \tag{5.27}$$

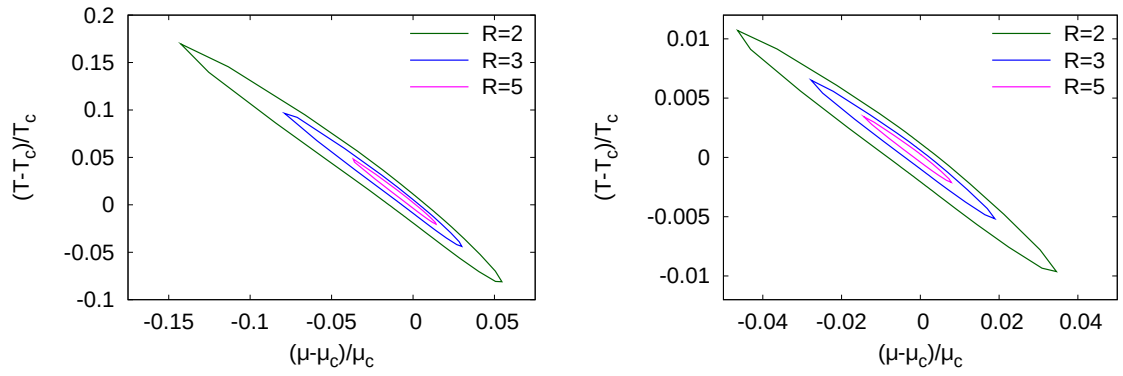

(a) QM (b) PQM

Figure 5.15.: The critical region in the QM (left) and the PQM model with logarithmic potential (right). Note the different scales.

In Fig. 5.15 the critical regions are shown as contour plots in the QM and PQM model. The critical region shows an elongated shape in the direction of the phase transition. In the QM model the region is not symmetric in this direction, but enhanced in the direction of the crossover roughly by a factor of two. This significant enhancement is not seen in the PQM model. There a much smaller critical region is observed. Note that the scales are different in the two figures. In Fig. 5.8 we have already shown the ratio $R = \chi_q/\chi_q^{\text{free}}$ in the (T, μ) plane. The apparently smaller size of the critical region partly stems from the used definition. The value of R is much smaller in the broken phase and at the phase boundary in the PQM model since the fermionic fluctuations are suppressed by the Polyakov loop. The enhancement due to the divergence is partly eaten up by the smaller regular part of χ_q. Further note that for the two models the CEPs are located in different regions of the phase diagram. In the PQM model the phase boundary is rather parallel to the μ-axis. The phase boundary is rotated by roughly 14° compared to the μ-axis, so the temperature is nearly constant along the phase boundary near the CEP. In the QM model, the CEP is located at higher chemical potential and smaller temperature. In this region the phase boundary is rotated by $\sim 38°$ relative to the μ-axis, so the temperature changes noticeably along the phase transition. The enhancement of the critical region in the QM goes along with higher temperatures.

The elongated shape of the critical region can be understood from the different scaling exponents in different directions. For a path parallel to the first order transition we found $\epsilon \sim 1$ and for any other direction $\epsilon \sim 2/3$. Using the precise AD calculations we were able to determine a boundary of the region with $\epsilon \sim 1$. Fig. 5.16 shows a detailed view of the critical region (Fig. 5.15(a)) with a calculation of the boundary of the $\epsilon \sim 1$ region. It agrees with our expectations shown in Fig. 5.13. The black lines indicate the region with $\epsilon \sim 1$. The regions are not sharply separated but we find a rather smooth

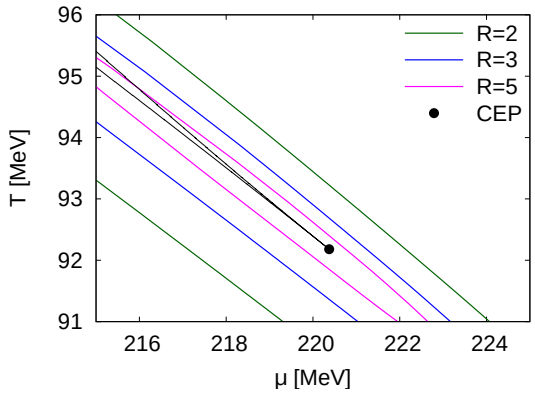

Figure 5.16.: Critical region similar to Fig. 5.15(a) in the QM model. The black lines display the boundary of the region with $\epsilon = 1$.

crossover between the two regions. A similar behavior is also found in the direction of the first-order transition as well as in the PQM model. Note, that the region is extremely sharp. For a deviation of five MeV from the critical end point in the μ-direction the region has only an extension in the T-direction of $\sim 0.2\,\mathrm{MeV}$. This confirms that a very precise determination of the direction with a deviation less then $0.001°$ is required to find a value of $\epsilon = 1$.

6. Finite density extrapolations

Although studies at finite chemical potential are straightforward in model calculations the application of approximations used in lattice calculations should be considered. Effective models are currently the only way to study the QCD phase diagram at arbitrary chemical potential. This enables us to compare the results of extrapolations methods to finite chemical potential methods (cf. Sect. 2.2.1) with calculations performed at finite chemical potential. Several assumptions can be checked within this comparison, e.g., whether some features of the convergence radius or peaks in thermodynamic quantities are signals for a critical endpoint or just artifacts of the approximation. We will focus on the Taylor expansion method.

6.1. Taylor expansion

One extrapolation method to finite chemical potentials is based on a Taylor expansion of thermodynamic quantities at zero chemical potential in powers of $\left(\frac{\mu}{T}\right)$. Only the calculation of derivatives w.r.t. $\left(\frac{\mu}{T}\right)$ at zero chemical potential is required. Therefore the coefficients are measurable on the lattice with standard simulation techniques [13].

Most common is the Taylor expansion of the pressure

$$\frac{p(T,\mu)}{T^4} = \sum_{n=0}^{\infty} c_n(T) \left(\frac{\mu}{T}\right)^n \tag{6.1}$$

with the coefficients

$$c_n(T) = \frac{1}{n!} \frac{\partial^n \left(p(T,\mu)/T^4\right)}{\partial \left(\mu/T\right)^n}\bigg|_{\mu=0} . \tag{6.2}$$

Since the pressure is directly related to the grand potential, $p = -\Omega$, it contains all information about the system. Because of the CP symmetry of the QCD action, the QCD partition function is even in μ, i.e., $Z(\mu) = Z(-\mu)$, hence only even powers of $\left(\frac{\mu}{T}\right)$ contribute in the series.

Another quantity that allows for a Taylor expansion whose coefficients can be obtained in lattice simulations is the interaction measure

$$\frac{\epsilon - 3p}{T^4} = \sum_{n=0}^{\infty} \bar{c}_n(T) \left(\frac{\mu}{T}\right)^n . \tag{6.3}$$

The coefficients $\bar{c}_n$ are related to the coefficients of the pressure c_n via

$$\bar{c}_n(T) = T \frac{\partial c_n(T)}{\partial T} \tag{6.4}$$

and require an additional T derivative.

The energy and entropy densities can be expanded as well,

$$\frac{\epsilon}{T^4} = \sum_{n=0}^{\infty} \epsilon_n(T) \left(\frac{\mu}{T}\right)^n \ , \tag{6.5}$$

and

$$\frac{s}{T^3} = \sum_{n=0}^{\infty} s_n(T) \left(\frac{\mu}{T}\right)^n \ . \tag{6.6}$$

The coefficients s_n and ϵ_n can be expressed in terms of the coefficients c_n and $\bar{c}_n$:

$$\epsilon_n = 3c_n(T) + \bar{c}_n(T) \tag{6.7}$$

and

$$s_n = (4-n)c_n(T) + \bar{c}_n(T) \ . \tag{6.8}$$

In general the chemical potentials for the three quark flavors (μ_u, μ_d, μ_s) may be different. Alternatively, one may use chemical potentials for the conserved quantum numbers, i.e., baryon number (B), strangeness (S) and electric charge (Q).

Since we have chosen a 2+1 flavor symmetry breaking pattern in this work we are restricted to $\mu_u = \mu_d$. This still allows for the separation of the coefficients

$$c_n^q(T) = \frac{1}{n!} \frac{\partial^n \left(p(T, \mu_q, \mu_s)/T^4\right)}{\partial \left(\mu_q/T\right)^n}\bigg|_{\mu_q=\mu_s=0} \tag{6.9}$$

and

$$c_n^s(T) = \frac{1}{n!} \frac{\partial^n \left(p(T, \mu_q, \mu_s)/T^4\right)}{\partial \left(\mu_s/T\right)^n}\bigg|_{\mu_q=\mu_s=0} \ . \tag{6.10}$$

We will focus on the coefficients c_n where the derivatives have been calculated for one uniform quark chemical potential $\mu = \mu_q = \frac{1}{3}\mu_B$.

On the lattice, the calculation of the coefficients requires the computation of the μ derivatives of the fermion determinant. The complexity of the expressions required in the calculations rises exponentially with higher orders and methods for automation have been developed [92]. The T-derivative required in the calculation of the $\bar{c}_n$ coefficients is currently performed using a numerical derivative [93]. The error inherent in the numerical derivative adds as an additional error to the results.

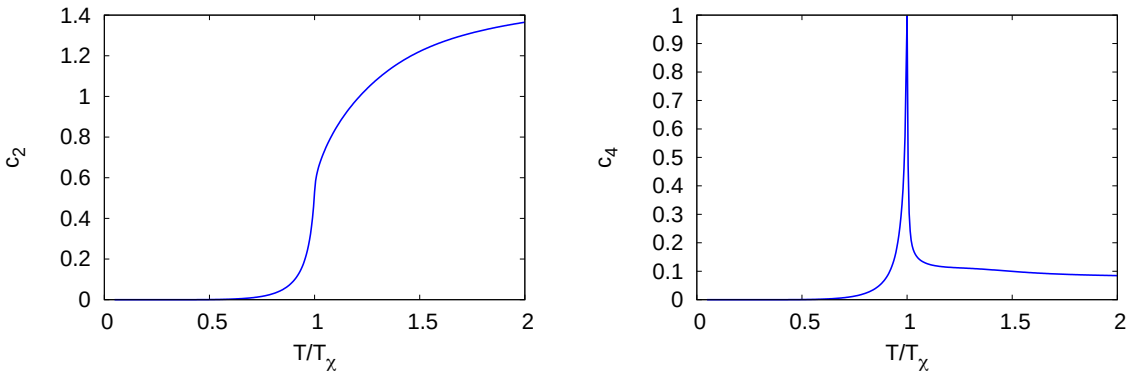

(a) c_2 (b) c_4

Figure 6.1.: Taylor coefficients c_2 to c_6 in the PQM model with logarithmic Polyakov loop potential ($T_0 = 270\,\mathrm{MeV}$).

6.2. Coefficients in the PQM model

In the PQM model the coefficients can be calculated as derivatives of the grand potential w.r.t. μ since $p = -\Omega$. The calculation of the coefficients benefits from the cheaper calculations compared to lattice simulations. Nonetheless, for higher coefficients the expressions for the derivatives become increasingly complex. An analytic calculation of these expressions is theoretically possible but not feasible practically.

Apart from the need to code and check the lengthy expressions for each derivative, the calculation is hampered by the implicit dependencies due to the μ and T-dependence of the fields. Since the equations of motion include an integral that has to be solved numerically, an inversion of these equations is not possible. Even if the explicit derivatives of the grand potential w.r.t. μ are known analytically, the implicit dependencies have to be treated in a numerical derivative.

For the calculation of the derivatives a technique based on *algorithmic differentiation* (AD) has been developed. AD allows for the evaluation of an arbitrary number of derivatives at machine precision, using successive applications of the chain rule on the elementary functions used in the evaluation of the original function. With this novel technique it is possible to calculate derivatives of the grand potential w.r.t. T and μ up to orders $n \sim 40$. This method is presented in App. B.

In the following we will concentrate on the application of this technique to the PQM model using a logarithmic Polyakov loop potential ($T_0 = 270\,\mathrm{MeV}$, $m_\sigma = 600\,\mathrm{MeV}$), including the $U(1)_A$ anomaly.

The high temperature limit of the coefficients can be found analytically in the following

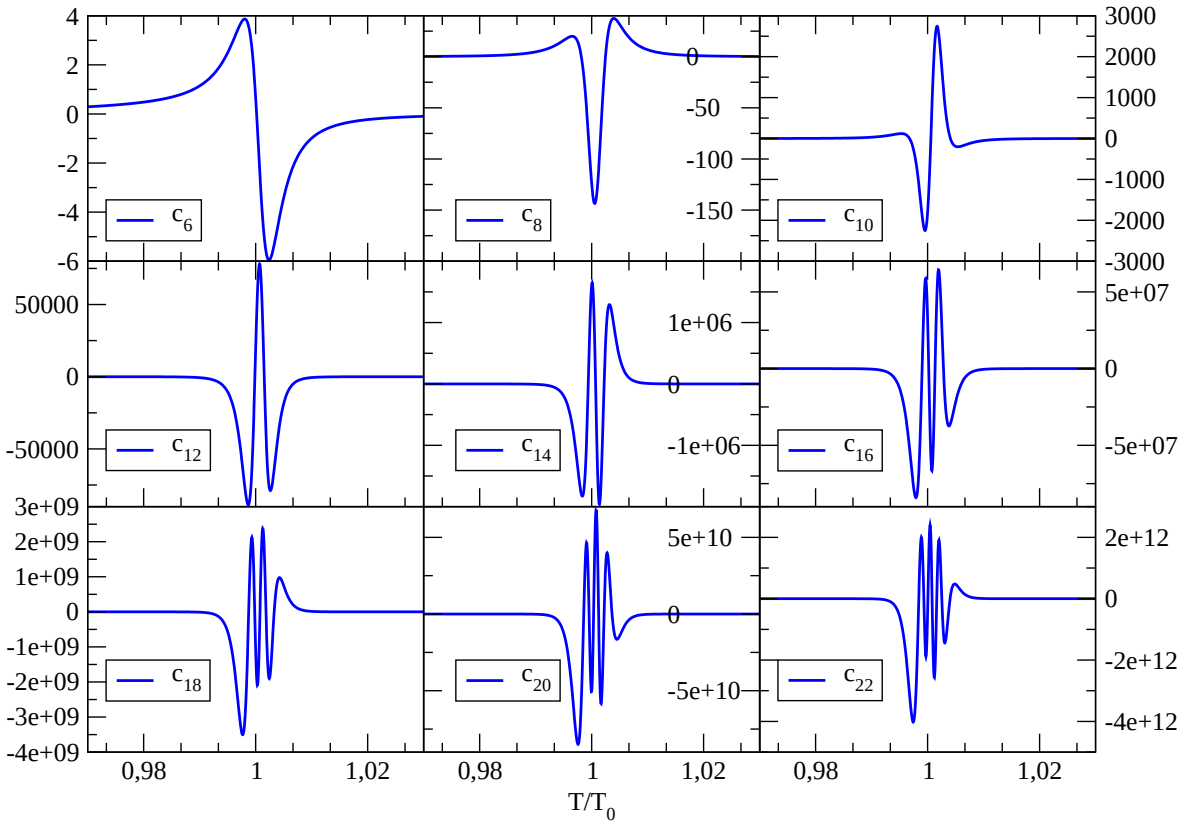

Figure 6.2.: Taylor coefficients c_6 to c_{22} in the PQM model with the logarithmic Polyakov loop potential ($T_0 = 270\,\mathrm{MeV}, m_\sigma = 600\,\mathrm{MeV}$).

way: knowing that the pressure should approach the Stefan-Boltzmann pressure

$$\frac{p_{SB}}{T^4} = 2(N_c^2-1)\frac{\pi^2}{90} + N_c N_F \left(\frac{7\pi^2}{180} + \frac{1}{6}\left(\frac{\mu}{T}\right)^2 + \frac{1}{12\pi^2}\left(\frac{\mu}{T}\right)^4 \right) \tag{6.11}$$

one can easily calculate the coefficients in the high temperature limit

$$\begin{aligned} c_0(T\to\infty) &= \frac{7N_cN_f\pi^2}{180} \ , \\ c_2(T\to\infty) &= \frac{N_cN_f}{6} \ , \\ c_4(T\to\infty) &= \frac{N_cN_f}{12\pi^2} \ , \end{aligned} \tag{6.12}$$

$$c_n(T\to\infty) = 0 \quad \text{for } n>4.$$

The first two coefficients are shown in Figs. 6.1. The coefficient c_0 is simply the pressure at vanishing chemical potential and c_2 is proportional to the quark number density. All coefficients approach the high temperature limit discussed above. The coefficient c_2 is smooth, but c_4 develops a cusp at the transition temperature.

In Fig. 6.2 the coefficients c_6 to c_{22} are only shown in the range $0.95T_\chi$ to $1.05T_\chi$. Outside the displayed range they become very small. While the first coefficients up to c_4 are strictly positive, the higher coefficients develop an increasing number of peaks and roots.

For high temperatures the scale is set by the Matsubara mode $\sim \pi T$ and coefficients of order one are expected for the natural expansion parameter $(\mu/\pi T)$ [94]. Using this expansion parameter, each coefficient has to be divided by an additional factor π^n. Since $\pi^2 \sim 10$ the assumption that the coefficients are of order 1 for the expansion parameter $(\mu/\pi T)$ leads to the estimate

$$c_n \sim \pi^n \approx 10^{n/2} \quad \text{or} \quad c_n \sim 10^{(n\log_{10}\pi)} \quad \text{with } \log_{10}\pi \sim 0.497 \ . \tag{6.13}$$

For the lower coefficients this estimate is rather well fulfilled, but for the higher coefficients we find larger values. For instance, c_{22} should be of the order 10^{11} and a peak with a height of $\sim 2\times 10^{12}$ is found.

The first three coefficients qualitatively agree with published lattice results, see, e.g., [93]. Higher coefficients are currently not available. c_{10} is probably the highest coefficient accessible with current methods [95]. The general features of the lower coefficients are also seen in older lattice calculations with two quark flavors and larger pion masses, e.g. [96, 97].

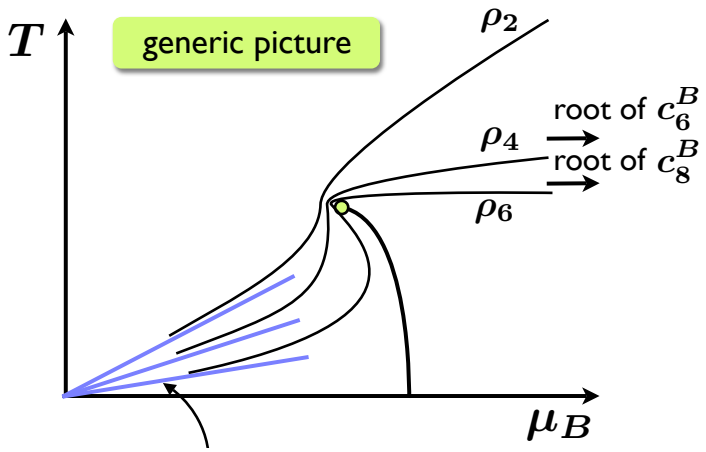

Figure 6.3.: Expected behavior of the convergence radius and influence on the critical point. The lower lines indicate the results obtained in the hadron resonance gas. The arrows mark the position of the first root in the Taylor coefficients. Figure taken from [99].

6.3. Radius of convergence and the critical end point

In each series expansion the radius of convergence limits the range of the expansion's applicability. The radii of convergence of the series expansion can be obtained from the definitions [98]

$$r = \lim_{n\to\infty} r_{2n} = \lim_{n\to\infty} \left| \frac{c_{2n}}{c_{2n+2}} \right|^{1/2} \tag{6.14}$$

and

$$\rho = \lim_{n\to\infty} \rho_{2n} = \lim_{n\to\infty} \left| \frac{c_2}{c_{2n}} \right|^{1/(2n-2)} . \tag{6.15}$$

If the limit $n \to \infty$ is taken both should give the same result, so $\rho = r$. However since n is finite, they may deviate and it is known that (6.14) smoother approaches the limit $n \to \infty$ [92]. We will use both definitions to estimate the effects of the finite value of n. Above a certain value of n, $r_n \approx \rho_n$ is expected. This may be interpreted as a signal for convergence of r_n and ρ_n.

The first order line and the CEP are expected to limit the radius of convergence of the Taylor expansion of the pressure. Therefore it is often argued, that the convergence radius could provide some insight on the location of the critical end point in lattice calculations. This method has been proposed in [30] and used in [32, 92]. One hopes to find a characteristic dip in the convergence radius near the critical point, see Fig. 6.3.

The coefficients have also been calculated in the hadron resonance gas (HRG), which describes the pressure in the broken phase [100, 101]. In this model the pressure differ-

ence is given by

$$\left(\frac{\Delta p}{T^4}\right)_{HRG} = f_B(T)\left(\cosh(\mu_B/T) - 1\right) \ , \tag{6.16}$$

with the function f_B containing information on the resonance mass spectrum. The ratio of the coefficients can be calculated to be [101]

$$\left(r^{(n)}_{HRG}\right)^2 = \left(\frac{c_n}{c_{n+2}}\right) = \frac{(n+2)(n+1)}{9} \ . \tag{6.17}$$

The convergence radius for finite values of n is also shown in the generic view in Fig. 6.3. In the limit $n \to \infty$ the convergence radius diverges

$$r_{HRG} \to \infty \ , \tag{6.18}$$

hence the resonance gas can merely provide a guide for the convergence radius of lattice QCD. For $n < 6$ the convergence radii at high temperatures can be derived from the limits for the coefficients given in Eq. 6.12.

The results for both definitions of the convergence radius are shown in Fig. 6.4. Although the definitions should be equivalent in the limit $n \to \infty$, they differ up to $n = 24$. For the lower coefficients ($n = 2, \ldots, 12$) the radius of convergence changes significantly when higher orders of the expansion are taken into account. The results seem to be numerically very stable. Remember that the higher coefficients are very small for $T \ll T_\chi$ and develop an increasing number of peaks and roots in the vicinity of T_χ that might cause trouble in the calculation of the radii.

In the model calculations the CEP is known exactly and also shown in Fig 6.4. Surprisingly, the CEP lies within the radius of convergence in the calculations for $n \leq 24$. This might be a truncation artifact since the radius of convergence is not yet converged as can be seen when comparing r_{22} and r_{24}. Furthermore the Taylor expansion at $\mu = 0$ might not be able to resolve all effects related to the first-order transition.

A further information contained in the Taylor coefficients is the sign. For $T < T_c$ the Taylor coefficients should be positive [13]. The first root of the Taylor coefficients gives an upper bound on the critical temperature. The first coefficient with a root is c_6. With an increasing number of oscillations this upper bound decreases. In the limit $n \to \infty$ this upper bound should converge to the critical temperature. For the coefficients up to c_{24} the first root of the coefficients decreases to $T \sim 0.98 T_\chi \sim 202\,\mathrm{MeV}$. This is still much larger than the critical temperature $T_c \sim 186\,\mathrm{MeV}$ in this model. If this upper bound converges to the critical temperature, the convergence radius at this upper bound should also provide a good approximation of the critical chemical potential. Since the estimate for T_c is much too large, the determination of μ_c from the radius of convergence at the estimated T_c yields a much too small value.

In Sec. 6.5 we will show, that the position of the peaks and roots of the $2n$-th μ-derivative corresponds to the peak structure in the n-th T-derivative of the pressure. Using this relation, we can show that c_{2n-2} coefficient has an extremum at the first root

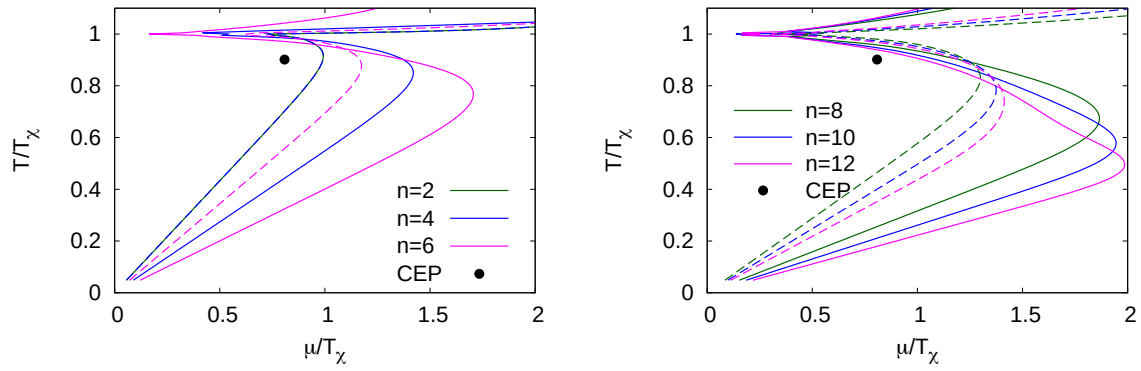

(a) $n = 2, 4, 6$

(b) $n = 8, 10, 12$

(c) n=14,16,18

(d) n=20,22,24

Figure 6.4.: The convergence radii r_n (solid lines) and ρ_n (dashed lines) for $n = 2 \ldots 24$ in the PQM model with logarithmic Polyakov loop potential ($T_0 = 270\,\mathrm{MeV}$).

$T = T_r$ of c_{2n}. This can be understood in the following way: The necessary condition for an extremum in c_{2n-2} is a root in the temperature derivative of c_{2n-2} at $T = T_r$,

$$\frac{d}{dT} c_{2n-2}(T)\bigg|_{T=T_r} = 0 \ . \tag{6.19}$$

For the determination of the position of the root the temperature derivative is identical to the 2nd derivative w.r.t. μ,

$$\frac{d}{dT} c_{2n-2}(T)\bigg|_{T=T_r} = 0 \quad \Leftrightarrow \quad \frac{d^2}{d\mu^2} c_{2n-2}(T)\bigg|_{T=T_r} \propto c_{2n} = 0 \ . \tag{6.20}$$

Up to prefactors the second μ-derivative of c_{2n-2} is equal to c_{2n}. So instead of seeking for the position of the first root in c_{2n} we can search for the maximum in c_{2n-2}. This gives us an information about a higher order Taylor coefficient.

6.4. Thermodynamic quantities

The convergence radius was used to check for signals of a critical end point. Using Taylor expansions it is possible to calculate several thermodynamic quantities at small μ/T. Some of these quantities have already been discussed earlier in this chapter.

The pressure difference is given by

$$\frac{\Delta p(T,\mu)}{T^4} = \frac{p(T,\mu) - p(0,0)}{T^4} = \sum_{n=2,4,\ldots} c_n(T) \left(\frac{\mu}{T}\right)^n \ . \tag{6.21}$$

Using μ-derivatives of the Taylor-expanded pressure, the quark number density

$$\frac{n_q(T,\mu)}{T^3} = \sum_{n=2,4,\ldots} n c_n(T) \left(\frac{\mu}{T}\right)^{n-1} \ , \tag{6.22}$$

and the quark number susceptibility

$$\frac{\chi_q\,(T,\mu)}{T^2} = \sum_{n=2,4,\ldots} n(n-1) c_n(T) \left(\frac{\mu}{T}\right)^{n-2} \tag{6.23}$$

can be evaluated. The quark number susceptibility is a particularly important quantity since it is known to diverge at the critical end point.

The critical end point in the PQM model with logarithmic potential is located at

$$(T_c, \mu_c) \approx (185.7, 166.5)\,\mathrm{MeV} \tag{6.24}$$

(cf. Chap. 4), corresponding to the ratio

$$\frac{\mu}{T} \approx 0.89 < 1 \ . \tag{6.25}$$

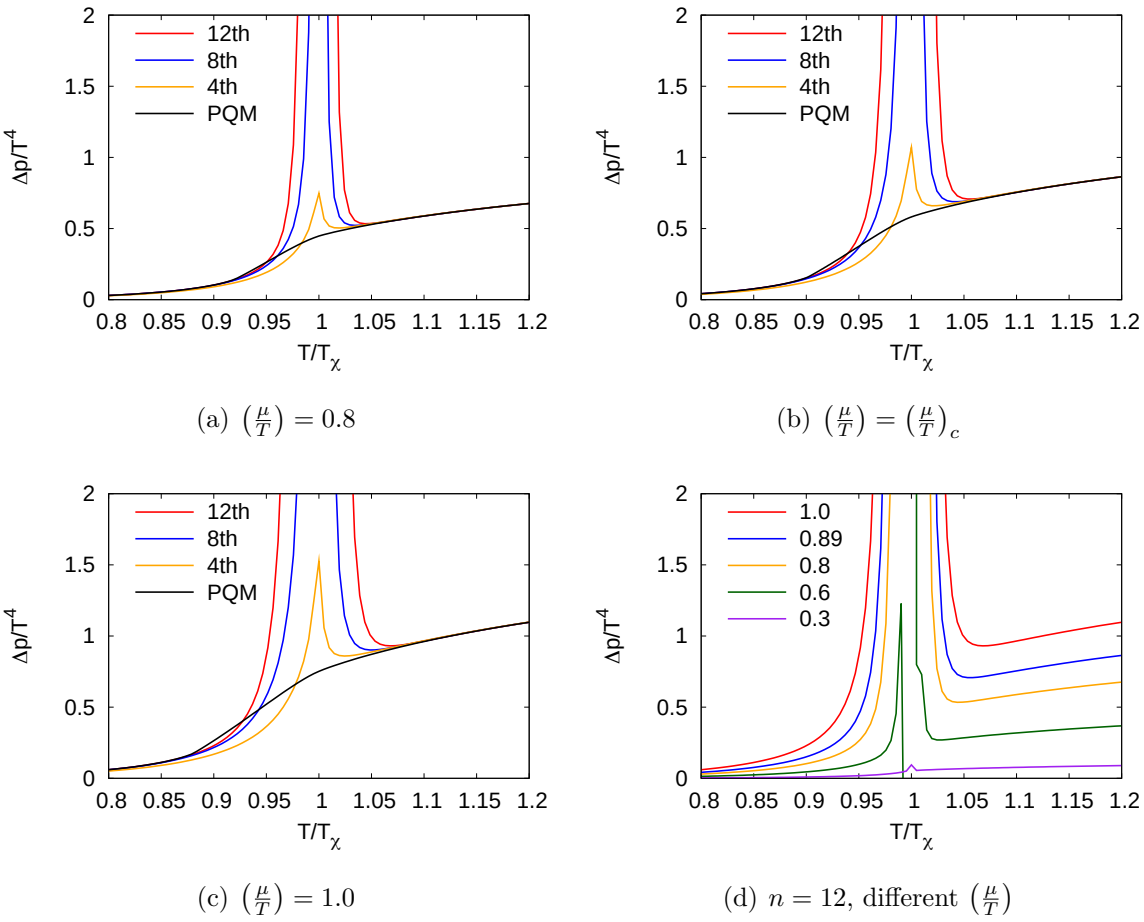

(a) $\left(\frac{\mu}{T}\right) = 0.8$

(b) $\left(\frac{\mu}{T}\right) = \left(\frac{\mu}{T}\right)_c$

(c) $\left(\frac{\mu}{T}\right) = 1.0$

(d) $n = 12$, different $\left(\frac{\mu}{T}\right)$

Figure 6.5.: The pressure difference $\Delta p/T^4$ for different ratios of μ/T and different orders of the Taylor expansion as a function of T. In the lower right plot the Taylor expansion at 12-th order is shown for different values of $\left(\frac{\mu}{T}\right)$.

Since in this model the expansion parameter is smaller than one at the critical end point one can hope that the expansion may indeed work at the critical end point. This allows us to check whether we find signatures directly for $\mu/T = \mu_c/T_c$ which may not be present for other values of μ/T, i.e., $\mu/T < \mu_c/T_c$ and $\mu/T > \mu_c/T_c$. In the following we will compare the quantities calculated using the Taylor expansion and a direct evaluation at finite μ. For the series, different orders of the expansion are used at different ratios of μ/T.

In Fig. 6.5 we show the pressure difference Δp for $\mu/T = 0.8$, μ_c/T_c, 1.0 for $n = 4$, 8, 12 compared with a PQM calculation at finite μ. Further we compare different orders of the expansion for $\mu/T = 1$ in Fig. 6.5(d). The chosen values of n correspond to the simplest lattice calculations with $n = 4$, the currently best lattice calculations $n = 8$, and $n = 12$ to check the influence of even higher orders.

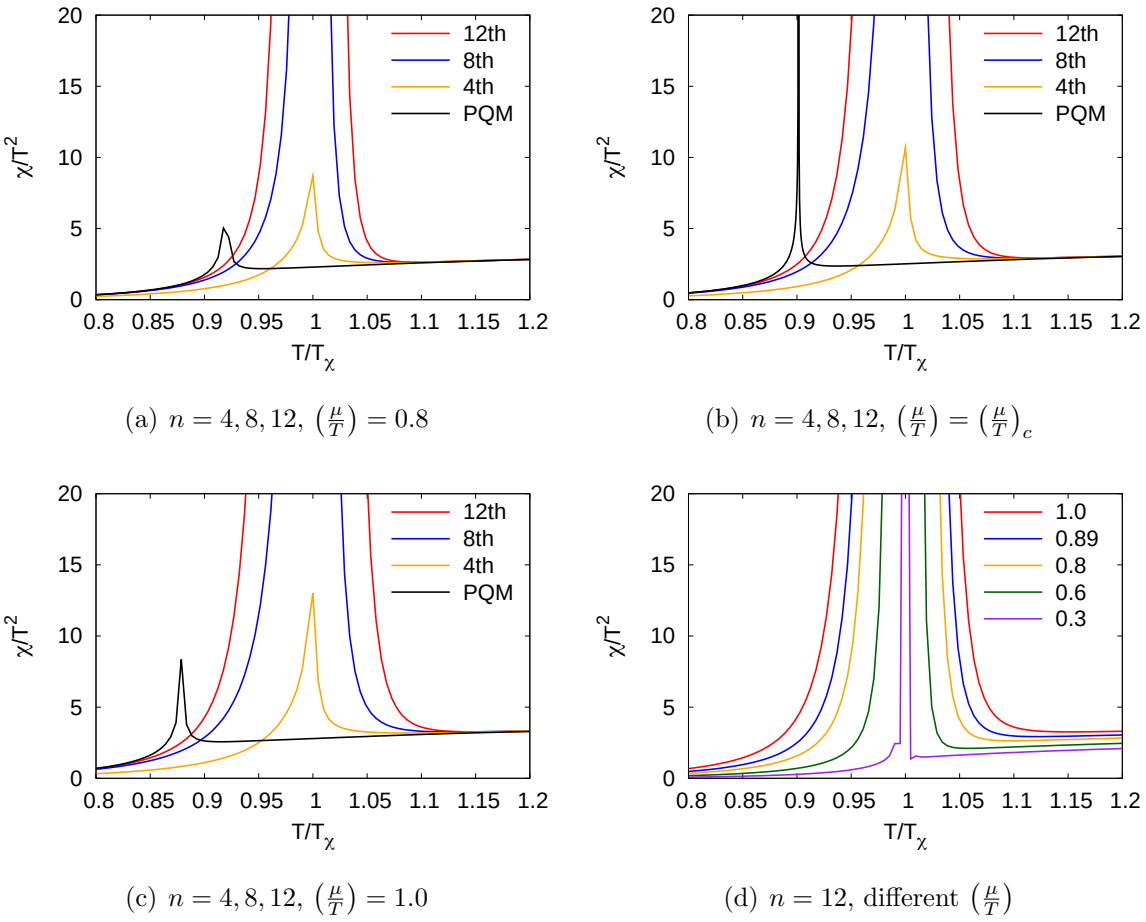

(a) $n = 4, 8, 12$, $\left(\frac{\mu}{T}\right) = 0.8$

(b) $n = 4, 8, 12$, $\left(\frac{\mu}{T}\right) = \left(\frac{\mu}{T}\right)_c$

(c) $n = 4, 8, 12$, $\left(\frac{\mu}{T}\right) = 1.0$

(d) $n = 12$, different $\left(\frac{\mu}{T}\right)$

Figure 6.6.: The quark number susceptibility χ_q/T^2 for different ratios of μ/T and different orders of the Taylor expansion similar to Fig. 6.5.

For all values the exact results can be reproduced for $n \geq 6$ at temperatures sufficiently removed from the phase transition. This is expected because all higher coefficients are small for $n > 6$ and $T \lesssim 0.95T_\chi$ and $T \gtrsim 1.05T_\chi$ (cf. Figs. 6.1 and 6.2). Already at $4th$ order the result obtained with the Taylor expansion shows a peak near T_χ while the exact calculation is smooth. The peak in the expansion becomes more pronounced with higher orders and for higher orders of μ/T. This results from the peak structure of the higher coefficients near T_χ, which become more important for higher values of μ/T. In Fig. 6.5(d) this is demonstrated using different values of μ/T and an expansion up to 12-th order. Even for $\mu/T = 0.3$ a small peak is found which is not seen if the series is truncated earlier, but becomes more pronounced the more higher orders are taken into account.

While the pressure difference is the most simple quantity to study in the Taylor expansion it is not very sensitive to the critical end point. The quark number susceptibility

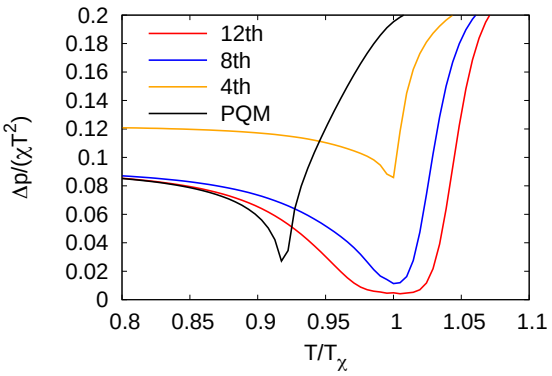

(a) $\left(\frac{\mu}{T}\right) = 0.8$

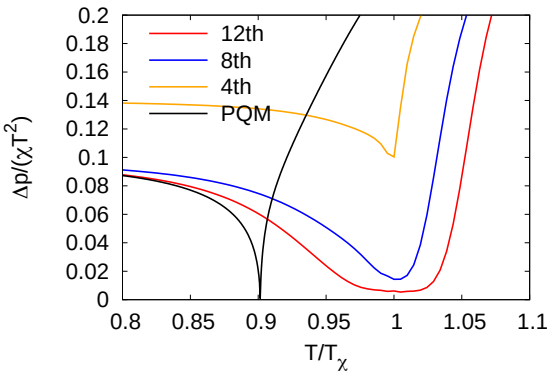

(b) $\left(\frac{\mu}{T}\right) = \left(\frac{\mu}{T}\right)_c$

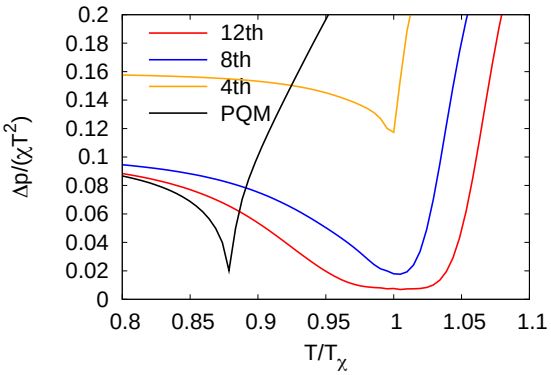

(c) $\left(\frac{\mu}{T}\right) = 1.0$

Figure 6.7.: The size of the fluctuations measured as $\frac{\Delta p}{T^2 \chi_q}$ for different values of $\left(\frac{\mu}{T}\right)$ and different orders of the Taylor expansion.

diverges at the critical end point (cf. Chap. 5) and can be calculated in the Taylor expansion (6.23). Similar to Fig. 6.5, the quark number susceptibility is displayed in Fig. 6.6. In the PQM result a peak with finite height is found for $\mu/T \neq \mu_c/T_c$ as expected for the crossover and first order phase transition at these values of $\left(\frac{\mu}{T}\right)$. At the critical end point the susceptibility diverges. With the Taylor expansion we also find a peak, but it is located at T_χ and the height of the peak grows as more terms in the series are included. The Taylor expansion of the susceptibility fails in describing the height of the peak and its position. At the position of the peak in the PQM calculation the Taylor expansion result is smooth, hence the peak obtained in the Taylor expansion is a pure artifact of the expansion. Since the higher order Taylor coefficients are small at T_c and $\mu_c/T_c < 1$ no additional contribution of even higher orders is expected at T_c.

Another quantity to predict the relative size of the fluctuation has been suggested (cf.

e.g. [101])

$$\frac{\Delta p}{T^2\chi_q} = \frac{1}{2}\left(\frac{\mu}{T}\right)^2 \frac{1 + \frac{c_4}{c_2}\left(\frac{\mu}{T}\right)^2 + \frac{c_6}{c_2}\left(\frac{\mu}{T}\right)^4 + \dots}{1 + 6\frac{c_4}{c_2}\left(\frac{\mu}{T}\right)^2 + 15\frac{c_6}{c_2}\left(\frac{\mu}{T}\right)^4 + \dots} \ . \tag{6.26}$$

This Padé approximant is expected to behave smoother in the region where the coefficients are oscillating. At the critical end point this quantity should vanish. The results of (6.26) are shown for different orders in Fig. 6.7. The PQM model result shows a dip at the phase transition and vanishes at the critical end point. This is expected since the susceptibility diverges at the CEP, but is finite at a crossover and first-order transition while Δp is a smooth function. The Taylor expansions of Δp and χ_q show a peak structure near T_χ and the behavior of $\Delta p/(T^2\chi_q)$ cannot easily be predicted. For all ratios we find a dip with increasing depth for higher expansion orders at $T \sim T_\chi$. Since the Taylor series of the susceptibility and the pressure difference are smooth at the phase transition no sign for a critical end point is expected. At the exact position of the phase transition $\Delta p/(T^2\chi_q)$ shows no noticeable structure.

All quantities considered in this section show the influence of the increasing peak structure in the higher coefficients. When only the lowest coefficients are used the curves may be smooth at small μ/T. Taking into account higher orders will however produce a peak also at rather small μ/T.

Despite these problems the Taylor expansion works reasonably far away from the phase transition, where the higher coefficients become very small.

The details of the peak structure in the coefficients might partly be an artifact of the PQM model with logarithmic potential. The crossover transition is rather fast in this model. With a smoother crossover the peaks are less pronounced, but the general structure like the number of roots is the same. An expansion might work better with a smoother transition. This probably does not affect the finding of the critical end point discussed in the previous section. For a smoother transition at $\mu = 0$ the critical end point is usually located at higher chemical potential.

6.5. Scaling

Near the phase transition it is possible to apply scaling relations. They may provide some further insight since it becomes possible to relate temperature derivatives with higher μ-derivatives. The lower T-derivatives might be more easier accessible.

Using the scaling assumption (cf. e.g. [83, 102]) for the pressure in the vicinity of the pseudocritical phase transition at $\mu = 0$

$$p(T,\mu) - p(T_\chi, 0) \propto t^\alpha \tag{6.27}$$

with the scaling variable

$$t = \frac{T - T_\chi}{T_\chi} + A\left(\frac{\mu}{T_\chi}\right)^2 \ , \tag{6.28}$$

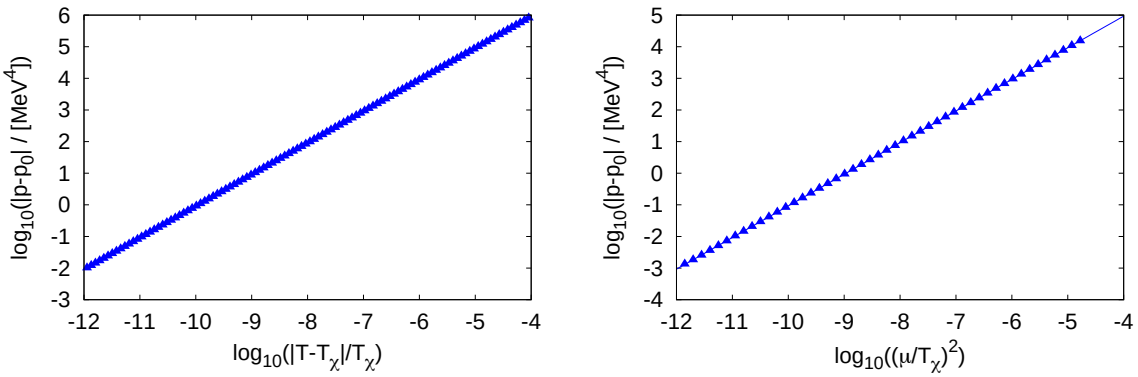

(a) T-direction (b) μ-direction

Figure 6.8.: The logarithm of the deviation from the critical value at $\mu = 0$ as function of $\log_{10}(t)$. The left panel shows a path for $\mu = 0$ in the T-direction. The right panel shows the path for $T = T_\chi$ towards finite μ.

it is possible to relate T and μ derivatives. A is a proportionally constant. The scaling of the pressure at $\mu = 0$ is shown in Fig. 6.8 for the T and the μ direction. Both curves show the same slope and differ only by an offset which is due to the constant A in the scaling variable t. The solid lines show a linear fit to the data in the log-log plot. In this fit we found the values

$$\alpha_T = 1.001 \pm 0.002 \ , \quad \alpha_\mu = 1.000 \pm 0.002$$

in T and μ direction, respectively. They nicely agree which each other and are in agreement with a value of one. The constant A results in an offset in the logarithmic plots between the scaling in T and μ-direction. A can be calculated to be $\log_{10}(A)$ and we find $\log_{10}(A) \sim -1$ corresponding to $A \sim 1/10$. If one replaces $A(\mu/T)^2$ in Eq. 6.28 with the natural scaling variable $\left(\frac{\mu}{\pi T}\right)^2$ this corresponds to $A = \pi^{-2} \sim 1/10$ in agreement with the observed offset.

From this scaling point of view the $2n$-th derivative w.r.t. μ looks like the n-th derivative w.r.t. to T. This is demonstrated for some derivatives in Fig. 6.9. We have defined the coefficients

$$d_n(T) = \frac{1}{2n!}\frac{1}{T^4}\frac{\partial^n \left(p(T,\mu)\right)}{\partial T^n}\bigg|_{\mu=0} \ . \tag{6.29}$$

with the factorial $2n!$ to compensate the factorial in the c_{2n} coefficient for comparison.

In Fig. 6.9 the coefficients d_n are compared with the c_{2n} coefficients for $n = 1, 2, 5, 10$. Note that the coefficients have been scaled to be of order one for better comparison. The qualitative agreement is rather good. The positions of the peaks and roots is nearly perfectly reproduced. So the peak structure might be explored using T-derivatives instead of μ-derivatives, as already mentioned in Sec. 6.3.

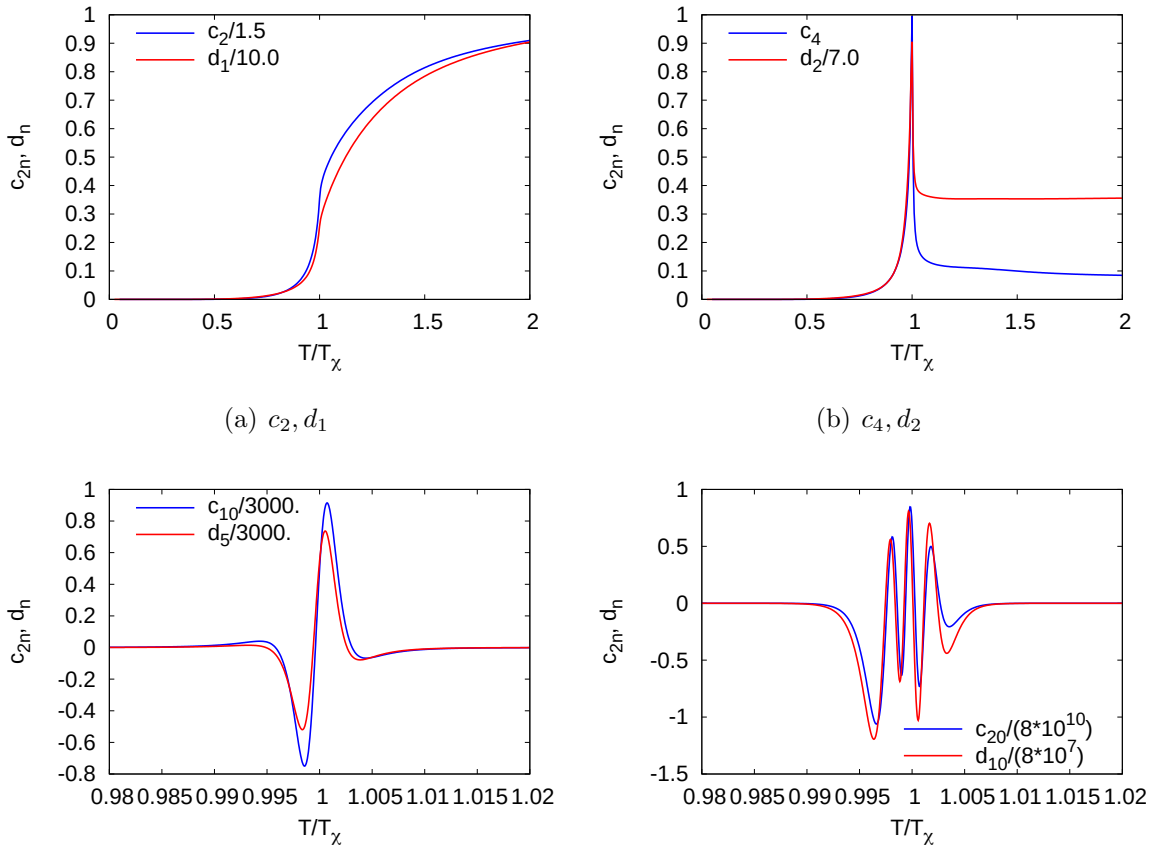

(a) c_2, d_1

(b) c_4, d_2

(c) c_{10}, d_5

(d) c_{20}, d_{10}

Figure 6.9.: Comparison of the coefficients for the n-th temperature derivative d_n with the $2n$-th μ-derivative c_{2n} for various values of n as a function of temperature.

7. Summary

In this work we have investigated several properties of strongly interacting matter, in particular the chiral symmetry restoration and deconfinement transition. Even today the quantitative as well as the qualitative knowledge of the phase diagram of strongly interacting matter is very limited. Currently, studies in effective models are the only way to explore the phase diagram at arbitrary chemical potential, where lattice calculations, although a valuable tool at vanishing chemical potential, are hampered by the fermion sign problem.

On the scales relevant for the phase transition, the chiral symmetry of Quantum Chromodynamics (QCD) is most suitably described using mesons and the three light quarks (up, down, strange) as degrees of freedom. This is accomplished by the use of a linear sigma model (LσM) with additional quark degrees of freedom. The effects of confinement are added by coupling the Polyakov loop to the fermions, resulting in the Polyakov-Quark-Meson (PQM) model. This model allows for a more realistic description of the equation of state of strongly interacting matter.

For the investigation of the chiral symmetry restoration in Chapter 3 the strange and non-strange condensates serve as approximate order parameters. The chiral symmetry restoration can also be observed in the in-medium meson masses. In the applied mean-field approximation, negative squared meson masses do not occur in the broken phase, unlike in the LσM without quarks, and low-energy theorems like the Goldstone theorem in the chiral limit or the Ward identities are satisfied also at finite temperature and density.

At the physical mass point, i.e., for realistic pion and kaon masses, a critical end point was observed in the phase diagram for values of the sigma mass in between $m_\sigma = 600 \ldots 800$ MeV. For larger values of m_σ the critical end point disappears. The chiral critical surface has been calculated for $m_\sigma = 800\,\mathrm{MeV}$. With and without $U(1)_A$ anomaly the standard scenario with a bending of the surface towards higher masses was observed. A strong influence of the $U(1)_A$ anomaly was found in the region of low pion and kaon mass, while for higher kaon masses the modifications due to the $U(1)_A$ anomaly become negligible again. We further checked the influence of the variations of m_σ. For increasing sigma masses the surface becomes steeper at smaller chemical potentials and the bending towards higher masses sets in at higher chemical potentials. A non-standard scenario proposed by de Forcrand and Philipsen is not observed in the considered mass range $m_\sigma = 500 \ldots 900\,\mathrm{MeV}$. This non-standard scenario might be realized in the model when instanton screening is taken into account, resulting in a temperature and density-dependent strength of the $U(1)_A$ symmetry breaking.

The LσM with quarks does not incorporate confinement. In Chapter 4, the Polyakov loop was introduced as an order parameter for confinement in the pure gauge limit. Three different choices for the Polyakov loop potential in pure gauge have been presented. This allows us to investigate the deconfinement and chiral symmetry restoration in the PQM model with a realistic $2+1$ flavor symmetry breaking pattern for the first time.

The suppression of the fermionic degrees of freedom due to confinement also affects the chiral symmetry restoration. At zero chemical potential a higher pseudocritical temperature and a more rapid crossover is observed than in the model without Polyakov loop. These observations hold for several combinations of the Polyakov loop potentials and parameters for the underlying LσM. Current lattice data suggest that the deconfinement and chiral phase transition coincide within a few MeV at vanishing chemical potential, hence for the studies at finite chemical potential we focussed on combinations where this coincidence is realized. At finite chemical potential, we found a separation of the chiral and deconfinement transitions at some finite chemical potential for all Polyakov loop potentials. This hints at a quarkyonic phase in the PQM model. Whether this is a shortcoming of the chosen Polyakov loop potentials which are not really adapted to effects at finite chemical potential is still under investigation. Notably, the chiral first-order transition at small chemical potential is completely unaffected by the Polyakov loop. The chiral critical end point moves to lower chemical potentials and higher temperatures with the Polyakov loop. Its position depends on the Polyakov loop potential as well as on the details of the underlying LσM.

In Chapter 5, several thermodynamic properties of strongly interacting matter have been analyzed in the framework of the models with and without Polyakov loop. Including the Polyakov loop dynamics, a reasonable description of current lattice data, e.g., the pressure or the interaction measure is achieved. The quark number density nicely shows the suppression of the quarks by the Polyakov loop as well as the possible quarkyonic phase. Furthermore, the size of the critical region, relevant for an experimental observation of the critical end point, shrinks in the PQM model. The elongated shape along the phase transition can be explained by different values of the critical exponent for the quark number susceptibility for a path parallel to the phase transition. Values for the different directions have been calculated explicitly.

In Chapter 6 we presented results for the Taylor expansion method obtained with a novel method based on algorithmic differentiation. Using this method, we were able to calculate the Taylor coefficients up to c_{24} for the first time. This is far beyond current lattice calculations, which are currently limited to c_8. Since the grand potential of the PQM model can also be evaluated directly at finite chemical potential, a comparison between the extrapolated results and a direct calculation at finite chemical potential could be carried out. It turned out that the Taylor expansion results fail to reproduce the characteristic structures of the critical end point, e.g., the peak in the quark number susceptibility and a peak near the pseudocritical temperature is observed instead. Furthermore, the convergence radii have been calculated to estimate the position of the critical end point. While it is expected that critical end point should limit the conver-

gence radius, we found it to be still inside the convergence radius up to all calculated orders. The critical temperature is overestimated significantly and correspondingly, the location of the critical end point is found at an unrealistically low chemical potential. Calculating even higher orders or using an $1/n$ extrapolation for the convergence radii might improve this results. However, the higher orders now available in the model are clearly out of reach for current and near-future lattice calculations. Due to these results, the locations of the critical point determined using the Taylor expansion method in the literature (e.g., [32]) become questionable.

The developments achieved in this work allow for numerous further studies. While several properties of the chiral symmetry restoration, e.g., the chiral critical surface, have been studied in the LσM without confinement effects, it is still unknown how they are influenced by the Polyakov loop in the PQM model. The effects of instanton screening, resulting in a weaker $U(1)_A$ symmetry breaking at finite temperatures and densities, should be considered as well. The inclusion of vector-vector-interactions in the model has been shown to open the possibility for a non-standard scenario of the chiral critical surface [22].

In the PQM model, the situation at finite chemical potential remains an open issue. The Polyakov loop potentials in particular are constructed solely in the pure gauge limit and leave room for improvements to account for finite densities and dynamical quarks. The power of the method developed to calculate higher derivatives has just been revealed. The calculation of the higher order Taylor coefficients is just one example, that demonstrates the abilities of this method. The exact treatment of the implicit dependencies is useful for many fields in physics and not restricted to effective models for strongly interacting matter at all. A first logical extension is of course a more detailed study of the convergence radii and possibilities to estimate the critical end point from the Taylor coefficients. Here the study of different parameters, e.g., with critical end points located in different regions of the phase diagram, will allow for an improved understanding of the limitations of the Taylor expansion method used in lattice simulations.

The algorithmic differentiation might also be used in connection with Renormalization Group (RG) studies, which take fluctuations into account. Calculations in the quark-meson model with two flavors [50, 103] show that the influence of the mesonic fluctuations, which are neglected in the mean-field approach, may crucially modify certain properties, in particular near the critical end point, e.g., the size of the critical region. RG studies with three quark-flavors have not yet been performed at finite temperature and density. A modification of the chiral critical surface is expected, since the two-flavor RG calculation correctly predicts a second-order transition in the chiral limit [50] and we can therefore expect to find a critical strange quark mass in a RG calculation for three flavors. At realistic strange quark masses the influence of the additional strange quark on the phase diagram turned out to be weak in our studies. The mesonic fluctuations might lead to a stronger modification due to the additional strangeness degree of freedom. The inclusion of the Polyakov loop in these RG studies is a completely

unknown field. The suppression of the quark number density and correspondingly also the fermionic fluctuations will certainly be influenced significantly. Finally, since fluctuations are always present near phase boundaries, these RG studies should allow for a more realistic description of the phase diagram of strongly interacting matter.

With improvements in model calculations, as well as lattice simulations, which may serve as a guide for model studies at vanishing chemical potential, more reliable predictions for the QCD phase diagram will be in reach, which can be tested by the upcoming experiments at the LHC and the FAIR facility. These will allow for a deeper understanding of the fundamental properties of strongly interacting matter at finite temperature and density. The field will certainly stay one of the most fascinating and lively ones in modern particle physics.

A. Parameters and formulas of the LσM

A.1. Parameter fits

In this appendix several parameter sets for the linear sigma model (LσM) with three quark flavors are collected.

As experimental input we have chosen the low-lying pseudoscalar meson mass spectrum (m_π, m_K, m_η), the constituent quark mass m_q and the pion and kaon decay constants. To be more precise, for the fit with anomaly ($c \neq 0$) the sum $m_\eta^2 + m_{\eta'}^2$ is chosen as input, while for $c = 0$ the m_η has not been used as input. The experimental values, taken from Ref. [54], are listed in the last line of Tab. A.2 for comparison. Since the chiral σ-particle is a broad resonance, its mass is not known precisely. We therefore have used different input values for m_σ in the range of $400 - 1000$ MeV and refitted the remaining parameters of the model accordingly. It is remarkable that larger sigma meson masses cannot be produced since m_σ as a function of the quartic coupling λ_1 saturates around 1100 MeV.

In Tab. A.2 all resulting meson masses are listed. The upper block contains the fit without anomaly and the lower block the fit including the anomaly. With the exception of the pseudoscalar masses in the first four/five columns in the table, all other (scalar) masses and the mixing angles are predictions of the model.

In Tab. A.1 the obtained values for the six mesonic model parameters of the LσM with and without explicit $U(1)_A$ symmetry breaking are summarized. The Yukawa coupling is always kept fixed to $g \sim 6.5$, corresponding to a constituent quark mass of $m_q = 300$ MeV. The decay constants, $f_\pi = 92.4$ MeV and $f_K = 113$ MeV, are also kept constant for all fits. Without $U(1)_A$ symmetry breaking the quartic coupling λ_1 is always negative while it is positive if the symmetry is broken. It is interesting to realize that for small values of m_σ and with $U(1)_A$ anomaly the mass parameter m^2 changes its sign and becomes positive when fitted to realistic masses. As a consequence, spontaneous symmetry breaking is lost in the chiral limit and all condensates will vanish in this limit. This happens for $m_\sigma \leq 600$ MeV. Even without anomaly ($c = 0$) a similar phenomenon can be seen. In this case, the masses are smaller when this effect appears, i.e. $m_\sigma \leq 400$ MeV. This is the motivation for our choice of $m_\sigma = 800$ MeV. For this parameter set we can investigate the mass sensitivity of the chiral phase transition over arbitrary explicit symmetry breaking values including the chiral limit. The choice $m_\sigma = 800$ MeV for the parameter fit without anomaly is also in agreement with [49] ($m_\sigma = 600$ MeV is a misprint in this reference). For larger m_σ values the quartic coupling λ_1 increases significantly.

m_σ[MeV]	c[MeV]	λ_1	m^2[MeV^2]	λ_2	h_x[MeV^3]	h_y[MeV^3]
400	0	-24.55	$+(309.41)^2$	82.47	$(120.73)^3$	$(336.41)^3$
500	0	-21.24	$+(194.82)^2$	82.47	$(120.73)^3$	$(336.41)^3$
600	0	-17.01	$-(189.85)^2$	82.47	$(120.73)^3$	$(336.41)^3$
700	0	-11.61	$-(360.91)^2$	82.47	$(120.73)^3$	$(336.41)^3$
800	0	-4.55	$-(503.55)^2$	82.47	$(120.73)^3$	$(336.41)^3$
900	0	5.56	$-(655.82)^2$	82.47	$(120.73)^3$	$(336.41)^3$
1000	0	24.22	$-(869.50)^2$	82.47	$(120.73)^3$	$(336.41)^3$
400	4807.84	-5.90	$+(494.75)^2$	46.48	$(120.73)^3$	$(336.41)^3$
500	4807.84	-2.70	$+(434.56)^2$	46.48	$(120.73)^3$	$(336.41)^3$
600	4807.84	1.40	$+(342.52)^2$	46.48	$(120.73)^3$	$(336.41)^3$
700	4807.84	6.62	$+(161.98)^2$	46.48	$(120.73)^3$	$(336.41)^3$
800	4807.84	13.49	$-(306.26)^2$	46.48	$(120.73)^3$	$(336.41)^3$
900	4807.84	23.65	$-(520.80)^2$	46.48	$(120.73)^3$	$(336.41)^3$
1000	4807.84	45.43	$-(807.16)^2$	46.48	$(120.73)^3$	$(336.41)^3$

Table A.1.: Different parameter sets for various m_σ with ($c \neq 0$) and without ($c = 0$) $U(1)_A$ anomaly.

m_σ	m_π	m_K	$m_{\eta'}$	m_η	θ_P	m_{a_0}	m_κ	m_{f_0}	θ_S
400	138	496	138.0	634.8	35.3	850.4	1124.3	1257.3	16.7
500	138	496	138.0	634.8	35.3	850.4	1124.3	1267.4	18.7
600	138	496	138.0	634.8	35.3	850.4	1124.3	1282.3	21.5
700	138	496	138.0	634.8	35.3	850.4	1124.3	1304.9	25.5
800	138	496	138.0	634.8	35.3	850.4	1124.3	1341.4	31.3
900	138	496	138.0	634.8	35.3	850.4	1124.3	1408.0	40.0
1000	138	496	138.0	634.8	35.3	850.4	1124.3	1563.4	53.2
400	138	496	963.0	539.0	−5.0	1028.7	1124.3	1198.4	14.9
500	138	496	963.0	539.0	−5.0	1028.7	1124.3	1207.5	16.9
600	138	496	963.0	539.0	−5.0	1028.7	1124.3	1221.1	19.9
700	138	496	963.0	539.0	−5.0	1028.7	1124.3	1242.3	24.2
800	138	496	963.0	539.0	−5.0	1028.7	1124.3	1278.0	30.7
900	138	496	963.0	539.0	−5.0	1028.7	1124.3	1348.0	40.9
1000	138	496	963.0	539.0	−5.0	1028.7	1124.3	1545.6	57.1
400-1200	138.0	496	957.8	547.5		984.7	1414	1200-1500	

Table A.2.: Meson masses and mixing angles in the vacuum for different sets of parameters. The first six columns are input while the remaining columns are predictions. Upper block: without ($c = 0$) $U(1)_A$ anomaly, lower block: with $U(1)_A$ anomaly. Last line: experimental values from the PDG [54].

A.2. Meson masses

The scalar ($J^P = 0^+$) and pseudoscalar ($J^P = 0^-$) meson masses are defined by the second derivative w.r.t. the corresponding scalar and pseudoscalar fields $\varphi_{s,a} = \sigma_a$ and $\varphi_{p,a} = \pi_a$ ($a = 0, \ldots, 8$) of the grand canonical potential $\Omega(T, \mu_f)$, Eq. (3.10), evaluated at its minimum. The minimum is given by vanishing expectation values of all scalar and pseudoscalar fields but only two of them, $\bar{\sigma}_x$ and $\bar{\sigma}_y$, are nonzero.

$$m^2_{i,ab} = \left.\frac{\partial^2 \Omega(T,\mu_f)}{\partial\varphi_{i,a}\partial\varphi_{i,b}}\right|_{\min} \quad ; \quad i = s, p \ . \tag{A.1}$$

In the vacuum, the contribution from the quark potential vanishes, hence only the mesonic part of the potential determines the mass matrix completely. The squared mass matrix is diagonal and due to isospin $SU(2)$ symmetry several matrix entries are degenerate. We begin with the scalar sector corresponding to $i = S$. The squared mass of the a_0 meson is given by the (11) element which is degenerate with the (22) and (33) elements. Similar, the squared κ meson mass is given by the (44) element which is also degenerate with the (55), (66) and (77) elements. The σ and $f_0(1370)$ meson masses are obtained by diagonalizing the (00)-(88) sector of the mass matrix, introducing a mixing angle θ_S. Explicitly, the squared masses for scalar sector, formulated in the non-strange-strange basis, are

$$m^2_{a_0} = m^2 + \lambda_1(\bar{\sigma}_x^2 + \bar{\sigma}_y^2) + \frac{3\lambda_2}{2}\bar{\sigma}_x^2 + \frac{\sqrt{2}c}{2}\bar{\sigma}_y \ , \tag{A.2}$$

$$m^2_{\kappa} = m^2 + \lambda_1(\bar{\sigma}_x^2 + \bar{\sigma}_y^2) + \frac{\lambda_2}{2}\left(\bar{\sigma}_x^2 + \sqrt{2}\bar{\sigma}_x\bar{\sigma}_y + 2\bar{\sigma}_y^2\right) + \frac{c}{2}\bar{\sigma}_x \ , \tag{A.3}$$

$$m^2_{\sigma} = m^2_{s,00}\cos^2\theta_S + m^2_{s,88}\sin^2\theta_S + 2m^2_{s,08}\sin\theta_S\cos\theta_S \ , \tag{A.4}$$

$$m^2_{f_0} = m^2_{s,00}\sin^2\theta_S + m^2_{s,88}\cos^2\theta_S - 2m^2_{s,08}\sin\theta_S\cos\theta_S \tag{A.5}$$

with

$$\begin{aligned}
m^2_{s,00} &= m^2 + \frac{\lambda_1}{3}(7\bar{\sigma}_x^2 + 4\sqrt{2}\bar{\sigma}_x\bar{\sigma}_y + 5\bar{\sigma}_y^2) + \lambda_2(\bar{\sigma}_x^2 + \bar{\sigma}_y^2) - \frac{\sqrt{2}c}{3}(\sqrt{2}\bar{\sigma}_x + \bar{\sigma}_y) \ , \\
m^2_{s,88} &= m^2 + \frac{\lambda_1}{3}(5\bar{\sigma}_x^2 - 4\sqrt{2}\bar{\sigma}_x\bar{\sigma}_y + 7\bar{\sigma}_y^2) + \lambda_2(\frac{\bar{\sigma}_x^2}{2} + 2\bar{\sigma}_y^2) + \frac{\sqrt{2}c}{3}\left(\sqrt{2}\bar{\sigma}_x - \frac{\bar{\sigma}_y}{2}\right) \ , \\
m^2_{s,08} &= \frac{2\lambda_1}{3}\left(\sqrt{2}\bar{\sigma}_x^2 - \bar{\sigma}_x\bar{\sigma}_y - \sqrt{2}\bar{\sigma}_y^2\right) + \sqrt{2}\lambda_2\left(\frac{\bar{\sigma}_x^2}{2} - \bar{\sigma}_y^2\right) + \frac{c}{3\sqrt{2}}\left(\bar{\sigma}_x - \sqrt{2}\bar{\sigma}_y\right) \ .
\end{aligned}$$

The situation for the pseudoscalar sector ($i = P$) is completely analogous: the squared pion mass is identified with the (11) element and the squared kaon mass with the (44) element of the pseudoscalar mass matrix. Similar to the scalar case, the η and η' mass

are obtained by diagonalizing the (00)-(88) sector and accordingly a pseudoscalar mixing angle θ_P is introduced. Explicitly, the squared masses for the pseudoscalar sector are

$$m_\pi^2 = m^2 + \lambda_1(\bar{\sigma}_x^2 + \bar{\sigma}_y^2) + \frac{\lambda_2}{2}\bar{\sigma}_x^2 - \frac{\sqrt{2}c}{2}\bar{\sigma}_y \tag{A.6}$$

$$m_K^2 = m^2 + \lambda_1(\bar{\sigma}_x^2 + \bar{\sigma}_y^2) + \frac{\lambda_2}{2}\left(\bar{\sigma}_x^2 - \sqrt{2}\bar{\sigma}_x\bar{\sigma}_y + 2\bar{\sigma}_y^2\right) - \frac{c}{2}\bar{\sigma}_x \tag{A.7}$$

$$m_{\eta'}^2 = m_{p,00}^2 \cos^2\theta_P + m_{p,88}^2 \sin^2\theta_P + 2m_{p,08}^2 \sin\theta_P \cos\theta_P \tag{A.8}$$

$$m_\eta^2 = m_{p,00}^2 \sin^2\theta_P + m_{p,88}^2 \cos^2\theta_P - 2m_{p,08}^2 \sin\theta_P \cos\theta_P \tag{A.9}$$

with

$$\begin{aligned}
m_{p,00}^2 &= m^2 + \lambda_1(\bar{\sigma}_x^2 + \bar{\sigma}_y^2) + \frac{\lambda_2}{3}(\bar{\sigma}_x^2 + \bar{\sigma}_y^2) + \frac{c}{3}(2\bar{\sigma}_x + \sqrt{2}\bar{\sigma}_y) \\
m_{p,88}^2 &= m^2 + \lambda_1(\bar{\sigma}_x^2 + \bar{\sigma}_y^2) + \frac{\lambda_2}{6}(\bar{\sigma}_x^2 + 4\bar{\sigma}_y^2) - \frac{c}{6}(4\bar{\sigma}_x - \sqrt{2}\bar{\sigma}_y) \\
m_{p,08}^2 &= \frac{\sqrt{2}\lambda_2}{6}(\bar{\sigma}_x^2 - 2\bar{\sigma}_y^2) - \frac{c}{6}(\sqrt{2}\bar{\sigma}_x - 2\bar{\sigma}_y)
\end{aligned}$$

Both mixing angles are given by

$$\tan 2\Theta_i = \frac{2m_{i,08}^2}{m_{i,00}^2 - m_{i,88}^2} \ , \ i = S, P \ . \tag{A.10}$$

In the medium the meson masses are further modified by the quark contribution (3.7). In order to evaluate the second derivate (A.1) for the quark contribution the complete dependence of all scalar and pseudoscalar meson fields in the quark masses has to be taken into account, cf. Eq. (3.4). The resulting quark mass matrix can be diagonalized. Finally, we obtain the expression

$$\begin{aligned}
\left.\frac{\partial^2\Omega_{\bar{q}q}(T,\mu_f)}{\partial\varphi_{i,\alpha}\partial\varphi_{i,\beta}}\right|_{\min} &= \nu_c \sum_{f=q,s}\int\frac{d^3p}{(2\pi)^3}\frac{1}{2E_{q,f}} \\
&\left[(n_{q,f} + n_{\bar{q},f})\left(m_{f,\alpha\beta}^2 - \frac{m_{f,\alpha}^2 m_{f,\beta}^2}{2E_{q,f}^2}\right) - \frac{(b_{q,f} + b_{\bar{q},f})}{2E_{q,f}T} m_{f,\alpha}^2 m_{f,\beta}^2\right]
\end{aligned} \tag{A.11}$$

where we have introduced the short hand notation $m_{f,a}^2 \equiv \partial m_f^2/\partial\varphi_{i,a}$ for the quark mass derivative w.r.t. the meson fields $\varphi_{i,a}$, the quark function

$$b_{q,f}(T,\mu_f) = n_{q,f}(T,\mu_f)(1 - n_{q,f}(T,\mu_f)) \tag{A.12}$$

		$m^2_{l,\alpha}m^2_{l,\beta}/g^4$	$m^2_{l,\alpha\beta}/g^2$	$m^2_{s,\alpha}m^2_{s,\beta}/g^4$	$m^2_{s,\alpha\beta}/g^2$
$\bar{\sigma}_0$	$\bar{\sigma}_0$	$\frac{1}{3}\bar{\sigma}_x^2$	$\frac{2}{3}$	$\frac{1}{3}\bar{\sigma}_y^2$	$\frac{1}{3}$
$\bar{\sigma}_1$	$\bar{\sigma}_1$	$\frac{1}{2}\bar{\sigma}_x^2$	1	0	0
$\bar{\sigma}_4$	$\bar{\sigma}_4$	0	$\bar{\sigma}_x\frac{\bar{\sigma}_x+\sqrt{2}\bar{\sigma}_y}{\bar{\sigma}_x^2-2\bar{\sigma}_y^2}$	0	$\bar{\sigma}_y\frac{\sqrt{2}\bar{\sigma}_x+2\bar{\sigma}_y}{2\bar{\sigma}_y^2-\bar{\sigma}_x^2}$
$\bar{\sigma}_8$	$\bar{\sigma}_8$	$\frac{1}{6}\bar{\sigma}_x^2$	$\frac{1}{3}$	$\frac{2}{3}\bar{\sigma}_y^2$	$\frac{2}{3}$
$\bar{\sigma}_0$	$\bar{\sigma}_8$	$\frac{\sqrt{2}}{6}\bar{\sigma}_x^2$	$\frac{\sqrt{2}}{3}$	$-\frac{\sqrt{2}}{3}\bar{\sigma}_y^2$	$-\frac{\sqrt{2}}{3}$
π_0	π_0	0	$\frac{2}{3}$	0	$\frac{1}{3}$
π_1	π_1	0	1	0	0
π_4	π_4	0	$\bar{\sigma}_x\frac{\bar{\sigma}_x-\sqrt{2}\bar{\sigma}_y}{\bar{\sigma}_x^2-2\bar{\sigma}_y^2}$	0	$\bar{\sigma}_y\frac{\sqrt{2}\bar{\sigma}_x-2\bar{\sigma}_y}{\bar{\sigma}_x^2-2\bar{\sigma}_y^2}$
π_8	π_8	0	$\frac{1}{3}$	0	$\frac{2}{3}$
π_0	π_8	0	$\frac{\sqrt{2}}{3}$	0	$-\frac{\sqrt{2}}{3}$

Table A.3.: Squared quark mass second derivatives with respect to the meson fields evaluated at the minimum of the grand potential. Left column block: the sum over two light quark flavors, denoted by index l. Right column block: strange quark flavor, index s.

and correspondingly the antiquark function $b_{\bar{q},f}(T,\mu_f) = b_{q,f}(T,-\mu_f)$. The index i distinguishes between scalar and pseudoscalar fields and is omitted for the sake of brevity in the following. In Tab. A.3, all second quark-mass derivatives w.r.t. the meson fields replaced by the non-vanishing vacuum expectation values in the non-strange-strange basis are collected. Despite the $SU(2)$ isospin symmetry the derivatives are different for the up- and down-quark sector. In the left column block of Tab. A.3 the sum over the two light quark flavors is shown which leads to large cancellations.

A.3. Isoscalar mixing

In this appendix a collection of relations describing the mixing of isoscalar states in the pseudoscalar and scalar multiplet is presented. The isoscalar ($I = 0$) pseudoscalar states in the octet-singlet (η_8, η_0) basis are defined by

$$|\eta_8\rangle = \frac{1}{\sqrt{6}}\left|u\bar{u} + d\bar{d} - 2s\bar{s}\right\rangle, \quad |\eta_0\rangle = \frac{1}{\sqrt{3}}\left|u\bar{u} + d\bar{d} + s\bar{s}\right\rangle. \tag{A.13}$$

For a realistic flavor symmetry breaking in the vacuum the physical η meson is close to the η_8 and η' to η_0.

The eigenstates in the flavor non-strange-strange $(\eta_{\rm NS}, \eta_{\rm S})$ basis are given by

$$|\eta_{\rm NS}\rangle = \frac{1}{\sqrt{2}} \left|u\bar{u} + d\bar{d}\right\rangle , \ |\eta_{\rm S}\rangle = |s\bar{s}\rangle \ . \tag{A.14}$$

These states are associated by a rotation with an angle $\alpha = -\arctan\sqrt{2} \sim -54.74°$

$$\begin{pmatrix} |\eta_{\rm NS}\rangle \\ |\eta_{\rm S}\rangle \end{pmatrix} = \frac{1}{\sqrt{3}} \begin{pmatrix} 1 & \sqrt{2} \\ -\sqrt{2} & 1 \end{pmatrix} \begin{pmatrix} |\eta_8\rangle \\ |\eta_0\rangle \end{pmatrix} \ . \tag{A.15}$$

Diagonalization of the mass matrix in the (η_8, η_0) basis is achieved by the introduction of the pseudoscalar mixing angle θ_P. This yields the relations

$$\begin{pmatrix} |\eta\rangle \\ |\eta'\rangle \end{pmatrix} = \begin{pmatrix} \cos\theta_P & -\sin\theta_P \\ \sin\theta_P & \cos\theta_P \end{pmatrix} \begin{pmatrix} |\eta_8\rangle \\ |\eta_0\rangle \end{pmatrix} \ . \tag{A.16}$$

For the $(\eta_{\rm NS}, \eta_{\rm S})$ basis a similar relation with the mixing angle ϕ_P holds

$$\begin{pmatrix} |\eta\rangle \\ |\eta'\rangle \end{pmatrix} = \begin{pmatrix} \cos\phi_P & -\sin\phi_P \\ \sin\phi_P & \cos\phi_P \end{pmatrix} \begin{pmatrix} |\eta_{\rm NS}\rangle \\ |\eta_{\rm S}\rangle \end{pmatrix} \ . \tag{A.17}$$

For vanishing mixing angle ϕ_P corresponding to $\theta_P = -\arctan\sqrt{2} \sim -54,7°$ the η tends to a pure non-strange $\eta_{\rm NS}$ and η' to a pure strange $\eta_{\rm S}$. In contrast, for a mixing angle $\phi_P = 90°$ ($\theta_P \sim +35.3°$) the ordering is reversed and $\eta \to \eta_{\rm S}$ and $\eta' \to \eta_{\rm NS}$. The ordering transition occurs at $\phi_P = 45°$ ($\theta_P \sim -9.74°$).

The diagonalization of the mass matrix in the $(\eta_{\rm NS}, \eta_{\rm S})$ basis leads to the masses

$$m_\eta^2 = m_{\eta_{\rm NS}}^2 \cos^2\phi_P + m_{\eta_{\rm S}}^2 \sin^2\phi_P - m_{\eta_{\rm S},\eta_{\rm NS}}^2 \sin^2(2\phi_P), \tag{A.18}$$

$$m_{\eta'}^2 = m_{\eta_{\rm NS}}^2 \sin^2\phi_P + m_{\eta_{\rm S}}^2 \cos^2\phi_P + m_{\eta_{\rm S},\eta_{\rm NS}}^2 \sin^2(2\phi_P). \tag{A.19}$$

and to the mixing angle ϕ_P given by

$$\tan 2\phi_P = \frac{2m_{\eta_{\rm S},\eta_{\rm NS}}^2}{m_{\eta_{\rm S}}^2 - m_{\eta_{\rm NS}}^2} \ . \tag{A.20}$$

Equivalently, these expressions can be rewritten in a form which does not contain the mixing angle explicitly

$$m_{\eta'}^2 = \frac{1}{2}(m_{\eta_{\rm NS}}^2 + m_{\eta_{\rm S}}^2 + \Delta_{\eta_{\rm NS},\eta_{\rm S}}) \ , \tag{A.21}$$

$$m_\eta^2 = \frac{1}{2}(m_{\eta_{\rm NS}}^2 + m_{\eta_{\rm S}}^2 - \Delta_{\eta_{\rm NS},\eta_{\rm S}}) \ , \tag{A.22}$$

with $\Delta_{\eta_{\rm NS},\eta_{\rm S}} \equiv \sqrt{\left(m_{\eta_{\rm NS}}^2 - m_{\eta_{\rm S}}^2\right)^2 + 4m_{\eta_{\rm NS},\eta_{\rm S}}^2}$. Note, that these expressions are numerically more stable compared to (A.18 - A.19) because possible ambiguities in the tangent (A.20) do not appear here.

The matrix elements in the $(\eta_{\rm NS}, \eta_{\rm S})$ system are obtained by a change of basis resulting un

$$\begin{aligned} m^2_{\eta_{\rm NS}} &= \frac{1}{3}(2m^2_{p,00} + m^2_{p,88} + 2\sqrt{2}m^2_{p,08}) \ , \\ m^2_{\eta_{\rm S}} &= \frac{1}{3}(m^2_{p,00} + 2m^2_{p,88} - 2\sqrt{2}m^2_{p,08}) \ , \\ m^2_{\eta_{\rm S},\eta_{\rm NS}} &= \frac{1}{3}(\sqrt{2}(m^2_{p,00} - m^2_{p,88}) - m^2_{p,08}) \ . \end{aligned} \tag{A.23}$$

As a consequence, the mixing angles ϕ_P and θ_P are related by

$$\phi_P = \theta_P + \arctan\sqrt{2} \sim \theta_P + 54.74^\circ \ . \tag{A.24}$$

Furthermore, supposing $m_\eta \leq m_{\eta'}$ one finds with (A.18),(A.19) and $\phi_P \leq 45^\circ$ ($\theta_P \leq -9.74^\circ$) $m_{\eta_{\rm NS}} \leq m_{\eta_{\rm S}}$ while for $\phi_P > 45^\circ$ the ordering of the masses in the non-strange-strange system is reversed.

Scalar mesons differ from the pseudoscalar ones only in the orbital excitation. Hence, all quoted relations can be immediately converted to the scalar (σ, f_0) complex with the corresponding replacements, e.g.

$$\begin{pmatrix} |f_0\rangle \\ |\sigma\rangle \end{pmatrix} = \begin{pmatrix} \cos\phi_S & -\sin\phi_S \\ \sin\phi_S & \cos\phi_S \end{pmatrix} \begin{pmatrix} |\sigma_{\rm NS}\rangle \\ |\sigma_{\rm S}\rangle \end{pmatrix} \ . \tag{A.25}$$

For an ideal scalar mixing angle $\phi_S = 90^\circ$ the σ meson is a pure non-strange state $\sigma_{\rm NS}$ and $f_0 \to -\sigma_{\rm S}$. Furthermore, σ replaces η' and f_0 η.

Since the mass of the f_0 meson is larger than m_σ we obtain the ordering $m_{\sigma_{\rm S}} > m_{\sigma_{\rm NS}}$ for an ideal mixing angle $\phi_S = 90^\circ$.

B. Algorithmic Differentiation

In this section we will present the technique used to calculate the derivatives of the grand potential w.r.t. T and μ used in Chap. 5 and 6. More details can be found in [104]. For simplicity we drop the Polyakov loop for this discussion and consider only the case of a uniform chemical potential. The extension to the model with Polyakov loop and different chemical potentials for each flavor is straightforward.

B.1. Introduction

The technique described here is based on *algorithmic differentiation* (AD). Several implementations of AD techniques are available, see [105] for an overview. Algorithmic differentiation is based on the idea that any numerical evaluation of a function is made up of elementary functions. This elementary functions are, e.g., sin, exp and multiplication. All steps performed in the calculation are recorded during runtime. In our calculations these are typically several thousand operations. Using the recorded information it is then possible to use successive applications of the chain rule to evaluate the derivative. In this way at least no additional error is introduced, in principle. Despite the restrictions in machine precision the calculations are as precise as the original function. If the evaluation of the original function is very expensive, requires e.g. numerical minimizations and integrations like in our calculation, it is numerically even cheaper to calculate the derivatives this way.

The grand potential Ω is a function of the temperature T, the chemical potentials and the values of the fields, σ_x, σ_y.

$$\Omega = \Omega(T, \mu; \sigma_x, \sigma_y) \ . \tag{B.1}$$

The integral in Eq. (3.7) has to be solved numerically for $T > 0$. For the explicit dependence of the thermodynamic potential on T and μ it is possible to calculate the derivatives w.r.t. T and μ analytically, however the resulting equations become quite long and contain several integrals that have to be coded and solved numerically. This is not only time-consuming but also error-prone in all required steps, the analytical derivation, the coding and the numerical evaluation of the contained integrals. The analytical calculation can be done in parts using computer algebra system like Mathematica. While this might be acceptable for lower derivatives it is not feasible for higher derivatives.

The considerations above do not take into account that the potential has to be evaluated at the physical point. This introduces an implicit (T, μ) dependence of the fields

$$\bar{\sigma}_x = \bar{\sigma}_x(T, \mu) \ , \quad \bar{\sigma}_y = \bar{\sigma}_y(T, \mu) \ , \tag{B.2}$$

defined by the equations of motion

$$\left.\frac{\partial\Omega(T,\mu)}{\partial\sigma_x}\right|_{\sigma_x=\bar{\sigma}_x,\sigma_y=\bar{\sigma}_y} = \left.\frac{\partial\Omega(T,\mu)}{\partial\sigma_y}\right|_{\sigma_x=\bar{\sigma}_x,\sigma_y=\bar{\sigma}_y} = 0 \ . \tag{B.3}$$

These also include a numerical integral in the derivative of Eq. 3.7 prohibiting analytical inversion.

As already described above, the calculation of the Taylor coefficients, i.e. the derivatives

$$\frac{d^l}{d\mu^l}\Omega\left(T,\mu,\bar{\sigma}_x(T,\mu),\bar{\sigma}_y(T,\mu)\right) \tag{B.4}$$

using AD requires two steps. First, the derivatives up to o-th order

$$\frac{d^l}{d\mu^l}\bar{\sigma}_{x,y}(T,\mu) \tag{B.5}$$

have to be evaluated using an inverse technique. Details can be found in [104].

They will then be used to define a function

$$\bar{\Omega}(T,\mu) = \Omega\left(T,\mu,\bar{\sigma}_x(T,\mu),\bar{\sigma}_y(T,\mu)\right) \tag{B.6}$$

which only depends explicitly on T and μ. The derivatives of $\bar{\Omega}$ can then be calculated using AD and are identical to the derivatives of Ω up to o-th order.

B.2. Errors in numerical derivatives

Before comparing the results obtained using AD with standard numerical derivatives, we introduce the numerical derivatives and discuss their shortcomings.

The simplest approach requires the evaluation of the function a two points

$$f'(x) = \lim_{h\to 0}\frac{f(x+h)-f(x)}{h} \overset{h\neq 0}{=} \frac{f(x+h)-f(x)}{h} \ . \tag{B.7}$$

These finite differences involve two types of errors (cf. e.g.[106]).

The truncation error results from the truncation of the Taylor series of

$$f(x+h) = f(x) + hf'(x) + \dots \ . \tag{B.8}$$

This error depends on the chosen value of h and is generally proportional to h^n, where n depends on the formula chosen to calculate the derivative. Assuming arbitrary precision for the calculation of f, a very small value $h \to 0$ is desirable.

For efficient real world calculations, one is typically limited to double precision arithmetics using 64 bits. This limitation in machine precision enters in the overall round-off

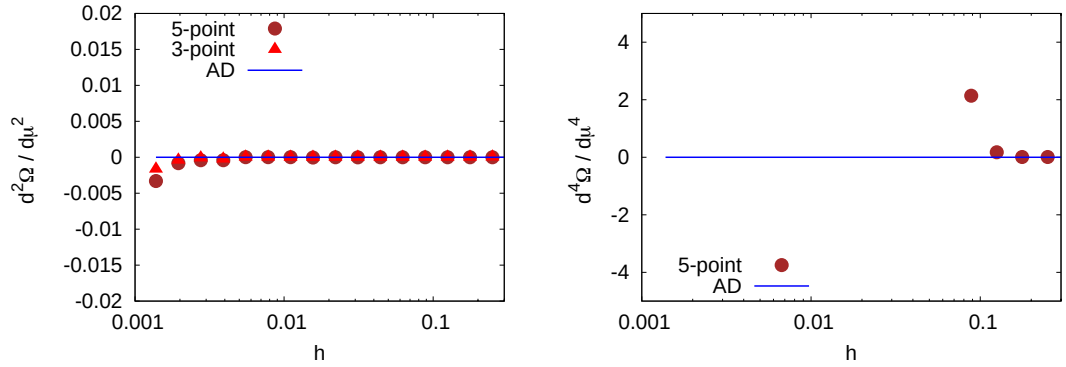

(a) 2nd derivative (b) 4th derivative

Figure B.1.: Numerical derivatives of Ω w.r.t. μ using 3 and 5 points compared with the result using AD at $\mu = 0$ and $T = 183\,\mathrm{MeV}$.

error in different phases of the calculation. Its impact on the final result can be minimized by some clever choices of the value of h. Due to the limited machine precision, the first error will occur already in the calculation oh $x + h$. This error should be on the order of the machine precision. For simple functions the calculation of f will be exact up to machine precision but for more complicated functions like the thermodynamic potential discussed in this work which also involve numerical calculations, this error will be several orders of magnitude larger. Finally the calculation of the difference $f\Delta = (x+h) = f(x-h)$ will also be limited by machine precision. For small values of h, Δ will also become very small. For double precision the smallest difference representable is $\approx 10^{-17}$. To minimize the round-off error a larger value of h is desirable. Thus, the two error types compete and one has to find an optimal value of h. This value will in general be different for each x at which the derivative is calculated.

B.3. Comparison with numerical derivatives

In order to check the numerical implementation and the quality of the calculations using AD, the results of the derivatives are compared with numerical derivatives for the 2nd and 4th derivative. For the 2nd derivative a formula using three function evaluations,

$$f''(x) = \frac{1}{h^2}\left(f(x_1) - 2f(x_2) + f(x_3)\right) + \mathcal{O}(h^2) \tag{B.9}$$

and a formula using five function evaluations,

$$f''(x) = \frac{1}{24h^2}\left(-2f(x_0) + 32f(x_1) - 60f(x_2) + 32f(x_3) - 2f(x_4)\right) + \mathcal{O}(h^4)\ , \tag{B.10}$$

have been used. The evaluation points of the function are defined as

$$x_0 = x - 2h\ , \quad x_1 = x - h\ , \quad x_2 = x\ , \quad x_3 = x + h\ , \quad x_4 = x + 2h\ . \tag{B.11}$$

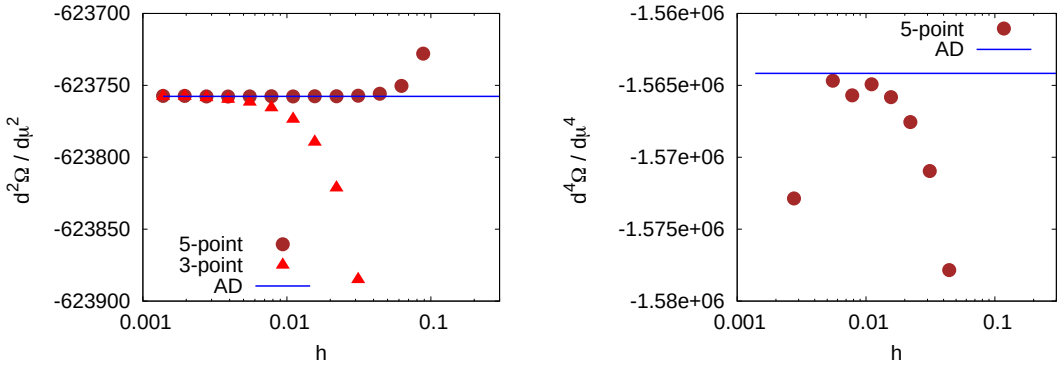

(a) 2nd derivative

(b) 4th derivative

Figure B.2.: Numerical derivatives of Ω w.r.t. μ using 3 and 5 points compared with the result using AD at the $\mu = 327$ and $T = 63\,\mathrm{MeV}$ (CEP).

For the fourth derivative at least five points are needed and therefore only the formula

$$f^{(4)}(x) = \frac{1}{h^4}\left(f(x_0) - 4f(x_1) + 6f(x_2) - 4f(x_3) + f(x_4)\right) + \mathcal{O}(h^4) \tag{B.12}$$

has been used.

In Figs. B.1 and B.2 the results of the numerical derivatives for various values of h are compared to the value obtained using AD. Fig. B.1 shows the derivatives close to the crossover phase transition at vanishing chemical potential $\mu = 0$. One can clearly see the competition of the truncation and the round-off error. For the second derivative, the optimal value is around 0.05 while for the fourth derivative a slightly larger value (≈ 0.1) leads to a better result. In Fig. B.2 the derivatives are calculated near the critical end point. While the round-off error dominated in Fig. B.1, the truncation error is more important here. For the second derivative no round off error is visible at the shown resolution. One can also clearly observe that the truncation error is of $\mathcal{O}(h^4)$ for the five-point formula and $\mathcal{O}(h^2)$ for the three point formula. For the second derivative the result of the five-point formula is indistinguishable from the AD result for $h_5 \approx 0.02$, while for the three-point formula a smaller value of $h_3 \approx 0.04 \approx h_5^2$ is required. For the fourth derivative the region in which the numerical derivative is constant w.r.t. variations of h is very small. Only for $h \approx 0.05$ the numerical result is close to the result obtained using AD. From both figures one can nicely see that the numerical derivatives require a very careful tuning of the value of h. The result obtained with AD always coincides with the result of the numerical differentiation when this is nearly constant w.r.t. h.

C. Conventions

Throughout this work we use natural units

$$\hbar = c = k_B = 1 \tag{C.1}$$

.

C.1. Generators of the $U(3)$

The generators of the $U(3)$, $T_a = \lambda_a/2$ with $a = 0, \ldots, 8$ are related to the usual Gell-Mann matrices

$$\begin{aligned}
\lambda_1 &= \begin{pmatrix} 0 & 1 & 0 \\ 1 & 0 & 0 \\ 0 & 0 & 0 \end{pmatrix}, \quad \lambda_2 = \begin{pmatrix} 0 & -i & 0 \\ i & 0 & 0 \\ 0 & 0 & 0 \end{pmatrix}, \quad \lambda_3 = \begin{pmatrix} 1 & 0 & 0 \\ 0 & -1 & 0 \\ 0 & 0 & 0 \end{pmatrix}, \\
\lambda_4 &= \begin{pmatrix} 0 & 0 & 1 \\ 0 & 0 & 0 \\ 1 & 0 & 0 \end{pmatrix}, \quad \lambda_5 = \begin{pmatrix} 0 & 0 & -i \\ 0 & 0 & 0 \\ i & 0 & 0 \end{pmatrix}, \quad \lambda_6 = \begin{pmatrix} 0 & 0 & 0 \\ 0 & 0 & 1 \\ 0 & 1 & 0 \end{pmatrix}, \\
\lambda_7 &= \begin{pmatrix} 0 & 0 & 0 \\ 0 & 0 & -i \\ 0 & i & 0 \end{pmatrix}, \quad \lambda_8 = \sqrt{\frac{1}{3}} \begin{pmatrix} 1 & 0 & 0 \\ 0 & 1 & 0 \\ 0 & 0 & -2 \end{pmatrix}
\end{aligned} \tag{C.2}$$

and $\lambda_0 = \sqrt{\frac{2}{3}}\, \mathbf{1}$.

The T_a are normalized to $\mathrm{Tr}(T_a T_b) = \delta_{ab}/2$ and obey the $U(3)$ algebra $[T_a, T_b] = i f_{abc} T_c$ and $\{T_a, T_b\} = d_{abc} T_c$ respectively with the corresponding standard symmetric d_{abc} and antisymmetric f_{abc} structure constants of the $SU(3)$ and

$$f_{ab0} = 0 \quad , \quad d_{ab0} = \sqrt{\frac{2}{3}} \delta_{ab} \; . \tag{C.3}$$

See, e.g., [107] for more relations.

Bibliography

[1] C. S. Fischer, J. Phys. **G32**, R253 (2006).

[2] H. Fritzsch, M. Gell-Mann, and H. Leutwyler, Phys. Lett. **B47**, 365 (1973).

[3] H. D. Politzer, Phys. Rev. Lett. **30**, 1346 (1973).

[4] D. J. Gross and F. Wilczek, Phys. Rev. Lett. **30**, 1343 (1973).

[5] K. Rajagopal and F. Wilczek, `arXiv:hep-ph/0011333`.

[6] M. G. Alford, Ann. Rev. Nucl. Part. Sci. **51**, 131 (2001).

[7] B.-J. Schaefer and M. Wagner, Phys. Rev. **D79**, 014018 (2009).

[8] B. Svetitsky, Phys. Rept. **132**, 1 (1986).

[9] H. Meyer-Ortmanns, Rev. Mod. Phys. **68**, 473 (1996).

[10] D. H. Rischke, Prog. Part. Nucl. Phys. **52**, 197 (2004).

[11] P. Braun-Munzinger and J. Wambach, `arXiv:0801.4256 [hep-ph]`.

[12] D. J. Gross, R. D. Pisarski, and L. G. Yaffe, Rev. Mod. Phys. **53**, 43 (1981).

[13] O. Philipsen, Eur. Phys. J. Spec. Top. **152**, 29 (2007).

[14] M. Asakawa and K. Yazaki, Nucl. Phys. **A504**, 668 (1989).

[15] A. Barducci, R. Casalbuoni, S. De Curtis, R. Gatto, and G. Pettini, Phys. Lett. **B231**, 463 (1989).

[16] J. Berges and K. Rajagopal, Nucl. Phys. **B538**, 215 (1999).

[17] Y. Aoki, G. Endrodi, Z. Fodor, S. D. Katz, and K. K. Szabo, Nature **443**, 675 (2006a).

[18] R. D. Pisarski and F. Wilczek, Phys. Rev. **D29**, 338 (1984).

[19] O. Philipsen, PoS **LAT2005**, 016 (2006).

[20] P. de Forcrand and O. Philipsen, JHEP **0811**, 012 (2008).

[21] P. de Forcrand and O. Philipsen, JHEP **0701**, 077 (2007).

[22] K. Fukushima, Phys. Rev. **D78**, 114019 (2008a).

[23] M. A. Stephanov, PoS **LAT2006**, 024 (2006).

[24] M. Peskin and D. Schroeder, *An Introduction to Quantum Field Theory* (Addison-Wesley Publishing Company, 1995).

[25] F. Karsch and E. Laermann, `arXiv:hep-lat/0305025`.

[26] F. Karsch, Lect. Notes Phys. **583**, 209 (2002).

[27] F. Karsch, E. Laermann, and A. Peikert, Nucl. Phys. **B605**, 579 (2001).

[28] M. Cheng et al., Phys. Rev. **D74**, 054507 (2006).

[29] Y. Aoki, Z. Fodor, S. D. Katz, and K. K. Szabo, Phys. Lett. **B643**, 46 (2006b).

[30] C. R. Allton, S. Ejiri, S. J. Hands, O. Kaczmarek, F. Karsch, E. Laermann, and C. Schmidt, Phys. Rev. **D66**, 074507 (2002).

[31] R. V. Gavai and S. Gupta, Phys. Rev. **D68**, 034506 (2003).

[32] R. V. Gavai and S. Gupta, Phys. Rev. **D78**, 114503 (2008).

[33] Z. Fodor and S. D. Katz, JHEP **03**, 014 (2002).

[34] P. de Forcrand and O. Philipsen, Nucl. Phys. **B642**, 290 (2002).

[35] M. D'Elia and M.-P. Lombardo, Phys. Rev. **D67**, 014505 (2003).

[36] K.-F. Liu, Int. J. Mod. Phys. **B16**, 2017 (2002).

[37] S. Kratochvila and P. de Forcrand, PoS **LAT2005**, 167 (2006).

[38] Y. Nambu and G. Jona-Lasinio, Phys. Rev. **124**, 246 (1961a).

[39] Y. Nambu and G. Jona-Lasinio, Phys. Rev. **122**, 345 (1961b).

[40] M. Buballa, Phys. Rept. **407**, 205 (2005).

[41] P. Braun-Munzinger, K. Redlich, and J. Stachel, *Particle production in heavy ion collisions* (2003), `arXiv:nucl-th/0304013`,

[42] M. Gyulassy and L. McLerran, Nucl. Phys. **A750**, 30 (2005).

[43] P. Braun-Munzinger and J. Stachel, Nature **448**, 302 (2007).

[44] P. Senger, T. Galatyuk, D. Kresan, A. Kiseleva, and E. Kryshen, PoS **CPOD2006**, 018 (2006).

[45] G. 't Hooft, Phys. Rept. **142**, 357 (1986).

[46] J. Goldstone, A. Salam, and S. Weinberg, Phys. Rev. **127**, 965 (1962).

[47] D. W. McKay, W. F. Palmer, and R. F. Sarraga, Phys. Rev. **D8**, 2532 (1973).

[48] H. Pagels, Phys. Rept. **16**, 219 (1975).

[49] J. T. Lenaghan, D. H. Rischke, and J. Schaffner-Bielich, Phys. Rev. **D62**, 085008 (2000).

[50] B.-J. Schaefer and J. Wambach, Phys. Rev. **D75**, 085015 (2007).

[51] O. Scavenius, A. Mocsy, I. N. Mishustin, and D. H. Rischke, Phys. Rev. **C64**, 045202 (2001).

[52] J. Kapusta, *Finite-Temperature Field Theory* (Cambridge University Press, 1989).

[53] P. Kovacs and Z. Szep, Phys. Rev. **D75**, 025015 (2007).

[54] W. M. Yao et al. (Particle Data Group), J. Phys. **G33**, 1 (2006).

[55] I. Caprini, G. Colangelo, and H. Leutwyler, Phys. Rev. Lett. **96**, 132001 (2006).

[56] S. Noguera and N. N. Scoccola, Phys. Rev. **D78**, 114002 (2008).

[57] P. Costa, M. C. Ruivo, and C. A. de Sousa, Phys. Rev. **D77**, 096001 (2008).

[58] J. T. Lenaghan, Phys. Rev. **D63**, 037901 (2001).

[59] T. Hatsuda, M. Tachibana, N. Yamamoto, and G. Baym, Phys. Rev. Lett. **97**, 122001 (2006).

[60] K. Fukushima, Phys. Rev. **D77**, 114028 (2008b).

[61] M. Buballa, *private communication.*

[62] T. Kunihiro, Phys. Lett. **B219**, 363 (1989).

[63] S. Strueber and D. H. Rischke, Phys. Rev. **D77**, 085004 (2008).

[64] C. Ratti, M. A. Thaler, and W. Weise, Phys. Rev. **D73**, 014019 (2006).

[65] C. Ratti and W. Weise, Phys. Rev. **D70**, 054013 (2004).

[66] C. Ratti, S. Roessner, M. A. Thaler, and W. Weise, Eur. Phys. J. **C49**, 213 (2007a).

[67] C. Ratti, S. Roessner, and W. Weise, Phys. Lett. **B649**, 57 (2007b).

[68] S. Roessner, C. Ratti, and W. Weise, Phys. Rev. **D75**, 034007 (2007).

[69] C. Sasaki, B. Friman, and K. Redlich, `arXiv:hep-ph/0702025`.

[70] C. Sasaki, B. Friman, and K. Redlich, `arXiv:hep-ph/0702206`.

[71] C. Sasaki, B. Friman, and K. Redlich, Phys. Rev. **D75**, 074013 (2007c).

[72] W.-j. Fu, Z. Zhang, and Y.-x. Liu, Phys. Rev. **D77**, 014006 (2007).

[73] M. Ciminale, R. Gatto, N. D. Ippolito, G. Nardulli, and M. Ruggieri, Phys. Rev. **D77**, 054023 (2007).

[74] H. Abuki, M. Ciminale, R. Gatto, G. Nardulli, and M. Ruggieri, Phys. Rev. **D77**, 074018 (2008).

[75] B.-J. Schaefer, J. M. Pawlowski, and J. Wambach, Phys. Rev. **D76**, 074023 (2007).

[76] J. Greensite, Prog. Part. Nucl. Phys. **51**, 1 (2003).

[77] K. G. Wilson, Phys. Rev. **D10**, 2445 (1974).

[78] R. D. Pisarski, Phys. Rev. **D62**, 111501 (2000).

[79] A. Dumitru and R. D. Pisarski, Phys. Lett. **B525**, 95 (2002).

[80] K. Fukushima, Phys. Lett. **B591**, 277 (2004).

[81] M. Cheng et al., Phys. Rev. **D77**, 014511 (2008a).

[82] L. McLerran and R. D. Pisarski, Nucl. Phys. **A796**, 83 (2007).

[83] F. Karsch, PoS **CPOD07**, 026 (2007).

[84] D. Blaschke, M. Buballa, A. E. Radzhabov, and M. K. Volkov, Yadernaya Fizika, vol. 71, no. **11**, 2012 (2008).

[85] J. P. Blaizot, Acta Phys. Polon. **B18**, 659 (1987).

[86] C. M. Hung and E. V. Shuryak, Phys. Rev. Lett. **75**, 4003 (1995).

[87] B. Stokic, B. Friman, and K. Redlich, `arXiv:0809.3129 [hep-ph]`.

[88] T. Hatsuda and T. Kunihiro, Phys. Rept. **247**, 221 (1994).

[89] M. E. Fisher, Rep. Prog. Phys. **30**, 615 (1967).

[90] R. B. Griffiths and J. Wheeler, Phys. Rev. **A**, 1047 (1970).

[91] Y. Hatta and T. Ikeda, Phys. Rev. **D67**, 014028 (2003).

[92] R. V. Gavai and S. Gupta, Phys. Rev. **D71**, 114014 (2005).

[93] C. Miao, C. Schmidt, and f. R.-B. Collaboration (RBC-Bielefeld), `arXiv:0810.0375 [hep-lat]`.

[94] P. de Forcrand and O. Philipsen, Nucl. Phys. **B673**, 170 (2003).

[95] F. Karsch, *private communication*.

[96] C. R. Allton, M. Doering, S. Ejiri, S. J. Hands, O. Kaczmarek, F. Karsch, E. Laermann, and K. Redlich, Phys. Rev. **D71**, 054508 (2005).

[97] C. R. Allton, S. Ejiri, S. J. Hands, O. Kaczmarek, F. Karsch, E. Laermann, and C. Schmidt, Phys. Rev. **D68**, 014507 (2003).

[98] I. N. Bronstein, K. A. Semendjajew, and G. Musiol, *Taschenbuch der Mathematik* (Verlag Harri Deutsch, Frankfurt am Main, Thun, 1999), 4th ed., ISBN 3-8171-2014-1.

[99] C. Schmidt, *Talk given at the conference 'Lattice 2008'* (2008).

[100] F. Karsch, K. Redlich, and A. Tawfik, Eur. Phys. Jour. **C29**, 549 (2003a).

[101] F. Karsch, K. Redlich, and A. Tawfik, Phys. Lett. **B571**, 67 (2003b).

[102] M. Cheng et al., `arXiv:0811.1006 [hep-lat]`.

[103] B.-J. Schaefer and J. Wambach, Nucl. Phys. **A757**, 479 (2005).

[104] M. Wagner, B.-J. Schaefer, and A. Walther, *work in progress*.

[105] *www.Autodiff.org*.

[106] W. H. Press, S. A. Teukolsky, W. T. Vetterling, and B. P. Flannery, *Numerical Recipes in C (2nd ed.): The art of scientific computing* (Cambridge University Press, New York, NY, USA, 1992), ISBN 0-521-43108-5.

[107] V. I. Borodulin, R. N. Rogalev, and S. R. Slabospitsky, `arXiv:hep-ph/9507456`.

Danksagung

Am Gelingen dieser Arbeit haben viele Personen einen bedeutenden Anteil. Für die Unterstützung möchte ich mich an dieser Stelle ganz herzlich bedanken.

An erster Stelle danke ich meinem Doktorvater Prof. J. Wambach für die Gelegenheit diese Arbeit zu verfassen und seine konstante Unterstützung. Sehr dankbar bin ich auch für die Möglichkeit, mehrere Workshops und Konferenzen besuchen zu können um dort meine Arbeiten zu präsentieren und diskutieren.

Wesentlich zum Gelingen dieser Arbeit hat Dr. Bernd-Jochen Schaefer beigetragen. Die Zusammenarbeit in den letzten Jahren war geprägt von einer freundschaftlichen Atmosphäre.

Prof. Christian S. Fischer danke ich für die Übernahme des Zweitgutachtens.

Dem Dokoratskolleg ‚Hadrons in vacuum, nuclei and stars' des Instituts für Physik an der Universität Graz und Prof. R. Alkofer möchte ich für die Ermöglichung mehrerer Forschungsaufenhalte in Graz danken. Die angenehme Atmosphäre dort hat stets zu sehr angenehmen und produktiven Wochen geführt.

Prof. M. Oka und den Organisatoren des ‚Foreign Graduate Invitation Program' am Tokyo Institute of Technology möchte ich für das Stipendium im Rahmen des o.g. Programms danken, dass mir einen Aufenthalt in Tokio und damit verbunden auch die Teilnahme an der ‚INPC 2007' erlaubt hat.

Prof. A. Walther danke ich für die Unterstützung bei der Anwendung und Entwicklung des Codes zum algorithmischen Differenzieren. Für hilf- und aufschlussreiche Diskussion zur Taylorentwicklung danke ich Prof. F. Karsch, Prof. E. Laermann und Prof. K. Redlich.

Den Mitgliedern der Theoriegruppen am Institut für Kernphysik möchte ich für die angenehme Arbeitsatmosphäre und zahl- und hilfreiche Diskussionen danken.

Einen grossen Anteil an der angenehmen Atmosphäre hatte die Kaffeerunde im Zimmer 411: Heiko Hergert, Markus Hild, Verena Kleinhaus und Felix Schmitt. Diese hatte sich auch beim Korrekturlesen dieser Arbeit verdient gemacht. Besonders unermüdlich war hierbei Heiko Hergert.

Verena Kleinhaus bin ich besonders dankbar für die moralische Unterstützung und die Möglichkeit Freud und Leid, die während des neunjährigen Weges bis zu dieser Arbeit aufgetreten sind, zu teilen.

Meine Familie hat mir das Physikstudium überhaupt erst ermöglicht und mich während des gesamten Studiums stets unterstützt.

Abschließend möchte ich noch meiner Frau Britta für ihre grenzenlose Unterstützung und besonders ihr Verständnis für die heiße Endphase und den ‚freien Rücken' in selbiger danken.

Lebenslauf

Name:	Mathias Wagner
Geburtsdatum:	06. März 1979
Geburtsort:	Frankfurt am Main
Staatsangehörigkeit:	deutsch
Eltern:	Richard Wagner Anne Wagner, geb. Ludwiczak
Familienstand:	verheiratet

Bildungsweg

07/1985-07/1989	Besuch der Lindenschule Kriftel (Grundschule)
08/1989-06/1998	Besuch der Main-Taunus-Schule in Hofheim a.Ts. (Gymnasium)
06/1998	Abitur, Gesamtnote: 1.1
09/1998-10/1999	Zivildienst in der Robinsonschule, Hattersheim a.M.
10/1998-10/1999	Fernstudium Informatik an der FU Hagen (Teilzeit).
10/1999-11/2004	Studium der Physik und Informatik an der TU Darmstadt
10/2001	Vordiplom Physik, Gesamtnote: gut
10/2002	Vordiplom Informatik, Gesamtnote: gut
09/2003-09/2004	Anfertigung der Diplomarbeit *"Anwendung der $V_{low\,k}$ Renormierungsgruppenmethode auf Hyperon-Nukleon Systeme"*
11/2004	Diplom, Gesamtnote: sehr gut
seit 12/2004	Promotionsstudium an der TU Darmstadt und Anfertigung der Dissertation
seit 12/2004	Wissenschaftlicher Mitarbeiter am Institut für Kernphysik Administration von Servern und Arbeitsplatzrechnern Aufbau eines Rechenclusters mit 200 Prozessoren